Republic of Iraq
Ministry of Higher Education and Scientific Research
University of Kerbala-College of Science
Chemistry Department

Preparation, Characterization of Spinel Cobalt Chromite/Zirconium Oxide Nanocomposite and Application on the Colored Solution

A Thesis

Submitted to the Council of the College of Science/ University of Kerbala

In a Partial Fulfillment of the Requirements for the Degree of Master of Science

in Chemistry

By

Hamad Hameed Kazem

B.Sc. Chemistry (2008) / Babylon University

Supervised by

Prof. Dr. Luma Majeed Ahmed   **Prof. Dr. Mohanad Mousa Kareem**

2021 AD   **1443 AH**

بسم الله الرحمن الرحيم

﴿ قُل لَّوْ كَانَ الْبَحْرُ مِدَادًا لِّكَلِمَاتِ رَبِّي لَنَفِدَ الْبَحْرُ قَبْلَ أَن تَنفَدَ كَلِمَاتُ رَبِّي وَلَوْ جِئْنَا بِمِثْلِهِ مَدَدًا ﴾

صدق الله العلي العظيم

سورة الكهف
الآية (١٠٩)

Supervisor Certification

We certify that this thesis, entitled " **Preparation, Characterization of Spinel Cobalt Chromite/Zirconium Oxide Nanocomposite and Application on the Colored Solution** " has been prepared under my supervision, by " **Hamad Hameed Kazem** " at the department of Chemistry, College of Science, University of Kerbala in a partial fulfillment of the requirements for the degree of Master of Science in Chemistry

Signature:

Signature:

Name: **Dr. Mohanad Mousa Kareem**
Title: Professor
Address: University of Babylon, College
of Science, Department of chemistry.

Name: **Dr. Luma M. Ahmed**
Title: Professor
Address: University of Kerbala, College
of Science, Department of Chemistry

Date: / /2021

Date: / /2021

In view of the available recommendations, I forward this thesis for debate by the examining committee.

Signature:

Name: **Dr. Adnan Ibrahim Al-Saadi**

Title: Assist Professor

Head of the Chemistry Department, college of science/ University of Kerbala
Date: / / 2021

Dedication

*To my father's and mother   soul (may God
have mercy on them)*

To all members of my family

To all friends and lovers

To every science students

I dedicate this study

Hamad

Acknowledgments

Praise be to **Allah**, Lord of the worlds, May God's blessings are upon **Mohammed** and his pure immediate family, and thanks to God for his countless and numberless graces and gifts.

I would like to extend my deep thanks, gratitude, and appreciation to:

My supervisor *Prof. Dr. Luma Majeed Ahmed and Prof.Dr. Mohanad Mousa Kareem* for her continuous support and invaluable suggestions and great contributions since the very beginning of this

work.

Also, I thank all faculty members of the Department of Chemistry in the College of Science at the University of Kerbala, for their worthless support of the work.

Finally, I thank my family and friends for their continued support throughout this journey. They were my source of encouragement along the way.

Abstract

This practical work involves three main parts. The first part illustrates the Luminol reagent, Luminol- tyrosine as ligand, and Fe(II)-(Luminol-Tyrosine) complex were prepared. Uv-Visible spectra, Fourier-Transform Infrared Spectroscopy (FTIR), Proton Nuclear Magnetic Resonance Spectroscopy (^{1}HNMR), Elemental Micro Analysis (C.H.N), and melting point (m.p) were confirmed prepared the top mention compounds. The hybridization of FeL_2Cl_2 complex is octahedral, which was investigated by using magnetic sensitivity and mole ratio method and obtained the ratio between Fe(II) and L is equal to 1:2.

The **second part** focused on the preparation of spinel $CoCr_2O_4$ using the co-precipitation method. The surface of spinel $COCr_2O_4$ was modified by chosen the ZrO_2 to improve its properties. The synthesis composites from incorporated spinel $CoCr_2O_4$ with ZrO_2 in different ratios (1:2 and 1:3) were performed using the ultrasonic technique as a simple and friendly-environment method. Based on X-ray diffraction (XRD), the spinel $CoCr_2O_4$, commercial ZrO_2, and spinel $CoCr_2O_4$ /ZrO_2 composites in different ratios (1:2 and 1:3) are nano-sizes with ranged 8.1785 nm to 15.5823 nm. The sequence of mean crystal sizes values is

ZrO_2 < composite 1:3 < composite 1:2 < spinel $CoCr_2O_4$.

The scan electron microscopy (SEM) given an idea of the morphology of the surface of the studied photocatalyst. The spinel $CoCr_2O_4$ shape and the rest photocatalysts are found to be quasi-spherical, except ZrO_2 has a spherical shape. Based on the SEM analysis, the range of the particle sizes for all studied photocatalysts is found to be from 17.89 nm to 52.62 nm, which conformed to all the studied samples regard as nano-crystals. Through the energy dispersive X-rays (EDX) spectra, that demonstrated the photocatalysts are prepared without any impurity. spectra detect the presence of Co, Cr,Zr and O in the

synthesized cobalte cromite and its nanocomposite materials. Tauc equation was used to found the band gaps for studied photocatalysts and found the bandgaps are indirect for all samples. The value of the bandgap for spinel $CoCr_2O_4$ increases with increasing the ratio of ZrO_2 via the preparation of its composites. The sequence of band gaps values is

Bg spinel $CoCr_2O_4$ < Bg Comp.1:2 < Bg Comp.1:3 < Bg ZrO_2,

and equal to 3.18 eV < 4.7 eV < 4.8eV< 5 eV, respectively.

In the **third part**, the application of studied photocatalysts was performed. The photo-decolorization of FeL_2Cl_2 complex at pH 7.3 was estimated using spinel $CoCr_2O_4$, commercial ZrO_2, and composites 1:2 and 1:3. The composite 1:3 is the best composite compared with composite 1:2. The optimum doses which used in photo-decolorization of FeL_2Cl_2 complex are 0.1g/ 100 mL, 0.2 g/100 mL and 0.3g/ 100 mL for using spinel $CoCr_2O_4$, ZrO_2, composite 1:2 and composite1:3 respectively. The decreased temperature enhanced the decolorization of the complex using spinel $CoCr_2O_4$ and composite 1:3 but inhibited the use of ZrO_2. The activation energy for using composite 1:3 is less than that using spinel $CoCr_2O_4$, and equal to -93.1084 kJ/mol and -46.2499 kJ /mol, respectively.This behaver depends on structure of spinel that involving from two metals in different oxidation state and hydridization (i.e Co (II) as tetrahaydral and Cr(III) as octahydral).

Table of Contents

List of abbreviations and Symbols

Abbreviation and Symbols	The Meaning
^{1}HNMR	Proton nuclear Magnetic Resonance
A_o	Initial absorbance
At	absorbance of substrate at time t of irradiation
Bg	Band gap
CB	Conduction Band
e-	Negative Electron
Ea	Activation Energy
EDX	Energy dispersive X-rays
E_f	Fermi Level
Eg	Energy gap
eV	Electron Volt
FWHM	Full width half –maximum
h^+	Positive Hole
HOMO	Highest Occupied Molecular Orbital
I_o	Light intensity
JCPDS	Joint Contry of Powder Diffraction Standard
k	Wave factor
k_{app}.	Apparent Rate constant
L	Crystallite Size
LUMO	Lowest Occupied Molecular Orbital
M.B	Melting Boint
PDE	Photo decolourization efficiency
SEM	Scan electron microscopy
T	Temperature
TMS	Tatramethyl silicon
UV-Vis	Ultra violet light in the range from 315 to 380nm
VB	Valance Band
XRD	X-Ray diffraction
λ	Wavelength
μ_{eff}	Magnetic Moment

CHAPTER ONE

Introduction

Chapter One   Introduction

1.1 General Introduction

Nanotechnology is an intriguing area that deals with particles smaller than 100 nm in size. Due to their tiny size, these particles have a high surface-to-volume ratio . In other words, these particles have a large number of active sites, which significantly increases their activity. Numerous kinds of nanomaterials have been described in the literature for different applications[1], including nanotubes, quantum dots, nanowires, nanocolloids, nanoparticles, and nanofilms. Whereas, the bulk materials are particles with a diameter of greater than 100 nm in all directions. The physical characteristics of bulk materials are size insensitive. Nanoparticles (NPs) have the potential to be used in a variety of applications, including water treatment facilities, oil refineries, petrochemical industries, industrial processes, catalytic processes, structures and building materials, diagnostics, and medication delivery[2].Nanocarbons may be used to detect hazardous gases in the environment [3]. Gas sensors based on nanocarbons have many benefits over traditional gas sensors [4,5]. These gas sensors are very sensitive, use little power, and operate at a low temperature (Figure1-1) illustrates a gas sensor made of nanomaterials. The sensor's resistance or conductance has changed in response to direct gas contact.
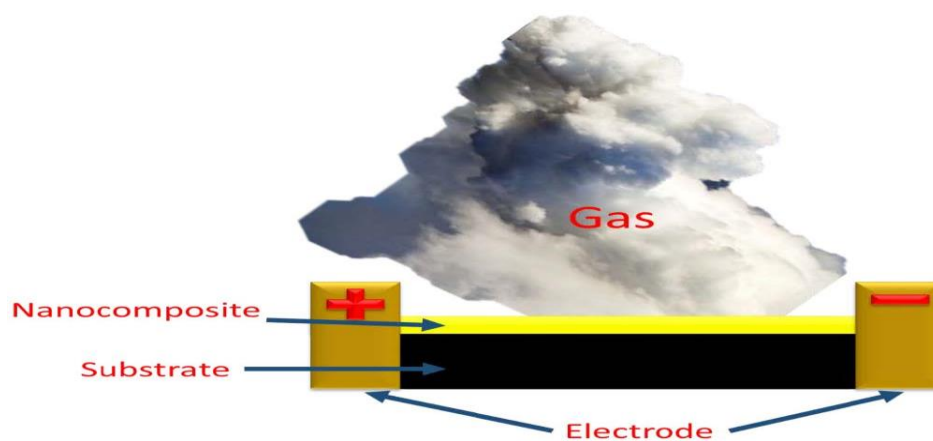
Figure (1-1). Gas sensor[5].

Carbon nanoparticles have been utilized in the treatment of wastewater [6,7]. (Figure1-2) illustrates the sorption behavior of pollutants in water. These nanoparticles have a large surface area, a high number of active sites, a uniform pore size distribution, and an extraordinary capacity for sorption.
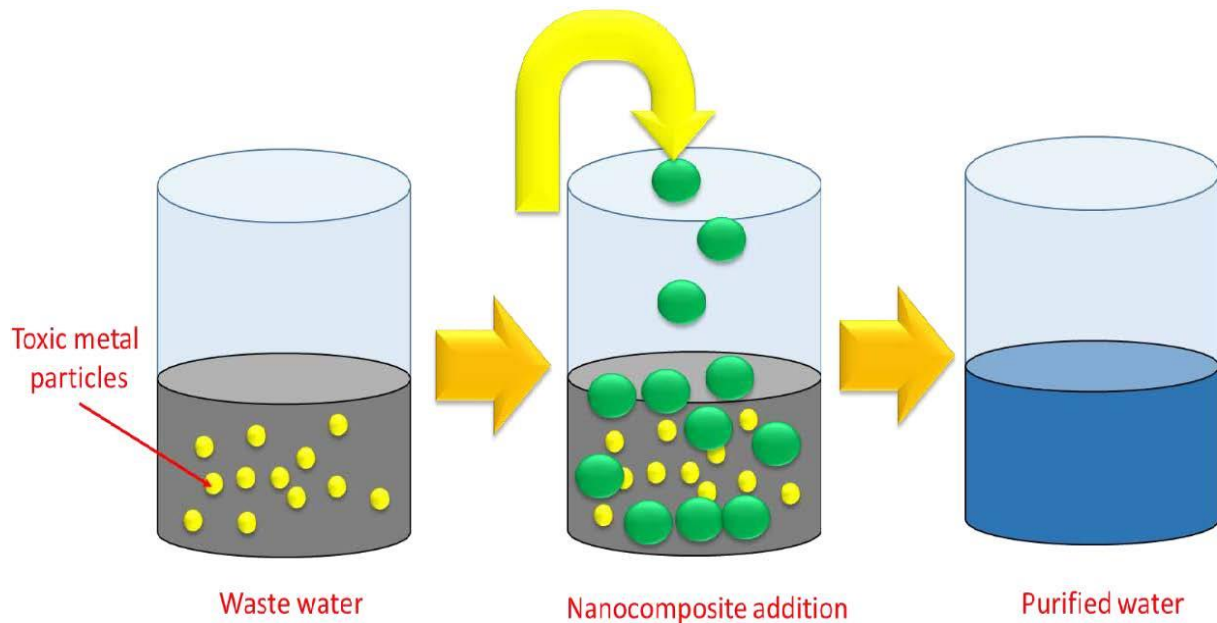
Figure(1- 2). Sorption behavior of nanosorbents[8].

1.2 Classification of nanomaterials

Nanomaterials may be categorized based on several factors. The size, shape, condition, and chemical content NMs are frequently classified according to their [9]. Furthermore, their size, which varies between 1 and 100 nm in at least one dimension, determines their categorization as shown in Figure(1-3) [10].
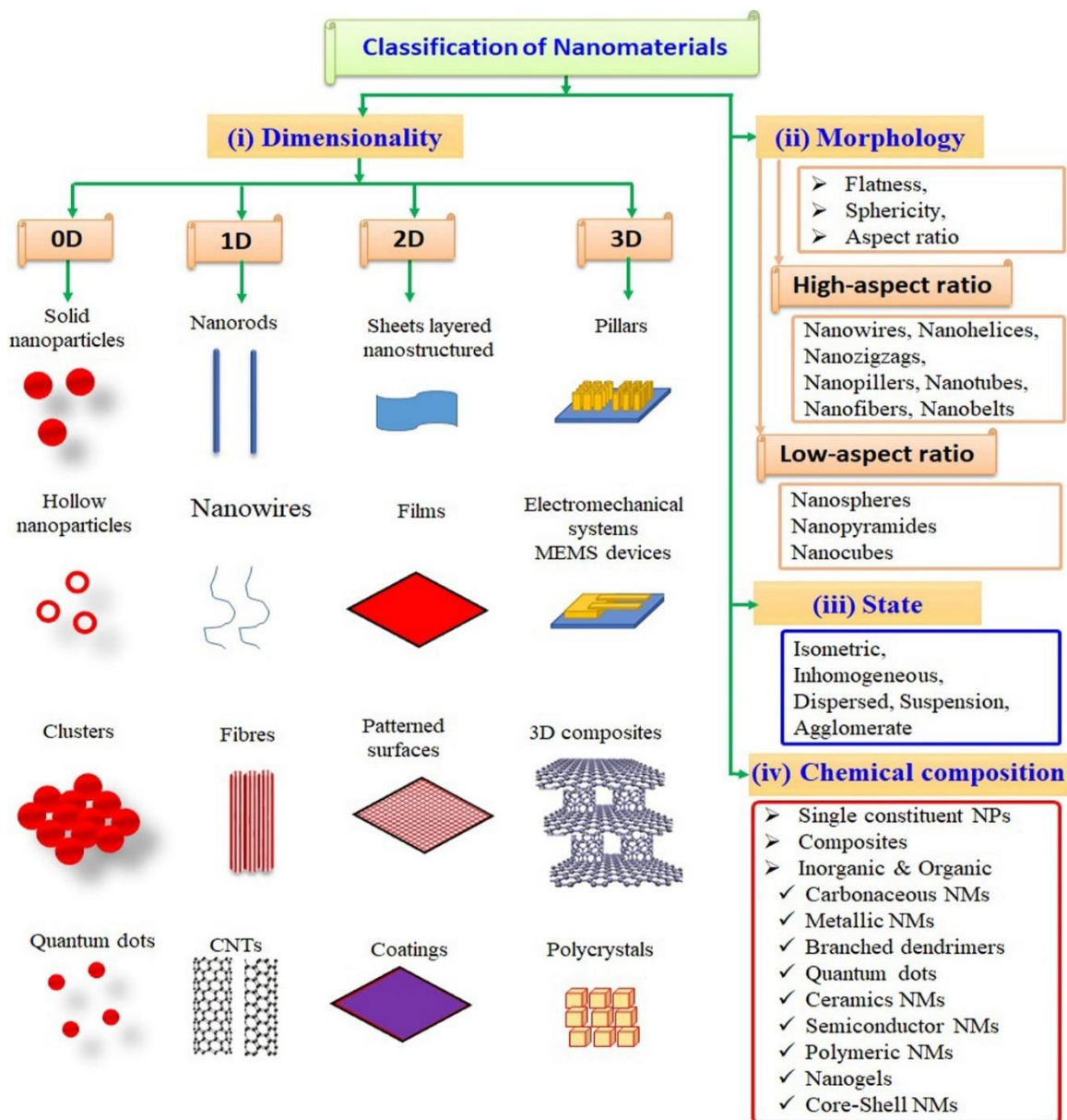
Figure (1-3). Diagrammatic representation of the categorization of nanomaterials according to several criteria.

1.3 Composite nanomaterials

Composites are solid materials made up of many phases, at least one of which is smaller than 100 nm in size, or structures with a nanoscale repetition spacing between phases [11,12]. Nanometer-scale physical dimensions are constantly utilized in the fabrication of composite structures. A composite material

composed of multiple materials may exhibit a variety of characteristics, including flexural strength, water absorption, optical properties, wear, and gloss retention [13]. For reactive orange dye adsorption, the Box–Behnken design can be employed to make chitosan–tripolyphosphate/TiO_2 nanocomposites that require less energy and chemicals [14] When components were combined to form nanocomposites, the surface area of the materials rose from 0.156 m^2/g to 2.75 m^2/g. Through a variety of interactions, such as electrostatic interactions, n- interactions between lone pair of electrons delocalized into the -orbital, dipole-dipole hydrogen bonding, and Yoshida H-bonding, composite materials enable the material's adsorption capacity to be increased [15].

1.4 Semiconductor nanomaterials

The word semiconductor refers to a class of materials that exhibit electrical characteristics that vary from those of insulators and conductors, with their electrical conductivity values falling between these two categories. Insulators are sometimes thought of as extremely large bandgap semiconductors (see Figure 1-4).
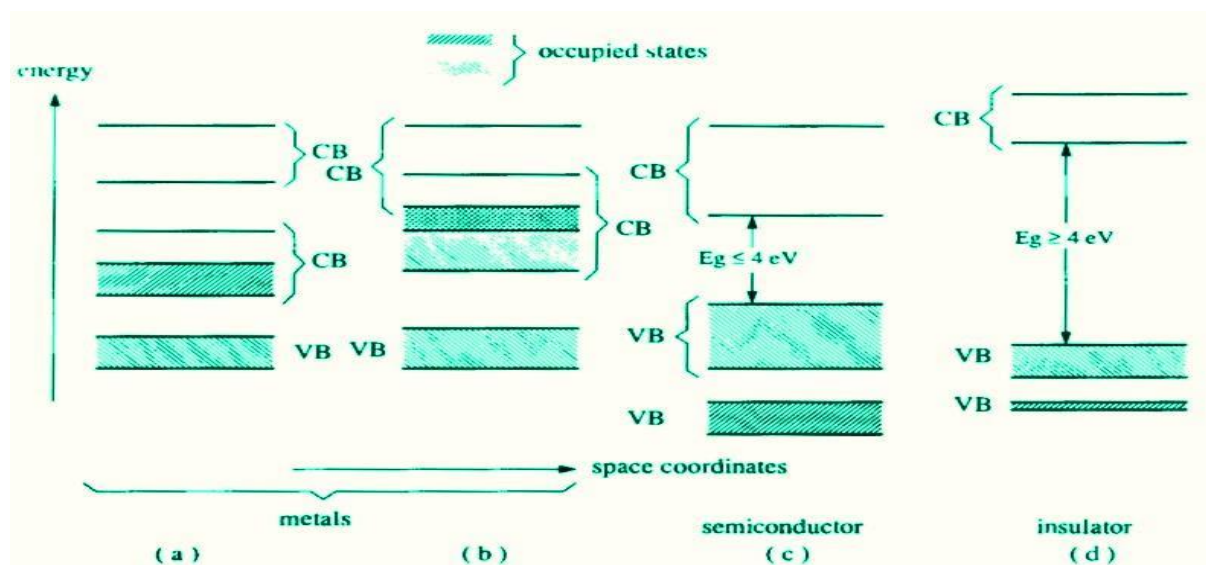
 Figure (1-4). Occupation states for the following materials: (a) (b) Metals, (c) Semiconductor, and (d) Insulators (CB: Conduction Band and VB: Valence Band) [16].

The bandgap energy of semiconductors is on the order of kT. Although most semiconductors are crystalline solids, some amorphous materials and liquids show comparable characteristics. They may be made up of a single pure element (from the periodic table's column IV) or a compound (from columns III and V, II and VI, IV and VI, or different group IV elements). A critical difference between direct and indirect bandgap conductors is required for optoelectronic applications. As explained in (Figure1-5), direct bandgap semiconductors (such as InP and GaAs) have a valence band maximum that corresponds to the conduction band minimum when the wave vector k is null. As a result, an electrical transition from the lowest energy level of the conduction band to the highest energy level of the valence band is feasible without changing the wave vector value. On the other hand, some semiconductors have a conduction band minimum that is not zero in momentum. This indicates that, in addition to energy loss, electron relaxation results in a change in momentum (i.e. the emission of a phonon). Radiative recombination is thus considerably less likely to occur than in a straight bandgap semiconductor since the radiative recombination period will be longer and therefore the majority of recombination will be non-radiative (via phonon emission at defect locations)[17]. As a result, direct-gap semiconductors are much more efficient at generating light. The bandgap energies are influenced by pH and electrons move between the smallest conductive band called the lower occupied molecular orbital (LUMO) and the largest valence band in most semiconductors, this is referred to as the high molecular orbital occupied (HUMO) [18].
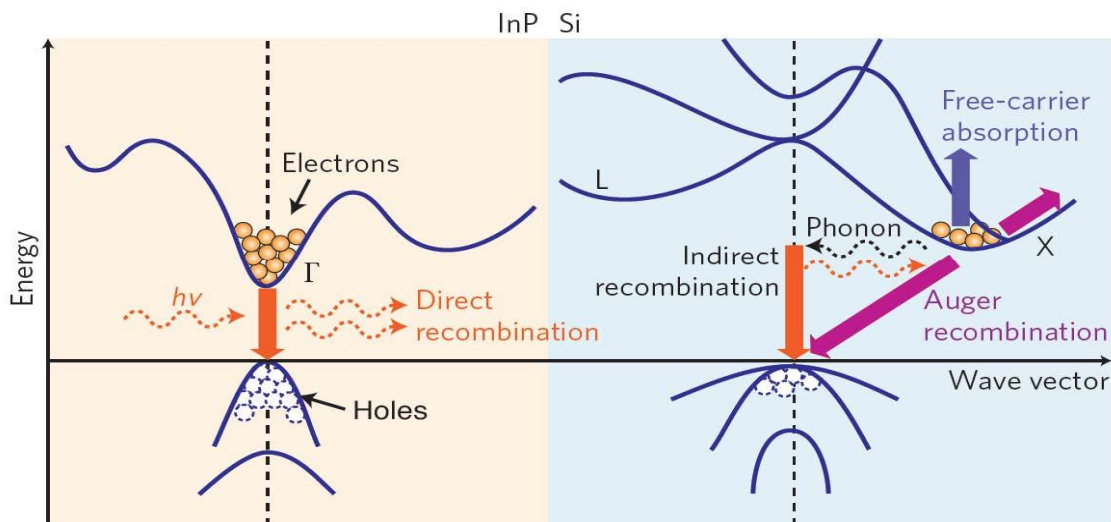
Figure (1-5). Energy band diagrams showing main carrier transition processes in crystals of indium phosphide (direct bandgap) and silicon (indirect bandgap) [17].

When examining the photon/semiconductor interaction in optoelectronic devices, three different processes must be considered, as shown in Figure (1-6). The first is spontaneous emission, in which an electron loses energy while transitioning from the conduction to the valence bands and emits it as a photon. The second is absorption: absorption occurs when a photon of certain energy stimulates an electron to a higher energy level. Finally, stimulated emission occurs when an electron-hole pair is recombined by a photon with an energy equal to the difference between the two energy levels. The second photon of equal energy is emitted. Other types of semiconductor/light interaction, such as non-radiative recombination, Auger recombination, and Shockley-Read-Hall recombination, may need to be considered during the device's design[19].
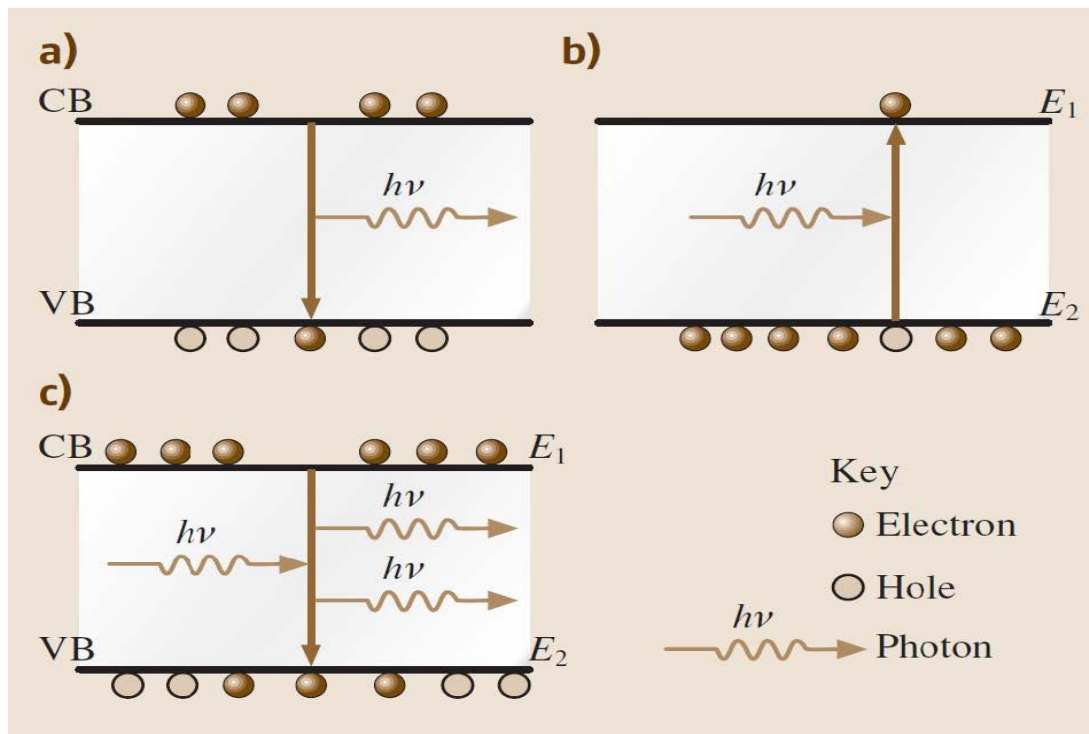
Figure (1-6). The types of electron-photon interactions in semiconductors: (a) spontaneous emission,(b) stimulated absorption, and (c) stimulated emission[19].

The semiconductor NMs are classified into two categories:

1. Inherent semiconductors, which are comprised of pure compounds or elements that are not doped and are present in the structure due to the presence of other metals. The temperature coefficients of resistance of intrinsic semiconductors are negative, which is their primary feature. This implies that as the temperature rises, the material's resistance lowers and its conductivity rises.

2. Extrinsic semiconductors, which are a kind of material added to other metals through doping to improve their conductivity, such as type-n and type-p semiconductors. Figure(1-7). is a description of some properties of nanomaterials and a brief explanation of each property[19]

Properties

Electronic properties

Optical properties

Magnetic properties

Mechanical properties

Thermal properties

NPs have mechanical characteristics that are distinct from those of microparticles or bulk materials. NMs have a high surface area and are easily modified, which results in a rise in mechanical characteristics like hardness, adhesion, stress and strain, and elastic modulus. Mechanical characteristics are shown by NPs derived from a class of inorganic chemicals, while organic molecules typically exhibit poor mechanical properties. Thus, it is common to enhance the mechanical characteristics of organic molecules via the addition of inorganic substances.

NPs' optical characteristics, particularly those of semiconductor materials, are critical for a variety of applications, including photocatalysts and photovoltaics. Basic light concepts and the Beer–Lambert equation may be used to establish the optical characteristics. The enhanced absorption of wavelengths in semiconductor NPs is determined by a number of variables, including the size distribution, shape, and size of the NPs, as well as the kind of modifiers used.

Because NPs have a high surface area, heat exchanges occur directly on the material's surface. The thermal characteristics of NPs are mostly determined by their high surface area, mass concentration, the ratio of energic atoms in NPs, and the percentage of NP volume distributed

The electronic characteristics of nanoparticles vary according to their size, surface area, chemical composition, and modification . Additionally, this kind of alteration results in altered electrical properties. Thus, the addition of inorganic chemicals to polymer systems improved the electrical characteristics of the polymer nanocomposites .

The magnetic characteristics of NPs are affected by their particle size . Generally, the change in particle size is very minor and has little effect on the metals' lattice characteristics. However, for metals with metal oxides on the surface, the lattice parameters of the metals may vary when the particle size changes owing to mismatches between the metal's lattice parameters and those of the metal oxides, resulting in additional interfacial tension on the surface. As a result, the magnetization value will vary as the particle size changes.

Figure (1-7). General Properties of the Nanomaterials[20-24].

1.5 Nanomaterials Quantum Dots (NQDs)

Due to their nanoscale size and flexibility to be tailored for specific applications such as nonlinear optical devices (NLO), electro-optical devices, and computers, quantum dots (QDs). It is known as semiconducting nanoparticles, are prospective zero-dimensional advanced materials [25].QDs are nanoscale semiconductor particles with optical and electrical characteristics that differ from those of bigger particles owing to quantum mechanics. Since QDs absorb white or ultraviolet light and reemit it at a specific wavelength, they exhibit unique optical and electrical characteristics. Here, electrons in the conduction band, holes in the valence band, and exactions are constrained to three spatial dimensions. Quantum mechanical factors dictate the electronic characteristics of semiconductors in the 1–10 nm range. Thus, quantum dots are nanospheres with a diameter of 1–10 nm, and their optical characteristics are very shape-and size-dependent. The photogenerated electron-hole pair's exciton diameter is on the order of 1–10 nm. It is possible to regulate the absorption and emission of light using semiconductors by altering the nanoparticle size in this range [26].

1.5.1. Core − Shell Structure Quantum Dots.

A popular way for designing the QD surface is to use a core-shell structure [27]. The inorganic core of nano-heterostructures is covered by a separate of different semiconductor material as an epitaxial shell, which improves the coupling strength between QDs. Type I, type II, and type III as in the figure(1-8). arrangements may be constructed based on the semiconductors' band positions. In a type I structure, the conduction and valence bands of the core semiconductor are proportionately greater and smaller than those of the shell semiconductor, resulting in electrons and holes being constrained in the core. In type II and III structures, the band edges of the core semiconductor are

staggered from the band edges of the shell semiconductor, resulting in lower recombination rates due to spatially separated electrons and holes [28]. As a result, heterojunction topologies affect device performance in a variety of ways. Typically, type I QDs with shielded electronic states of the core material are advantageous for obtaining the high photoluminescence quantum yield required for high-efficiency electro-luminescence, whereas, type II core/shell QDs are advantageous for charge separation and transport between QDs. As a result, type I quantum dots with charge confinement capabilities are favored for memory applications. The reported core shell quantum dot memory systems are mostly focused on type I quantum dots, such as ZnSe/ZnS, CdSe/ZnS, InP/ZnSe, CdS/PbS, and $CuInS_2$/ZnS [29], type II quantum dots, such as CdS/HgS, CdS/CdSe, ZnSe/CdSe [30] , and MgO/ZnO[31], and type III quantum dots, such as ZnTe/CdSe, CdTe/CdSe, CdS/ZnSe[32].
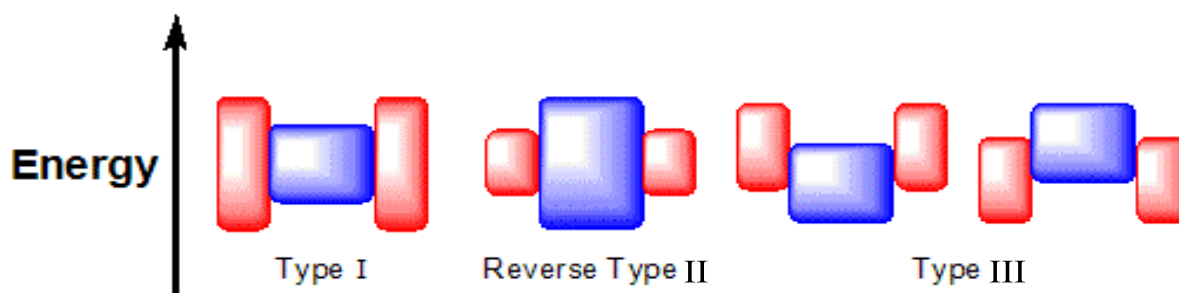
Figure (1-8). The three types of core–shell nanocrystals. The upper and lower edges represent the upper and lower energy edges of the core (blue) and the shell (red)[28].

Carbon quantum dots are a novel kind of carbon nanoparticle. They are one-dimensional discrete and quasi-spherical nanoscale carbon particles with a diameter of less than 10 nm [31]. Carbon quantum dots have several unique properties that make them exceptional materials for a variety of applications, including the following[34-36]. (i) tunable photoluminescence characteristics and excellent multi-photon excitation; (ii) biocompatibility and minimal

toxicity; (iii) certain unique quantum confinement phenomena; (iv) water solubility owing to the abundance of oxygen-containing groups; and (v) cost efficiency and environmental friendliness. They have an abundance of functional groups containing oxygen on their surface, such as carboxylic acids. Carbon quantum dots incorporated may significantly improve charge transfer and separation efficiency, inhibit photoexcited carrier recombination, and narrow the bandgap. Carbon quantum dots have several benefits over traditional semiconductor-based quantum dots, and as a result, have garnered significant scientific interest [37]. They have gained prominence in recent years because of to fire exceptional properties in the areas of light-emitting diodes, nanomedicine, solar cells, sensors, catalysis, and bioimaging.

1.5.2 Optical Properties of Quantum Dots.

In bulk semiconductors, free carriers form when the energy of a photon exceeds the semiconductor bandgap. The recombination rates of holes and electrons are quite high in bulk semiconductors with high permittivity and low Coulomb binding energy. Whereas, the quantum and dielectric confinement influenced in QDs produce a high light absorption resonance and allow for the electrons to pass between discrete states. The excitons are formed when electron-hole pairs with high binding energy are created as a result of QDs absorption of light at specific photon energy. Based on quantum dots direct bandgap, the electron-hole recombination is frequently accomplished through a band-to-band radiative transfer with almost monochromatic hues owing because of the quantized electronic states. The High-density interstitial trap states are produced on the surface of QDs through dangling bonds, resulting in competitive edge recombination (figure 1-9). Irradiation trap recombination may be aided by ligand passivation, which reduces the density of unintended traps. The charged QDs may give birth to excitons by a more effective Auger mechanism with subsequent stimulation. After the absorption of multiple photons with high

excitation densities, numerous excitons would be produced in a single QD. A single electron-hole pair may be driven to a high energy state (hot excitation) and subsequently relaxed to the band-edge state without emitting radiation throughout numerous exciton production cycles (cooling process). The cooling process stores enough energy to ignite another electron-hole pair across the bandgap. The ability of QDs to double the number of carriers is a key feature since it allows photoelectric memory applications to use QD films[38].
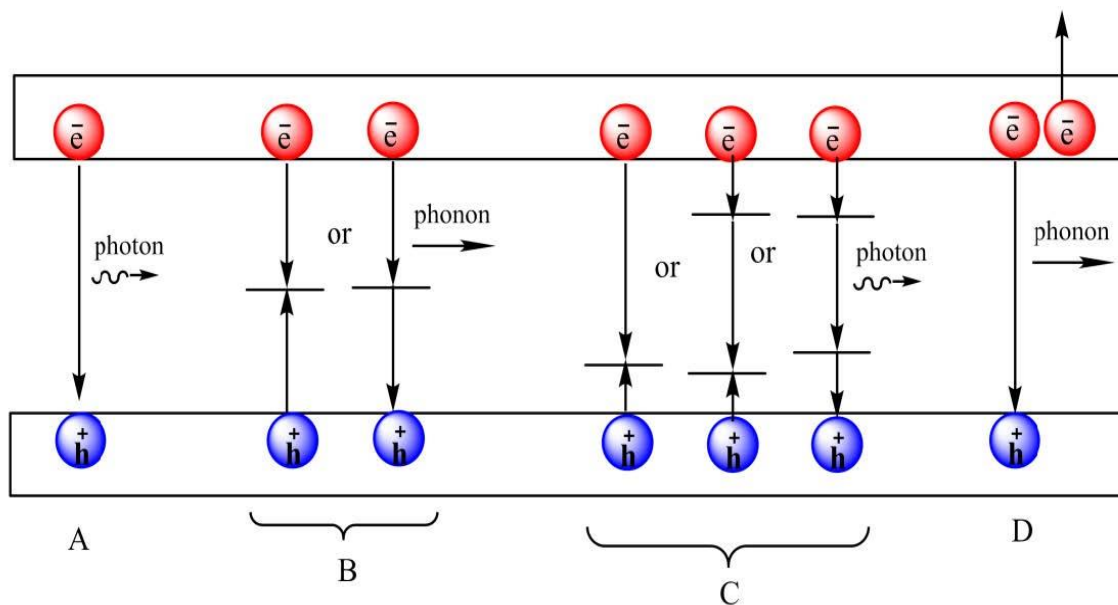
Figure(1-9). Schematic diagram for the common recombination kinds. A. Direct recombination (band-to- band recombination). B. Volume recombination (centers recombination or Trap-assisted recombination). C. Surface recombination (recombination of an exciton). D. Auger recombination [38].

1.6 Unique Nanomaterial Features

In aggregate, these properties have made nanoscale materials attractive for a broad variety of applications, significantly improving the performance of a variety of devices and materials across a variety of disciplines. Numerous nanoparticles are discussed in detail, along with their characteristics and applications in a variety of areas.

Table(1-1). Some nanomaterial features.

	feature	the details
1	Surface area	The surface areas of nanomaterials are generally substantially high compared with their bulk counterparts, and this property is associated with all nanomaterials.[39]
2	Magnetism	The magnetic behavior of elements can change at the nanoscale. A non-magnetic element can become magnetic at the nanoscale level.[40]
3	Quantum effects	Quantum effects are more pronounced at the nanoscale level. However, the size at which these effects will appear strongly depends upon the nature of the semiconductor material.[41]
4	High thermal and electrical conductivity	According to the nature of the nanomaterial, extraordinary thermal and electrical conductivity can be exhibited at the nanoscale level compared to bulk counterparts. One example of this is graphene attained from graphite.[42]
5	Excellent mechanical properties	Nanomaterials exhibit excellent mechanical properties that are absent in their macroscopic counterparts.[43]
6	Excellent support for catalysts	2D sheets of various nanomaterials have provided the opportunity for the good dispersion of nanoparticles of active catalyst, enhancing the catalyst performance substantially.[44] Recently, catalysts have been atomically dispersed on 2D sheets of nanomaterials to boost performance.[45]
7	Antimicrobial activity	Some nanomaterials possess antiviral, antibacterial, and antifungal properties and have an excellent capacity to deal with pathogen-related diseases.[46,47]

1.7 ZrO$_2$ and Spinel CoCr$_2$O$_4$ as Photocatalysts:

1.7.1 Zirconium Oxide (ZrO$_2$)

The ZrO$_2$ nanoparticles have attracted a lot of attention due to their various potential applications [48] and also contribute significantly to photocatalysis research because of their have a high surface-to-volume ratio [49]. ZrO$_2$ is regarded as an n-type semiconductor with a bandgap of 5.0 eV (248 nm) and exhibits excellent photocatalytic activity when exposed to UV light [48]. The photogenerated charge carriers have a broad bandgap, which gives them a high redox ability. ZrO$_2$ has three distinct crystalline forms at atmospheric pressure: monoclinic (1170 °C), tetragonal (between 1170 °C and 2370 °C), and cubic (> 2370 °C). Additionally, it possesses infrared frequencies that are distinct from cubic (480 cm^{-1}), tetragonal (435 cm^{-1}), and monoclinic (270 cm^{-1}) forms. This implies that the optical phonon energy of ZrO$_2$ is structure-dependent [50]. The large uses of ZrO$_2$ nanoparticles are highly dependent on their crystalline structure and phase transitions. ZrO$_2$ nanoparticles have very low thermal conductivity and a high coefficient of thermal expansion [51,52]. Additionally, these materials have a variety of technical uses because of their high strength, durability, superior wear resistance, stiffness, and resistance to thermal stress material [53]. However, owing to its bandgap (5 eV), hence, the visible area light absorption is limited, photo-excited charge carrier separation is limited, and photo-generated charge carrier recombination is rapid, and limiting its use as an effective solar photocatalyst material. To address the aforementioned issues and to enhance the photocatalytic activity of the material, doping with transition metal ions is an efficient approach with improving the physico-chemical characteristics especially the bandgap energy under visible light [54,55]. Moreover, the addition of dopant ions may promote the adsorption of organic pollutants onto the surface of the semiconductor, thus increasing the

host material's catalytic activity. Additionally, the crystallite size, phase purity, dopant type, and synthesis method may all affect the oxides' photocatalytic activity [56].

1.7.2 Spinel Cobalt Chromite ($CoCr_2O_4$)

Spinel nanomaterial is a significant material that has attracted a lot of attention.

There are three distinct kinds of spinel structures, each of which has the general formula AB_2O_4, where A and B denote tetrahedral and octahedral sites coordinated by oxygen atoms, respectively[57].

1-normal spinel, divalent cations prefer the A site, whereas trivalent cations choose the B site such as $CoCr_2O_4$ and Mn_3O_4 .

2-inverse spinel, divalent cations prefer one of the B sites, whereas trivalent cations alternate between the A and B sites such as Fe_3O_4 and $NiFe_2O_4$.

3-mixed spinels, which contain two or more distinct divalent cations dispersed across the A and B sites. It turns out that the magnetic behavior of these compounds depends on the cation type and its distribution in the spinel lattice such $NiAl_2O_4$.

As a consequence, materials' characteristics may be modified for technological purposes. $CoCr_2O_4$, one of the normal spinels, where Co^{2+} ions occupy the A site and Cr^{3+} ions occupy the B sites. It is unique as it not only displays uniform polarization and spatially modulated magnetism but also exhibits uniform magnetization in the conical cycloid state. The conventional spinel cubic structure shows up with two kinds of cation sublattice. In the A sublattice, there are Co^{2+} ions that occupy the tetrahedral (A) sites, and in the B sublattice, Cr^{3+} ions are occupying the octahedral (B) sites[58-60]. As explained in Figure (1-10).

| A | B |
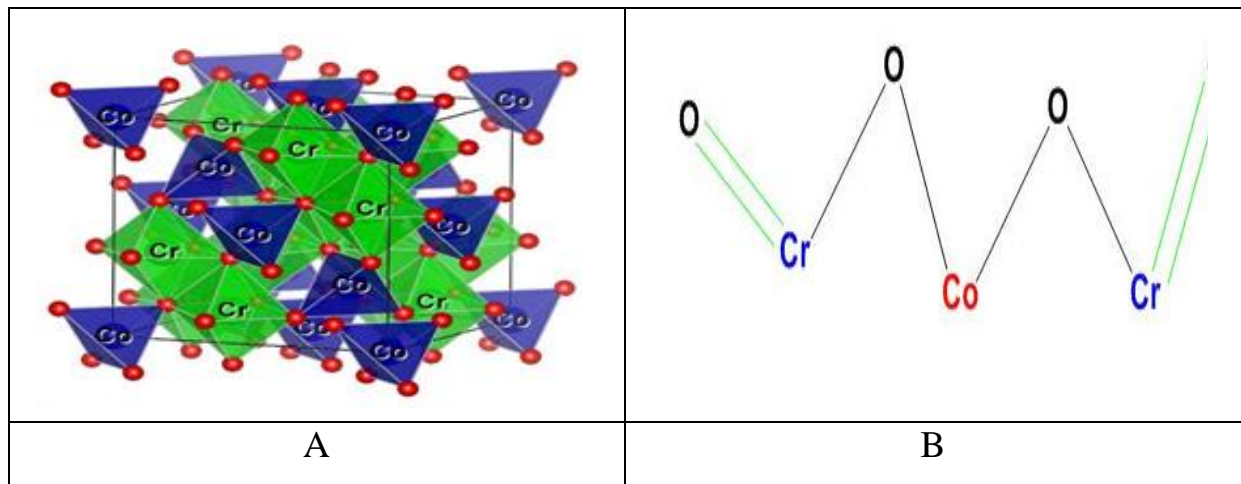
Figure (1-10). A.Crystal structure of $CoCr_2O_4$ conventional cell, B. Structural formula of the spinel $CoCr_2O_4$ [61].

The Magnetic characteristics of the spinel $CoCr_2O_4$ greatly rely on the number of cations that are grouped at sites A and B in the spinel. NP-influenced magnetic characteristics also differ between single NPs and their counter bulk material[62], which is consistent with their lattice distortion, surface imperfections, and the existence of interactions between NPs. When it comes to the family of chromites, cobalt chromite nanoparticles ($CoCr_2O_4$ NPs) have become popular because of their multiferroic characteristics. The spinel $CoCr_2O_4$ has a cubic spinel structure with multiferroicity, and a conical spin ordering has been discovered in this material. Neutron diffraction experiments, conducted down to 11K, have demonstrated the preservation of the cubic phase [63,64]. Due to the conflicting Co-Co, Cr-Cr, and Co-Cr interactions, cobalt chromate nanoparticles undergo three sequential magnetic transitions:

1. At temperature collinear (T_C) 95 K, the magnetic transition from paramagnetic to ferromagnetic(FIM) phase happens;
2. at temperature non-collinear spiral (T_S) 26 K, the magnetic transition from FIM to an incommensurate conical-spiral phase happens;

3. at temperature long-range collinear (T_L) 14 K, the magnetic transition from ferromagnetic (FIM) to an incommensurate conical-spiral phase happens [65].

Following a recent increase in popularity, cobalt chromate ($CoCr_2O_4$) samples have been of interest due to their physical and possible uses[66]. Kind-II multiferroic materials, such as pristine spinel $CoCr_2O_4$ nanoceramics, are a type of material that manifests magnetoelectric coupling as well as two or more ferroic features. Storing charges in electronic memory devices are made much more efficient using these nanoceramics [67]. In recent years, there has been a lot of focus placed on Cobalt Chromite ($CoCr_2O_4$) as a ceramic pigment because of its relevance in both industrial and research applications. Spinel $CoCr_2O_4$ is extensively employed as a plastic colorant, paint colorant, porcelain colorant, and ceramic decoration pigment owing to its chemical and thermal durability, as well as color stability [69-70]. However, just a few studies have looked at the appealing optical features of this ceramic pigment, which will be exploited to make color solar absorber coatings from [71,72]. Spinel $CoCr_2O_4$ ceramic pigments have been synthesized using thermolysis [73] and combustion processes [74]. The sol-gel combustion method is quick and easy to scale up, as it only requires a minimal amount of sol. This method produces pigments that are more homogeneous and have smaller particles. This method produces pigments that are more homogeneous and have smaller particles.

1.8 Methods of Nanomaterials Preparation

There are many common procedures to prepare nanomaterial that include

a. Physical methods (Top-down approach); depended on the transfer of the material size from micro to the nanosize such as mechanical milling, Leaser ablation, ultrasonic. etc.

b. Chemical methods(Button – up approach); depended on the transfer of the material size from Angstrom to the nanosize such as co-precipitation, sol-gel, hydrothermal, solvo-hydrothermal…etc

c. Mixed from the top mention approach such as prepared certain material by co-precipitation then incorporated it with other material using ultrasonic waves. In this work, the spinel was prepared by coprecipitation then combined with zirconia using ultrasonic waves, so, the principles of co-precipitation and ultrasonic will display in this chapter[75,76].

1.8.1 Co-precipitation Method

The most common approach for the synthesis of nanomaterials is co-precipitation. Nanoparticles are formed when aqueous solutions of raw materials are co-precipitated. This technique involves the heat breakdown of solids and the precipitation of their constituents. The whole process is divided into four stages: i)particle nucleation, ii)growth, iii)coarsening, and vi)agglomeration. For the production of monodispersed nanoparticles, the nucleation and development stages must be well regulated. Both the nucleation and synthesis stages may be regulated by modifying the reactant mixture ratio, the reaction parameters, adding surfactants, changing the solvent, and changing the injection sequences. Particles with relatively rapid nucleation and growth rate have resulted in monodispersed nanoparticles[77]. The slow growth mode results in the Oswald ripening of nanoparticles' molecules, while the rapid growth mode results in a scattered distribution of nanoparticles' sizes and an uneven morphology. During the Oswald ripening phase, smaller particles vanish while larger particles continue to develop. This tendency is attributed to molecules that are the least stable on the particle surface. Within the particles, the molecules are already packed and well-ordered. Due to the decreased volume-to-surface ratios of the big particles, low energy states are produced.

When a process tries to save energy, molecules on the surface of smaller particles diffuse into the solution and connect to the larger particles[78].

Co-precipitation is a commonly utilized technique in biomedical applications since it utilizes less toxic ingredients and procedures. This technique produces metallic nanoparticles from aqueous salt solutions by adding base materials such as NaOH, Na_2CO_3, or NH_3 to the solution at ambient temperature in an inert environment. The particle size and shape are depended on the salt type, the pH value, the reaction temperature, the stirring rate, the dripping speed of the basic solution, and the media's ionic strength. Occasionally, co-precipitation results in particles with a broad size distribution, necessitating the selection of secondary sizes [79]. It has high reaction speed, lower equipment requirements, improved performance of the prepared powder, high activity, and purity, and is a common method for preparing nanoparticles [80]. However, owing to the nonuniformity of the reaction, products with uniform performance can not be produced. Simultaneously, co-precipitated ions are tiny in size and exhibit significant agglomeration, making further separation problematic [81,82], used ultrasonic-assisted with co-precipitation to develop a technique for producing nanoparticles with a homogeneous particle size distribution and a good performance at low temperatures. When co-precipitation was combined with ultrasonic irradiation, the chance of getting a single spinel phase was greatly boosted, according to the results[83]. As a consequence, it is clear that incorporating ultrasound-assisted technology into the co-precipitation process may result in outstanding outcomes. As shown in Figure(1-11).
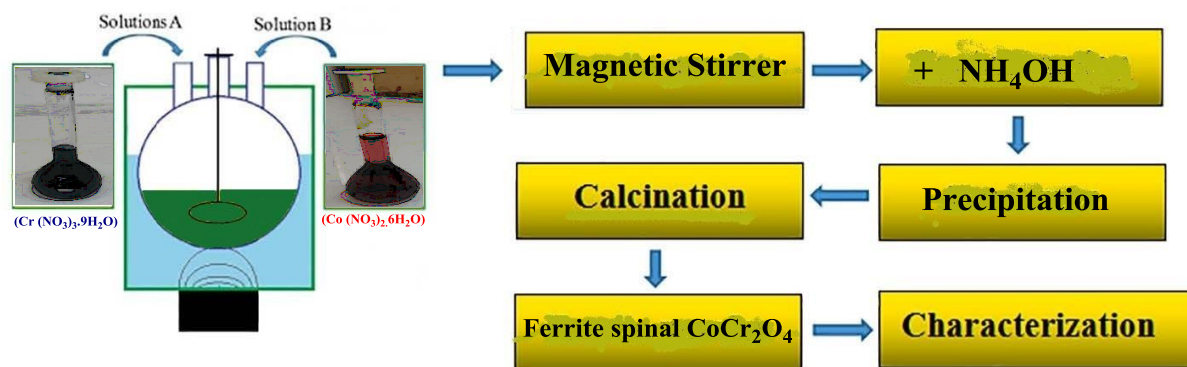
Figure (1-11). Schematic depiction of the synthesis of CoCr₂O₄ by co-precipitation and ultrasonic irradiation.

1.8.2 Ultrasonics Method

Ultrasound is a kind of acoustic wave that facilitates various chemical processes by causing chemical damage during the sonication process, resulting in the development, creation, and implosion of bubbles. Its acoustic cavitation event inside the liquid solution [84-86]. When ultrasonic waves were employed in conjunction with any solution, the reaction conditions, such as a change in vapor pressure, bubbles burst due to transitory pressure with the temperature were observed [87-89]. There are two kinds of transition of ultrasonic irradiation to be usual in the preparation method:

1. Indirect ultrasonic irradiation, as shown in Figure (1-12) (a). When the transducer's ultrasonic irradiation reaches the target solution after passing through the mediator fluid (i.e. water).

2. Direct ultrasonic irradiation, the ultrasonic transducer is in direct touch with the reaction vessel. The transducer may be connected to the reactor's bottom (Figure 1-12 (b)) or positioned inside the reactor (Figure1-1 2 (c)).
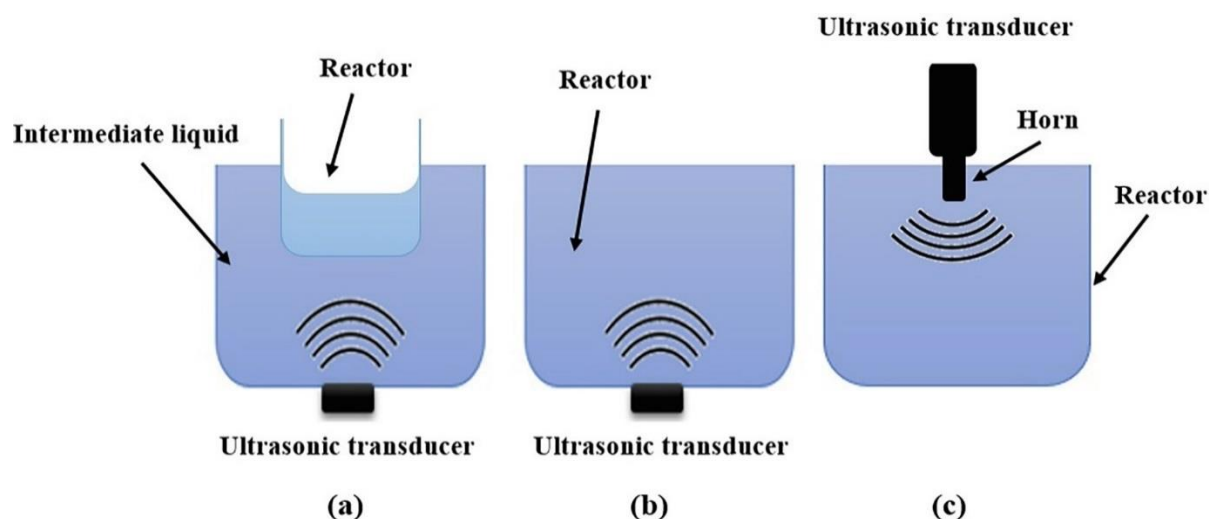
Figure (1-12). (A)Indirect ultrasonic irradiation, (B)direct ultrasonic irradiation in a bath,(C) and direct ultrasonic irradiation using a horn [90].

The ultrasonication-assisted synthesis of nanocomposite materials has piqued people's interest all over the world nowadays, Because of its broad range of applications in a variety of fields such as medicine, chemistry, industry, and the environment[89,91]. Specific research indicated that ultrasonic treatment might be used to manufacture nanoparticles [92]. While others demonstrated that the particle size remained constant at 10 nm and could not be further decreased by raising the ultrasound strength above a certain amount [93]. The large process of ultrasound particle refining may be qualitatively described in terms of acoustic radiation force and ultrasonic cavitation effect [93,94]. However, the quantitative connection between ultrasonic conditions and particle size has not been completely disclosed for the production of metal nanoparticles. Based on its frequency, ultrasound is categorized as power ultrasound[95] to three frequency ranges.

a. low-frequency ultrasound (20–100 kHz).
b. high-frequency ultrasound (100 kHz–1 MHz).
c. diagnostic ultrasound (1–500 MHz).

In general, chemical systems use ultrasound with a frequency range of 20 kHz–100 kHz [94]. By transmitting ultrasound through water or a variety of other liquids, areas of high and low pressure are produced inside the liquid as a result of the ultrasound's periodic expansion and compression [97]. This phenomenon obtains in liquid mediums and results in the creation, growth, and collapse of bubbles [98]. During the expansion of the ultrasound, little bubbles are formed. Moreover, the produced bubbles expand as a result of the energy absorbed during the alternating compression and expansion cycles [99]. Finally, the bubbles reach a threshold size and quickly disintegrate after a few acoustic cycles. It may be expected that virtually little heat transmission occurs between the interior of the bubbles and the surrounding medium during the bubbles' rapid transitory collapse. As a result, the pressure and temperature inside the bubbles' cores increase to several hundred atmospheres (1000 atm) and thousands of Kelvins (5000 K) [99].

Ultrasonic therapy has several benefits, including high frequency, excellent directionality and transmissibility, a high energy concentration, high reflectivity, and ease of use. Historically, ultrasonic treatment has been extensively utilized to synthesize a variety of nanomaterials and their composites, including metal nanoparticles, colloidal sols, catalytic materials, and proteins [100]. Despite the widespread use of ultrasound, the process by which ultrasound influences the size and dispersibility of particles remains poorly understood. When metal nanoparticles are produced, their sizes may range from a few nanometers to the micron scale, depending on the material systems, reaction processes, experimental settings, dispersants, and other solution additives [101].

1.9 Luminol

The chemical reagent Luminol with the IUPAC name (5-amino-2,3-dihydro-1,4-phthalazinedione) is employed in forensic, environmental, biomedical, and

clinical sciences. It's most commonly used in crime scenes to illuminate bloodstains that aren't immediately apparent to the human naked eye.

Luminol's chemiluminescence is catalyzed by the hemoglobin that is found in blood and has been utilized as a very sensitive forensic test for blood. Luminol has a strong reaction with some types of reagents, including strong reducing agents, strong oxidizing agents, strong acids, and strong bases. According to a report[102]. Only oxygen and a strong base are required for luminol chemiluminescence in aprotic media (dimethylsulphoxide or dimethylformamide), whereas in protic solvents (water, water -solvent mixtures, or lower amount of alcohols), various oxygen derivatives such as (molecular oxygen, peroxides, superoxide anion) can oxidize luminol derivatives but require a catalyst, either enzymes or mineral photocatalysts[102]. The mechanism of the luminol light-emitting process has appeared in (figure1-13). The oxidation of the luminol process starts with the excitation of an intermediate molecule, which creates light when it returns to its ground state [103].
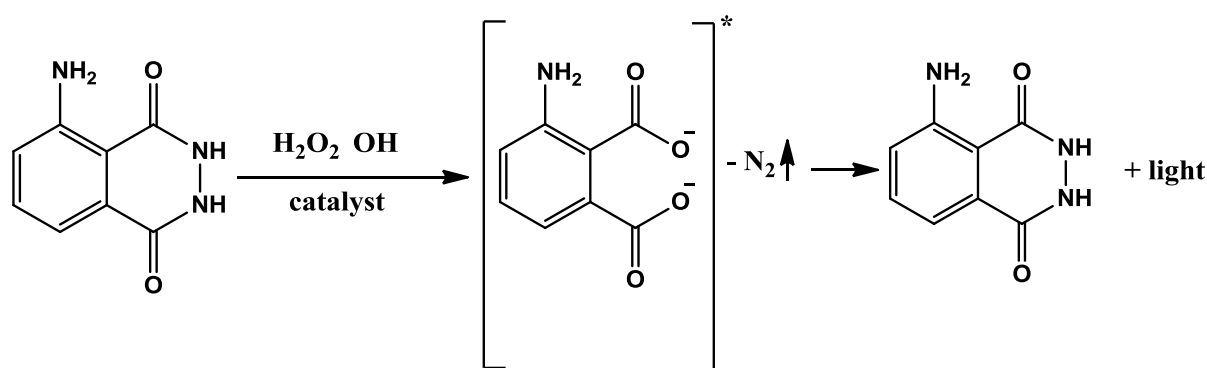
Figure (1-13). The luminol light-emitting process under using a catalyst[101].

Because luminol light-emitting and reacted with a trace amount of iron hence, it is extensively employed in forensic research to identify blood traces due to the iron in the hemoglobin protein catalyzing this reaction. Albrecht invented

luminol chemiluminescence in 1928 [104] and it has since been the subject of many basic investigations, as well as the creation of commercial analytical test kits [104]. The main drawback of employing luminol is to detect the blood include false-positive findings, a lack of specificity, and a dark environment. As a result, it is necessary to discover more stable chemiluminescence chemicals [102].

1.10 Photocatalytic Degradation of Colored Materials

At the moment, photocatalysis is one of the most effective ways of degrading the organic colored compounds such as dyes, organic ligands, and metal-organic ligands complexes through the production of Reactive Oxygen Species (ROS) [105]. While photocatalytic processes seem to be a very promising technique for the treatment of endocrine-disrupting chemicals (EDCs) such as household chemicals, fabrics treated with flame retardants, cosmetics, lotions, products with fragrance, and anti-bacterial soaps, their efficacy is largely dependent on the photocatalysts' performance [106]. In the aquatic environment, photodegradation is a significant abiotic degradation process [107]. Numerous research has been conducted in recent years to eradicate these contaminants using optical catalysts, with the conclusion that a photocatalytic degradation process is an eco-friendly approach that does not result in secondary contamination. During light exposure, photocatalysts and electron-hole pairs were generated which are now participating in the process of accelerating dye degradation [108]. Furthermore, under specified conditions, such as temperature, pressure, and concentration, extremely safe and effective photocatalytic technologies are utilized to eliminate chlorinated phenolic chemicals. Generally, the by-products of the photocatalytic process are benign or have low toxicity [109]. Direct photo-breakdown in aquatic conditions, like dye degradation, is a key mechanism for pesticide degradation [110]. In

summary, photo-degradation encompasses processes such as photo-chemical mineralization, photo-priming, and microbial photo-inhibition [111].
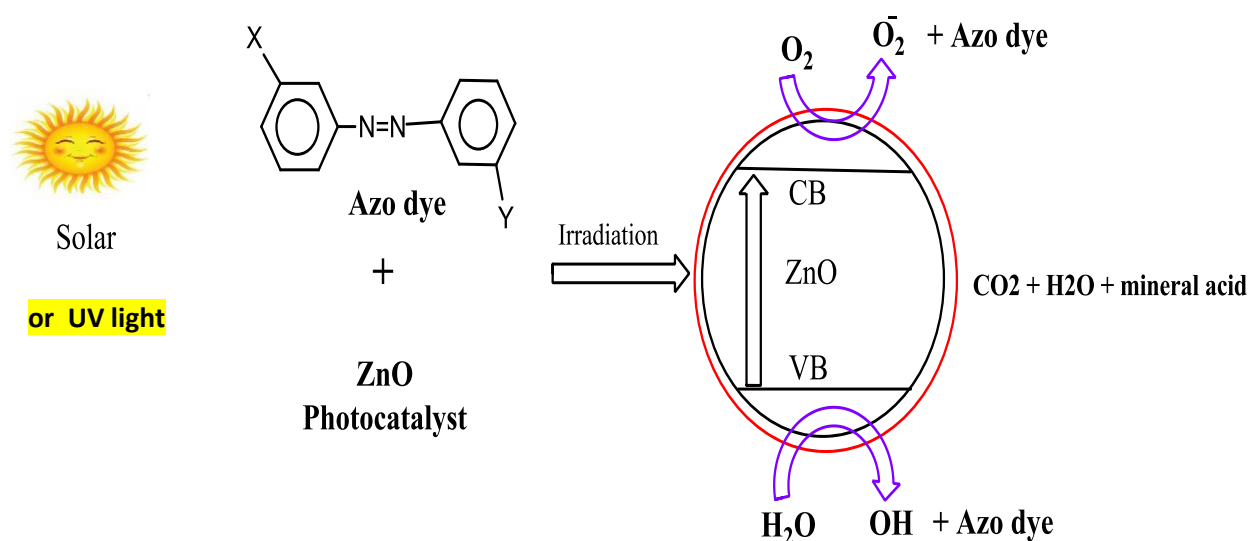
Figure (1-14). A schematic illustration of the photocatalytic mechanism.

Thus, heterogeneous photocatalysis is a very effective method for resolving environmental crises [112]. It has paved the path for the creation of novel semiconductor photocatalysts capable of performing photochemical processes, as displayed in Figure (1-14). However, the high recombination rate of photo-generated electron-hole pairs produced during the photo-degradation process restricts the effective degradation. To circumvent the quick recombination of photogenerated electron-hole pairs, a variety of research methods have been suggested for the preparation of CuO, ZnO, Fe, and TiO_2 nanoparticles coated with supporting materials for the removal of organic dyes [113].

While semiconductor materials with a bandgap energy of less than 2.5 eV are effective under solar or day sunlight, those with bandgap energy higher than 2.5 eV may be utilized as photocatalysts under UV light for the dye degradation process [114]. However, semiconductor photocatalysts with band gaps of 2. 3 eV may be effective in both ultraviolet and solar radiation. Recent research has

concentrated on the production of semi-conductors and on coupling them to low bandgap energy substrates to create UV-active catalysts with an enhanced surface and catalytic activity. In the case of semiconductor nanoparticles, photocatalytic reactions are inhibited primarily owing to nanomaterial aggregation, decreased adsorption capacity, decreased surface area, and the catalyst's recyclability. To address these limitations, porous materials such as silica, alumina, activated carbon, fly ash, and MCM are employed as supports for metal sulfide or metal oxide photocatalysts. As a result, the catalysts' specific surface area and adsorption efficiency were increased [115]. The general dye degradation process of a semiconductor nanocatalyst composed of tertiary metal oxides ($ZnO/TiO_2/Ag_2O$) is shown in Figure (1-15). To make ZnO a semiconductor material suitable for use as a solar active catalyst, it may be coupled with other materials having a small bandgap, such as Ag_2O.
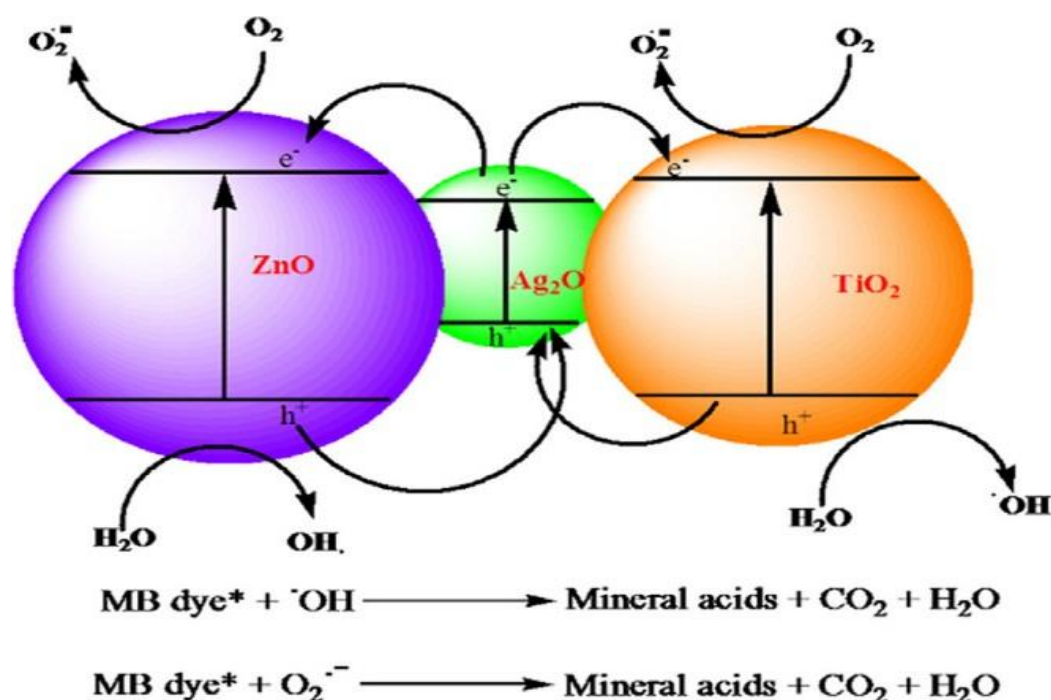
Figure (1-15). The general process of dye degradation by a semiconductor nanocatalyst composed of tertiary metal oxides ($ZnO/TiO_2/Ag_2O$) [115].

1.11 Literature Review for the Synthesis of Spinel $CoCr_2O_4$, ZrO_2 and Luminol.

There are many recent literature review for synthesis of photocatalyst. L.G. Wang and co-workers [116] in 2017, investigated the exchange bias effect in $CoCr_2O_4$/NiO system prepared by a two-step method. $CoCr_2O_4$/NiO has been successfully synthesized through a two-step method. X-ray diffraction results present the coexistence of $CoCr_2O_4$ and NiO with pure formation. Micrographs measured with a scanning electron microscope and transmission electron microscope display the homogeneous and dense morphology with two kinds of nanoparticles. Also, Yuting Hao and co-workers [117] in 2017, prepared the Multilayer and open structure of dendritic crosslinked CeO_2-ZrO_2 composite: enhanced photocatalytic degradation and water splitting performance. Using polystyrene spheres and $EO_{20}PO_{70}EO_{20}$ as double templates, a three-dimensionally ordered macroporous (3DOM) CeO_2-ZrO_2 material was synthesized by the sol-gel method combined with the decompression filling method. The composition, structure, morphology, and surface physicochemical properties of the material were characterized by XRD, XPS, UV-Vis/DRS, SEM, TEM, HR-TEM.

E. Berei and co-workers [118] in 2018, reported a novel route for the preparation of $CoCr_2O_4$/SiO_2 nanocomposite starting from Co(II)–Cr(III) carboxylate complex combinations. Preparation and characterization of the spinel $CoCr_2O_4$. In order to obtain 20% $CoCr_2O_4$/80% SiO_2 and 50% $CoCr_2O_4$/50% SiO_2 (mol%) nanocomposites, His used a versatile pathway based on the thermal decomposition of some particular precursors, Co(II) and Co(III) carboxylate-type complex combinations, inside the SiO_2 matrix. . Eunpyo Hong and co-workers [119] in 2018, Catalytic methane combustion over Pd/ZrO_2 catalysts: Effects of crystalline structure and textural properties. Zirconia supports were synthesized via a precipitation method, and the effects

of crystalline structure and textural properties of ZrO_2 on the methane combustion reaction were investigated using the Pd/ZrO_2 catalysts. Jun-Ying Huang and co-worker [120] in 2019, reported the Synthesis and characterizations of $CoCr_2O_4$ /C composite using high energy ball-milling technique as novel anode materials for Li-ion batteries. synthesize $CoCr_2O_4$/C composite (CCO/CB) as novel anode materials for Li- ion batteries by using hydrothermal reaction and high energy ball milling technique. The crystal structure and surface morphologies of as-prepared samples are carried out by X-ray diffraction (XRD), scanning electronic microscopy (SEM). Eunpyo Hong and co-workers [121] in 2019, published the Methane decomposition and carbon deposition over Ni/ZrO_2 catalysts: Comparison of amorphous, tetragonal, and monoclinic zirconia phase. The influence of the crystal phase of ZrO_2 on the catalytic performance of methane decomposition and the properties of deposited carbon on Ni/ZrO_2 catalysts was investigated. Ni/ZrO_2 catalysts were prepared by incipient-wetness impregnation method with 5% Ni loading, using amorphous, monoclinic, and tetragonal ZrO_2 as supports.

 K. Nadeem and co-workers [122] in 2020, have done Magnetic phase diagram and dielectric properties of Mn-doped $CoCr_2O_4$ nanoparticles. Effects of Manganese (Mn) substitution on the magnetic and dielectric properties of spinel phase $Co_{1-x}Mn_xCr_2O_4$ $(0.0_{\_x\_1})$ nanoparticles (NPs) have been studied. X-ray diffraction and Fourier transform infrared spectroscopy analysis showed the normal spinel structure for all the samples. Meng Zhang and co-workers [123] in 2020, have done Effects of the surface adsorbed oxygen species tuned by rare-earth metal doping on dry reforming of methane over Ni/ZrO_2 catalyst. the effects of the surface adsorbed oxygen species tuned by doping with different rare-metal metals (such as Ce, La, Sm, and Y) on the catalytic behavior were elaborated systematically.

There are many recent literature review for Luminol.

K. L. Lin and co-workers [124] in 2017, reduced Luminol and gold nanoparticle-co-precipitated on graphene oxide hybrids with long-persistent chemiluminescence for cholesterol detection. Herein, dual-functionalized reduced graphene oxide (rGO) hybrids (rGO/AuNP/luminol) with gold nanoparticles (AuNPs) and luminol were prepared *via* π–π conjugation and electrostatic interaction. the proposed method was successfully exploited for the determination of cholesterol in human serum samples.

L. Zhang and co-workers [125] in 2018, reported procedure for Silicon quantum dot that involved luminol chemiluminescence and its sensitive detection of dopamine. Water dispersible silicon quantum dots (SiQDs) were synthesized by *in situ* growth under microwave irradiation. The prepared SiQDs were characterized by transmission electron microscopy, FT-IR, and fluorescence spectroscopy. Under neutral conditions, a weak chemiluminescence (CL) signal was obtained in luminol/$K_2S_2O_8$ and SiQDs/$K_2S_2O_8$ mixed solutions, while a strong CL signal was obtained in the presence of luminol, $K_2S_2O_8$, and SiQDs. The CL spectra revealed that two luminophores were involved in the present CL system.

 L. Yue and co-worker [126] in 2020, reported manuscript in Mechanistic Insight into pH-Dependent Luminol Chemiluminescence in Aqueous Solution. Luminol is one of the best known chemiluminescent cyclic hydrazides used in basic solution. Owing to the complexity of luminol oxidation, the mechanism of luminol chemiluminescence (CL), especially in aqueous solution, has not yet been fully elucidated.

1.12 The Aim of the Study

The scope of this work is aimed to:

1. Prepare a Luminal reagent, Luminol- tyrosine as a ligand, and then created a Fe(II)-(Luminol-Tyrosine) complex.

2. Study the characterization of prepared reagent, ligand, and FeL_2Cl_2 complex by Uv-Visible spectra, FT-IR-spectra, ^1HNMR spectra, magnetic sensitivity, Elemental Micro Analysis (C.H.N) and melting point.

3. measure the metal: ligand ration using mole ratio method, and then calculate the stability constant.

4. Prepare of the Spinel $(CoCr_2O_4)$, then calcination at 600 °C.

5. Prepare spinel $CoCr_2O_4$ /ZrO_2 composites in different ratios.

6. Study the properties of the prepared spinel $CoCr_2O_4$, commercial ZrO_2 and spinel $CoCr_2O_4$/ZrO_2 composites by X-ray diffraction (XRD), Scanning Electron Microscopy (SEM) spectra, energy dispersive X-rays (EDX) and Band gap (Bg).

7. Investigate the photocatalytic activity for the commercial ZrO_2, prepared Spinel $CoCr_2O_4$, and prepared $(CoCr_2O_4/ZrO_2)$ composite by studying the effect of the following parameters on colored material (FeL_2Cl_2 complex):

a. weight of the catalyst.

b. Temperature.

c. Initial pH of a solution.

CHAPTER TWO

Experimental

2.1 Chemicals

In this job work, the chemicals used as tabulated in Table (2-1), were used without purification.

Table (2-1): Used chemicals

No.	Chemicals	Company supplied	Purities
1.	Absolute ethanol (C_2H_5OH)	Carlo erba, France..	(99.9) %
2.	Acetic acid (CH_3COOH)	BDH company, Enghand	99.9%
3.	Ammonia solution (NH_4OH)	CDH, India	99%
4.	Chromium nitrate nonahydrate ($Cr(NO_3)_3.9H_2O$)	BDH company, Enghand	99.9%
5.	Cobalt nitrate hexahydrate ($Co(NO_3)_2.6H_2O$)	BDH company, Enghand	99.9%
6.	Diethylene glycol(D.E.G) $C_4H_{10}O_3$	BDH company, Enghand	99%
7.	Dimethyl sulfoxide (DMSO) $SO(CH_3)_2$	Carlo erba, France	(99.99) %
8.	Ferrous chloride trihydrate $FeCl_2 \cdot 2H_2O$	CDH, India	99%
9.	Hexadecyltrimethylammonium bromide(CTAB) $C_{19}H_{42}NBr$	CDH, India	99%
10.	Hydrazine(80%) (N_2O_4)	BDH company, Enghand	99.9%
11.	Hydrochloric acid (HCl) (36.5-38.0) %	J. K. Baker, Netherlands.	(98-99) %
12.	Iron (II)sulfate heptahydrate ($FeSO_4.7H2O$)	Evans, Mf-Dica, England.	(99.98) %
13.	Iron (III)sulfate hydrate ($Fe_2(SO_4)_3.H_2O$)	Evans, Mf-Dica, England.	(99.98) %
14.	3-Nitro-Phthalic Acid ($C_8 H_5 NO_6$)	BDH-England	(99.98) %
15.	1,10- Phenanthroline ($C_{12}H_8N_2$)	Riedel-De-Haen AG, Seelze, Hannover, Germany.	(99.98) %
16.	Potassium hydroxide (KOH)	Sigma Chemical Company, USA	(99.99) %
17.	Potassium oxalate ($K_2C_2O_4.H_2O$)	Riedel-De-Haen AG, Seelze, Hannover, Germany	(99.98) %
18.	Sodium carbonate (Na_2CO_3)	BDH-England	(99) %

19.	Sodium dithionite (Sodium hydrosulphite) ($Na_2S_2O_4 . H_2O$)	BDH-England	(99.99) %
20.	Sodium dithionite ($Na_2S_2O_4$)	BDH company, England	(99.99) %
21.	Sodium hydroxide (NaOH)	Sigma Chemical Company, USA	(99.98) %
22.	Sodium nitrite($NaNO_2$)	CDH, India	99%
23.	Sulphuric acid (H_2SO_4)	CDH, India	(97.98) %
24.	Tetraethylene glycol(T.E.G) $C_8H_{18}O_5$	BDH company, England	99%
25.	Tyrosine ($C_9H_{11}NO_3$)	Sigma Chemical Company, USA.	(99) %
26.	Zirconium(IV) oxide, Zirconium dioxide, Zirconia, (ZrO_2)	Riedel-De-Haen AG, Seelze,Hannover, Germany.	(99.98) %

2.2   Instruments

Table (2-2) describes the employed instruments in this study with their companies and places.

Table (2-2): Employed instruments.

No.	Instruments	Companies	Places
1.	Centrifuge	Hettich- Universal II- Germany	University of Kerbala, Science college
2.	Digital pH meter	OAICTON-2100, Singapore	University of Kerbala, Science college
3.	Digital pH meter	740 Inolab WTW, Germany	University of Babylon, Science college
4.	FT-IR Spectrometers	Shimadzu,8400S Japan	University of Kerbala, Science college
5.	FT-IR Spectrometer	Bruker, Germany	University of Babylon, Science college
6.	Furnace	Muffle furnace Size-Tow Gallenkamp, England	University of Babylon, Science college

7.	^{1}H NMR Spectrophotometer	BAMX400 MHZ Spectrophotometer	University of Tehran, Iranian Islamic Republic
8.	High-Pressure Mercury Lamp -UV (A) (400W).	Rudium, China.	University of Kerbala, Science college
9.	Hotplate Magnetic Stirrer	Heido-MrHei-Standard, Germany	University of Kerbala, Science college
10.	Magnetic Measurements	Magnetic susceptibility Balance	Department of Chemistry - College of Science - Al-Nahrain University
11.	Melting point	SMP 30, Sturt, England	University of Babylon, Science college
12.	Microwave oven	Sartorius- Germany	University of Babylon, College of Women Science
13.	Oven	Memmert, Germany.	University of Kerbala, Science college
14.	Scanning Electron Microscopy (SEM)	(kyky EM) 320., USA.	Isfahan University, Iranian Islamic Republic
15.	Sensitive balance	BL 210 S, Sartorius-Germany	University of Kerbala, Science college
16.	Ultrasonic bath	DAIHAN Scientific, Korea.	University of Kerbala, Science college
17.	X-Ray Diffraction Spectroscopy	Lab X- XRD 6000, Shimadzu, Japan	University of Baghdad, Ibn- Al-Haitham, Education college
18.	Elemental Micro Analysis (C.H.N.)	EURO EA 300 C.H.N Element analysis 2012	University of Baghdad, Ibn- Al-Haitham, Education college

2.3   Reactor Set of Photo-Catalysis

Figure (2-1) shows the photocatalytic reactor unit used to perform all photo experiments.
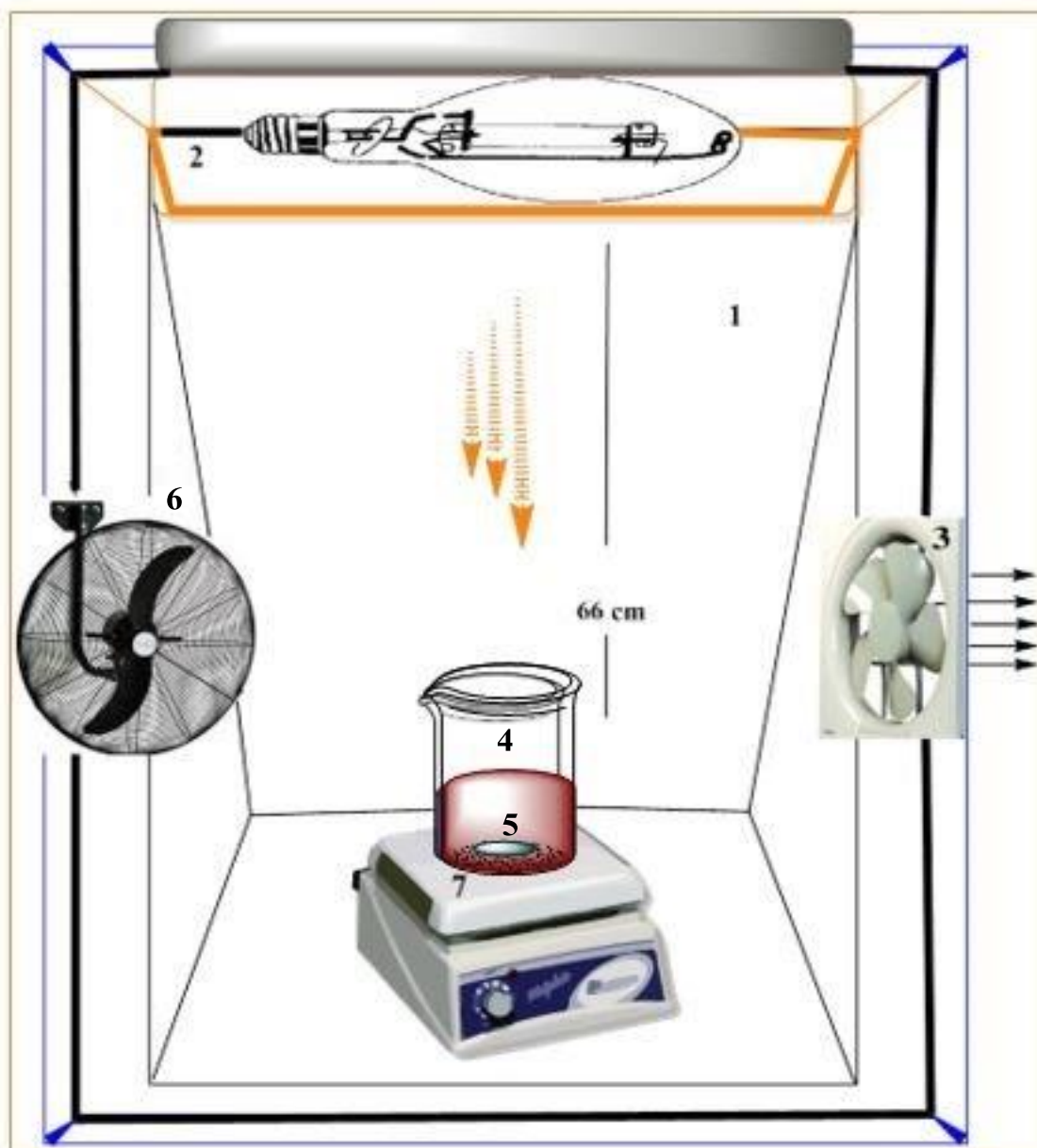
Figure (2-1). Experimental set-up schematic diagram (Photocatalytic Reactor Unit), consisting of a wooden box (1), high-pressure mercury lamp (400 W) (2), vacuum fan (3), beaker 400 cm³ (4), Teflon bar (5), fan (6) and magnetic stirrer (7).

2.4 Preparation (Luminol)

A- In order to prepare the (Luminol), as in the preparation reaction in figure (2-2). A series of steps were done.

1. A 20x150-mm test tube was heated using a bunsen burner, after mixing 1g of 3-nitrophthalic acid and 2 mL of an 8% aqueous solution of hydrazine until the solid is dissolved.

2. Exact 3 mL of tetraethylene glycol (Tetra-E. G) was transferred to the tube and clamp vertically on a bunsen burner.

3. The solution has been forcefully boiled to remove any remaining water (110-130) °C. The temperature was allowed to rapidly climb until it reaches 215 °C for 3-4 minutes. The temperature of this reaction was determined using a thermometer.

4. The heat was turned off, then the time was recorded, and a temperature was maintained of (215-220) °C for 2 minutes using occasional mild heating.

5. the tube of reaction was removed from the burner, then was cooled to about 100 °C (crystals of the product frequently form). The 15 mL of hot water was added, chilled under running water, and collected the light yellow granular nitro compound.

6. A 3 M NaOH solution was added immediately to the uncleaned test tube, which the nitro compound produced inside it, and stirred using a glasses rod, then added 3g of sodium hydrosulfide hydrate ($Na_2S_2O_4 . H_2O$) that leads to form a deep brown-red solution. Wash the edges of the tube with a little water.

7. The solution was heated to the boiling point, stirred, and kept the mixture hot for 5 min, during which time some of the reduction products may separate.

8. 2 mL of acetic acid was added to the solution. Then below, the tap cools and mixes. Gather the resultant yellow luminol was precipitated, filtered more than once, and washed with ethano. The percentage of luminol reagent is (86%).
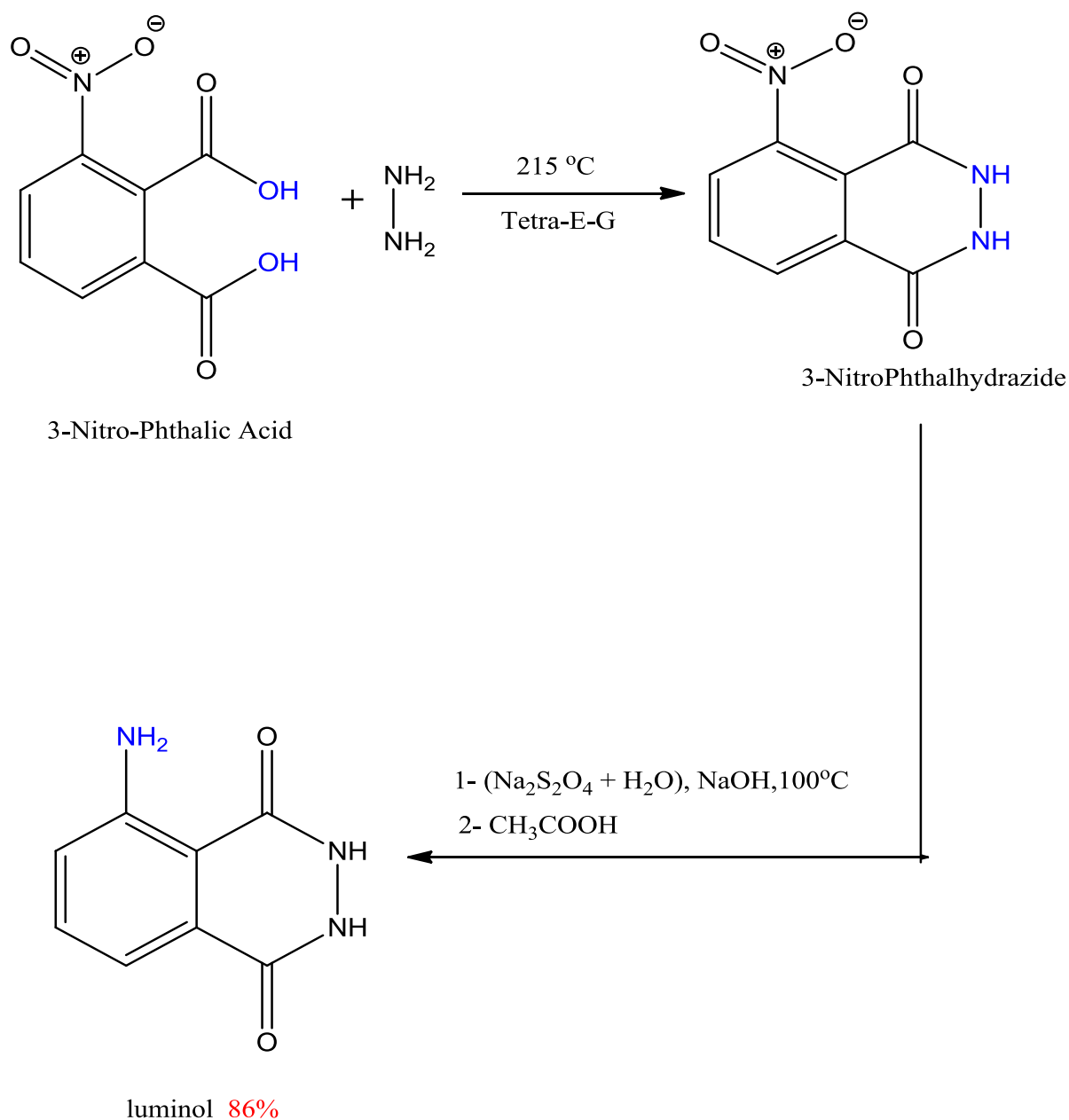
Figure (2-2). The prepared ligand (Luminol)using tetraethylene glycol.

B- In order to prepare the (Luminol) as in the preparation reaction in figure (2-3). A series of steps were done.

1-A solution of 2 mL of 8 % an aqueous solution of hydrazine was added to 1g of 3-nitrophthalic acid, and the resulting solution was heated until the solid was dissolved.

2-Clamp the tube vertically over a bunsen burner and add 2 mL of diethylene glycol (D.E.G).

3. To eliminate all residual water, the solution is heated at a temperature between 110 and 130 °C. Allow the temperature to increase quickly to around 215 °C during the next 3-4 minutes. One way to measure the temperature of the reaction is to use a thermometer.

4. Now that the heat has been turned off, note the time, and maintain a temperature of about 215-220 °C (or 1 or 2 degrees over the target temperature) for 2 minutes with intermittent moderate heating.

5-The tube was cooled to about 100 °C, then 15 mL of hot water was added, the mixture was chilled under running water, and the resulting light yellow granular nitro compound was collected.

6. The uncleaned test tube in which the nitro compound was generated, restored immediately to its original position. Next, to the solution, 5 mL of 3 M NaOH solution was added, stirred by a glasses rod, and then 3 g of Sodium dithionite ($Na_2S_2O_4$) was added to the resulting deep brown-red solution. The edges of the tube were washed with a little amount of water.

7-After boiling for 5 minutes, some of the reduction results may separate.

8. 2 mL of acetic acid was added. Then below, the tap cools and mixes. The resultant yellow luminol was precipitated, filtered more than once, and washed with ethanol . Percentage of luminol reagent **(73%).**
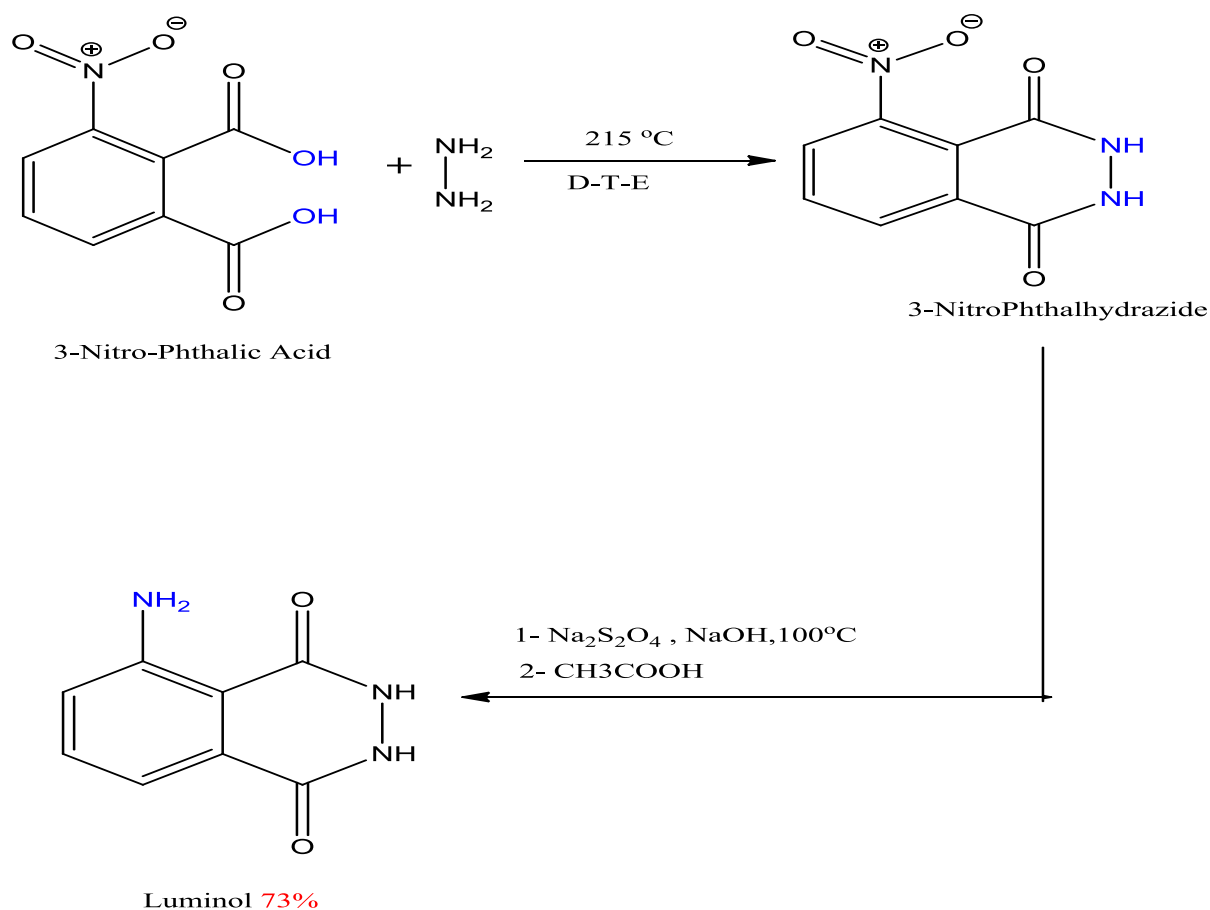
Figure (2-3). The prepared ligand (Luminol)using diethylene glycol.

2.4.1 Preparation (Luminol-Tyrosine)

In order to prepare the (Luminol-Tyrosine) as in the preparation reaction in figure (2-4).

1- (0.7086 g, 0.006 mol) of Luminol was mixed with (2.1mL) of concentrated hydrochloric acid and diluted with a little amount of distilled water (approximately 10 mL), and then stirred this mixture in an ice bath at (5 ^{o}C).

2-(0.4560 g) of sodium nitrate was dissolved in the smallest amount of distilled water possible and put in an ice bath.

3-To create the diazonium salt, the prepared NaNO$_2$ solution in step 2 was very slowly added, as drops to the cold solution that prepared in step (1) under continuously stirring and maintaining the temperature at (5 °C).

4- (0.7247 g, 0.004 mol) from Tyrosine was dissolved with (0.8 g) from sodium hydroxide in 100 mL H_2O.

5-With constant stirring in the ice bath, the generated diazonium salt in step (3) was gently added to the base solution prepared in step (4), and then the resultant solution was chilled for 24 hours to achieve a pH of 7.3.

6- This solution was filtered. The produced precipitate was occurred brown, washed with ethanol, and dried [127], with the percentage of ligand (83%).
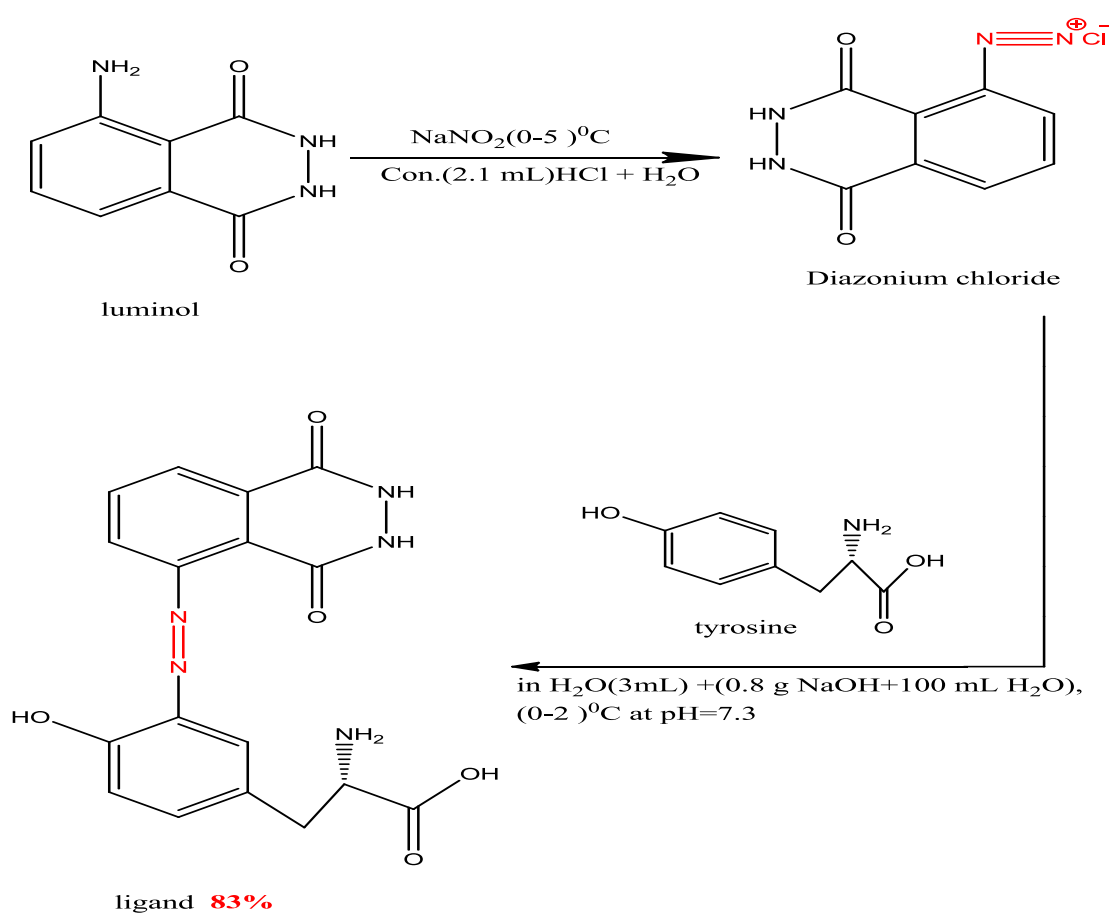
Figure (2-4). The structure of the prepared (luminal - Tyrosine) ligand

2.4.2 Preparation   Fe(II) - (Luminol-Tyrosine) Complex

The (0.01 mol) from (Luminol-Tyrosine) ligand and (0.01 mol) from $FeCl_2.2H_2O$ were well mixed in an agate mortar and then irradiated on the revolving platform of a microwave oven. The irradiation time is complicated at

a duration of ten minutes. The produced was washed repeatedly with ethanol and then dried with washing using ether. This procedure was pictured as the following scheme in figure (2-5) [128].

luminol - tyrosine

$FeCl_2.2H_2O$

ethanol

$$b.p = \frac{W}{4.18}$$
W= 78*4.18
W= 326 $kg \cdot m^2 \cdot s^{-3}$

Microwave irradiation

complex

Fe(ll)-luminol- tyrosine complex
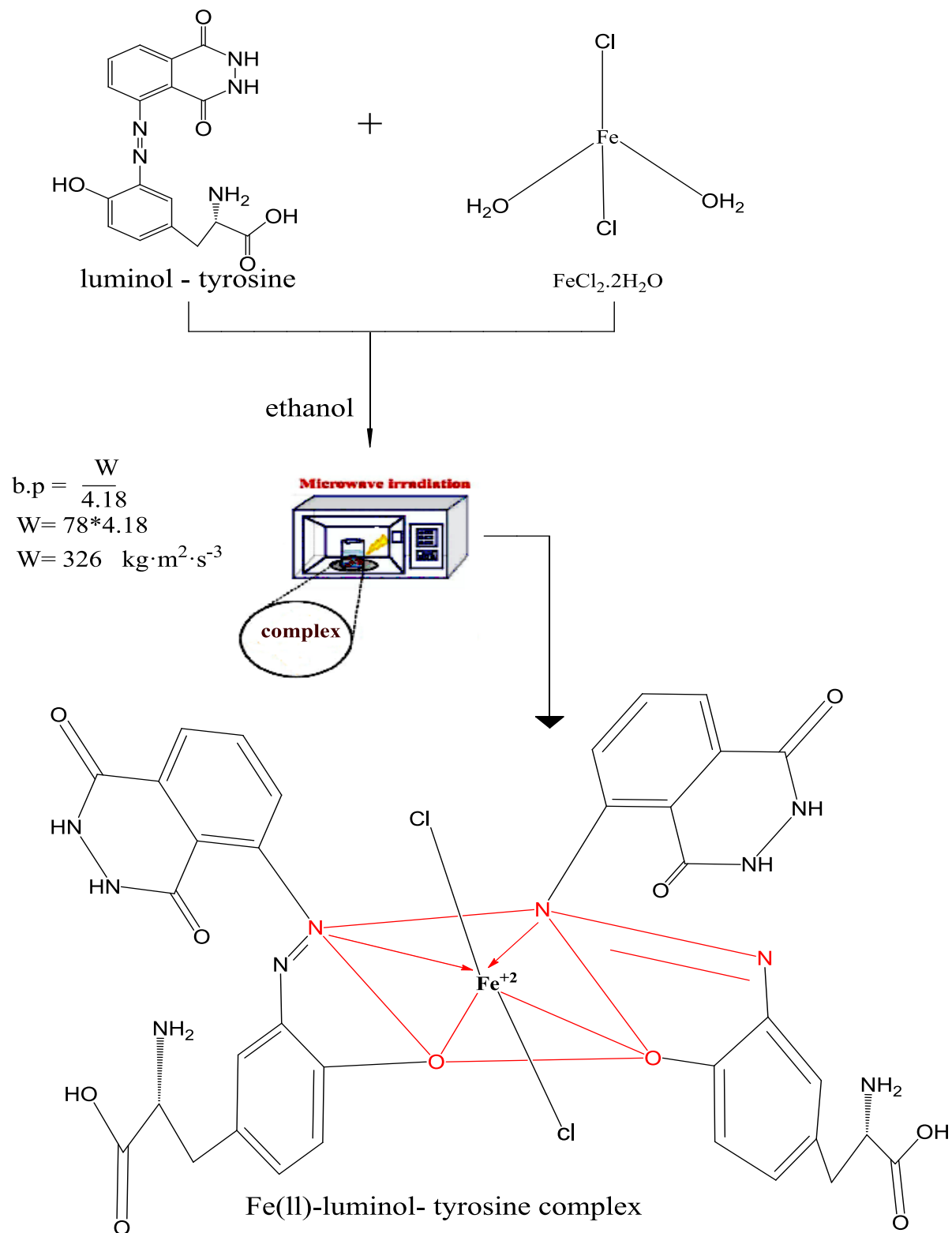
Figure (2-5). The structure of prepared ligand Fe^{2+} -(Lumino - Tyrosine)

40

2.4.3 Physical Property (Melting point)

The melting point for each of the Lumino, Luminal-Tyrosine ligand, and Fe(II) - (Luminal-Tyrosine) complex were measured by using Melting Point Instrument - SMP 30, Strut, England.

2.4.4 Stoichiometric Study and Stability of Complex

The estimation of the Fe-complex structure was proved by employing the mole ratio method [129]. This method is a vital method to determine the ratio of Fe: L and conformed to the produced structure of Fe-Complex. The instability constant ($k_{instability}$) and stability constant ($k_{stability}$) were determined according to the following equations [130]

$$FeL_2 \rightarrow Fe^{2+} + 2\,L \qquad\qquad (2\text{-}1)$$

$$k_{instability} = \frac{[Fe^{2+}][L]^2}{[FeL_2]} \qquad\qquad (2\text{-}2)$$

$$k_{instability} = \frac{\left[1 - \frac{A}{A_{max}}\right]^3}{\left[\frac{A}{A_{max}}\right]} \times C_{Fe^{2+}} \qquad\qquad (2\text{-}3)$$

$$k_{stability} = \frac{1}{k_{instability}} \qquad\qquad (2\text{-}4)$$

Here, A_{max} and A are maximum absorptions of Fe-complex and absorption of Fe-complex at equivalent points respectively. $C_{Fe^{2+}}$ is a concentration of Fe^{2+} at an equivalent point.

2.4.5 UV-Visible Spectroscopy

These spectra were determined for metal, Ligand, and complex by Double – beam UV-Visible-spectrophotometer (Shimadzu) at ranged (190-1000) nm.

2.4.6 ^{1}HNMR Spectrophotometer

The nuclear magnetic resonance spectrometry of the prepared Lumino reagent, ligand, and its complex with iron(ll) ion detector was measured using a device BAMX400 MHZ Spectrophotometer, DMSO as a solvent, and TMS as internal standard.

2.4.7 FT-IR Spectra

The FT-IR spectra of the ligand and complex were obtained using CsI powder in the range (400-4000) cm^{-1} using (FT-IR Spectroscopy, Shimadzu).

2.4.8 Magnetic Susceptibility

The magnetic susceptibility measurements of the complex were carried out at laboratory temperature using the Faraday method by placing the model whose gram-magnet sensitivity is to be measured in a small thermal glass tube hanging from the cuff of a sensitive scale placed between the poles of a strong electromagnet in preparation for obtaining the gram sensitivity value (Xg). To the molar sensitivity (XM) and then to the atomic sensitivity (XA) after extracting the value of the correction factor (D) from tables of Pascal constants, and thus the values of the effective magnetic moment (μ_{eff}) were calculated according to the following law:

$$\mu_{eff} = 2.828 \sqrt{X_A \, T} \; B.M \qquad\qquad (2-5)$$

Here: (XA) = atomic sensitivity, T= absolute temperature

B.M = bur. magneton is a unit of magnetic moment measurement.

2.4.9 Elemental Micro Analysis (C.H.N.)

The ratios of carbon, hydrogen, and nitrogen elements to the reagent, ligand, and complex were determined using the EURO EA 300 C.H.N Element analysis 2012.

2.5 Preparation of the Spinel ($CoCr_2O_4$)

Spinel $CoCr_2O_4$ nanocrystals were synthesized via co-precipitation method. At the outset, cobalt nitrate (0.5M) and chromium nitrate (1M) were prepared in 100 mL ethanol and transferred to an ultrasonic bath at 75 °C for 1 hour.

In the second step, the chromium nitrate solution was put in a beaker with a size of 500 mL, and then cobalt nitrate solution was slowly added to the chromium nitrate solution using an ultrasonic bath at 75 °C for 1 hour.

 In the third step, the generated mixture was stirred and heated at the same temperature for a further two hours using a magnetic stirrer. Following that, 1% hexadecyltrimethylammonium bromide (CTAB) is added to the mixture as a capping agent. A 25% aqueous ammonia solution was dropwise added to the last solution until a pH equal to 9. The produced precipitate was filtered and washed with distilled water and ethanol many times until the filtrate reached to pH of around 7. The deep green precipitate was dried overnight in a desiccator, then calcinated for 4 hours at 600 °C. as in the preparation reaction in figure (2-6).
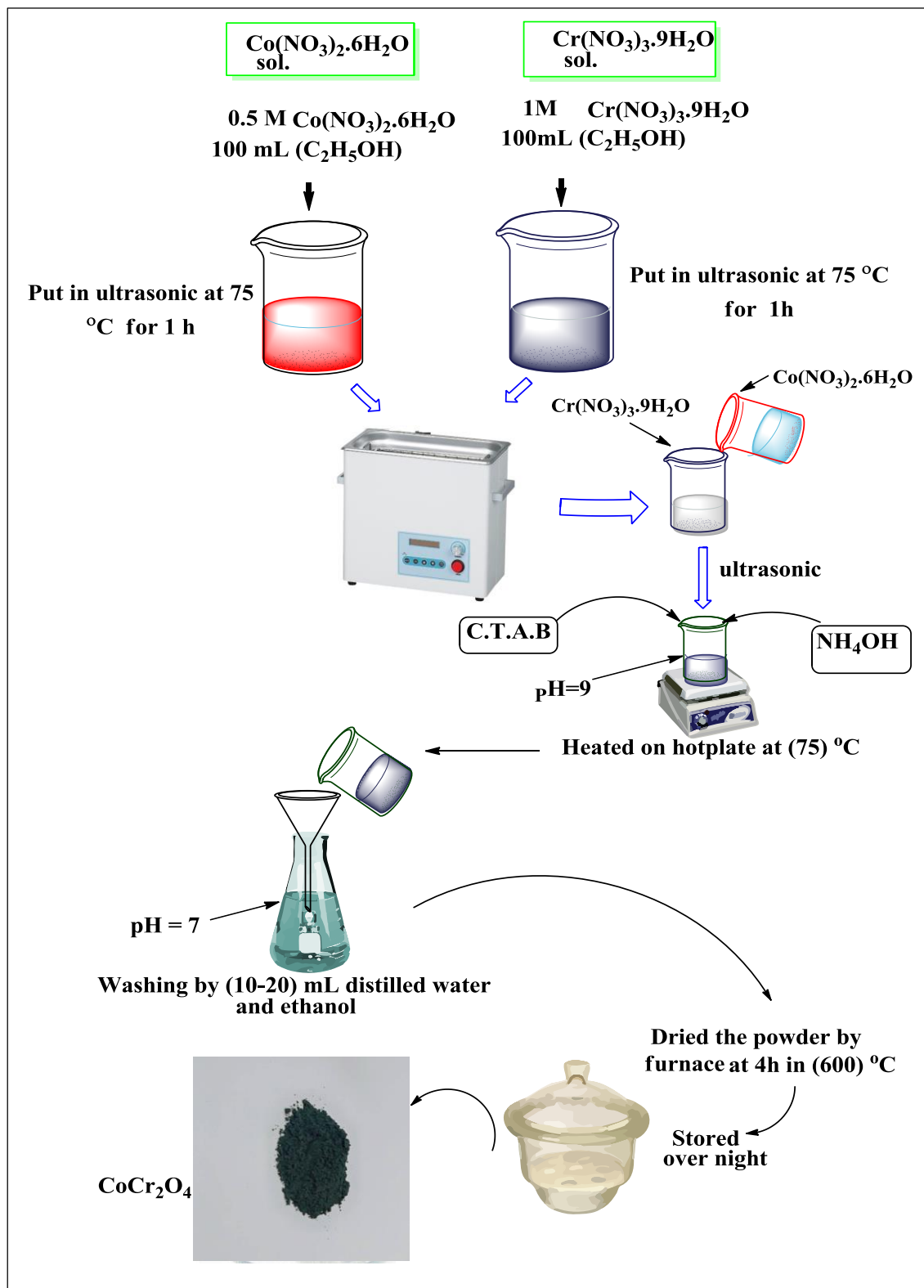
Figure (2-6). Schematic diagram for preparation of spinel $CoCr_2O_4$ nanoparticles.

Equations (2-6) and (2-7) suggested the chemical reaction of spinel.

$$Co(NO_3)_2.6H_2O + 2Cr(NO_3)_3.9H_2O + 8NH_4OH \longrightarrow Co(OH)_2.Cr_2(OH)_6 + 15H_2O + 8NH_4NO_3 \quad (2\text{-}6)$$

$$Co(OH)_2.Cr_2(OH)_6 \longrightarrow CoO.Cr_2O_3 + 4H_2O \qquad\qquad (2\text{-}7)$$
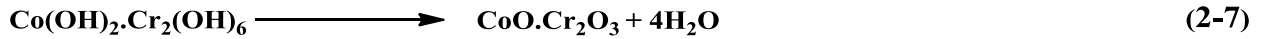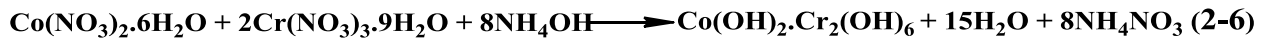
2.6   Preparation of (Spinel CoCr₂O₄ / ZrO₂) Nano Composites

The preceding procedures were carried out with the 1:2 and 1:3 ratios from spinel $CoCr_2O_4$: ZrO_2, respectively. The first step is to create nanocomposites was done when spinel $CoCr_2O_4$ suspension in ethanol and ZrO_2 suspension in ethanol were put in an ultrasonic bath at 60 kHz and 75 °C for 1 h. As a result, it is acceptable to provide sufficient energy to combine ZrO_2 and spinel $CoCr_2O_4$ into the crystal lattice. The second step is performed by adding a spinel $CoCr_2O_4$ suspension solution step by step to ZrO_2 suspension solution to incorporate it in two ratios of 1:2 and 1:3 using an ultrasonic bath for 2 hours at 75 °C. After that, the generated mixtures were stirred with heated at the same temperature for a further two hours using a magnetic stirrer until dried at 75 °C. A green powder from the spinel $CoCr_2O_4/ZrO_2$ nanocomposite has appeared, after that washed with ethanol and stored overnight in a desiccator using silica gel. The chemical equation for the synthesis of spinel $CoCr_2O_4/ZrO_2$ nanoparticles was suggested using equation (2-8).

 As in the preparation reaction in figure (2-7).

$$CoCr_2O_4 + ZrO_2 \xrightarrow{\text{(ultrasonic waves)}} CoCr_2O_4\text{-}ZrO_2 \qquad\qquad (2\text{-}8)$$

Ratio
50 % and 75%

CoCr$_2$O$_4$ sol.

2.5 g CoCr$_2$O$_4$ and 25 mL(C$_2$H$_5$OH)

2.5 g CoCr$_2$O$_4$ and 25 mL(C$_2$H$_5$OH)

ZrO$_2$ sol.

5 g ZrO$_2$ and 50 mL (C$_2$H$_5$OH)

7.5 g ZrO$_2$ and 75 mL (C$_2$H$_5$OH)

Put in ultrasonic at 75 °C for 1 h

Put in ultrasonic at 75 °C for 1 h

CoCr$_2$O$_4$

ultrasonic

ZrO$_2$

Heated on hotplate at (75) °C .

Washing by (10–20) mL distilled water and ethanol

CoCr$_2$O$_4$/ZrO$_2$

Stored over night

Figure (2-7). The schematic diagram for steps of prepared CoCr$_2$O$_4$ /ZrO$_2$ composite

2.7 Characterization of Photo Catalysts

2.7.1 X-Ray Diffraction Spectroscopy (XRD)

The mean Crystal sizes (L) of all samples were calculated by Scherrer's equation (eq. 2-9) [131,132]. The equation depended on the Data from X-Ray

diffraction (XRD). XRD data were analyzed by Shimadzu, Lab X XRD 6000 instrument. This instrument is used Cu as a target source with wavelength 1.54060 Å, voltage 40.0 kV and current 30 mA, speed is equal to 12.0000 (deg/min) and angle (2θ) range between (20 – 80) deg.

$$L = \frac{k\,\lambda}{\beta\,\cos\theta} \qquad\qquad\qquad (2\text{-}9)$$

Here: k is the Scherer's constant which depending on the dimensionless shape (used 0.94 spherical and 0.9 semi spherical), λ is the wavelength (used 0.15406 nm for Cu kα), θ is a Bragg diffraction angle and β is (FWHM) the full half-maximum intensity width that measured in degrees, but must convert to radians by multiplied to ($\pi/180$).

2.7.2 Scan Electron Microscopy (SEM)

The scanning electron microscopy image was measured for all samples (commercial ZrO_2, spinel $CoCr_2O_4$, and composites 1 and 2) using SEM analysis (FESEM FEI Nova Nano SEM 450)., USA.

2.7.3 Energy Dispersive X-Rays (EDX)Analysis

 The EDX spectra for all samples were performed via using SEM instruments to validate the sample's components as a percentage of atoms in samples.

2.7.4 Bandgap Energy Measurements

 Direct bandgap energy (Eg) was calculated with Tauc equation (eq. 2-11) [133] in (eV) by using UV- Visible spectrophotometer. The absorbance coefficient (α) [134] was found in equation (2-10) which depended upon absorption (A), and thickness (t).

$$\alpha = (2.3026\,A)/t \qquad\qquad\qquad (2\text{-}10)$$

$$\alpha h\nu = k(h\nu - E_g)^m \qquad\qquad\qquad (2\text{-}11)$$

Here: α is the absorption coefficient of Photocatalysts, m is constant depending on the type of (Eg) and equal to ½ for a direct transition, h is Plank's constant, v is the frequency of the incident photon light and k is optical constant. After the preparation of photocatalysts such as a spinel $CoCr_2O_4$ and its composites with ZrO_2 should be applied to see if they are photocatalysts or no.

2.8   Photocatalytic Decolorization Reaction of Colored Material

The experiments were carried out in the photo-reactor unit using a high-pressure mercury lamp (400 Watt, 475nm), as a UV-A radiation source. First, without using the lamp for 15 minutes, the dark reaction was done. Periodically, UV-A light was used in irradiated the suspension solutions of colored Fe-complex solution with employed photocatalysts. Approximately 3 mL were removed by syringe at different periods and then double separated using a centrifuge at (15 min and 4000 rpm). The absorption was read at 475 nm for the filters formed. The apparent rate constant of this photoreaction (in equation 2-13) was calculated after the adsorption equilibrium, which can be expressed by the Langmuir-Hinshelwood model that modified for the pseudo-first-order kinetics[135] equation as equations (2-12 or 2-13):

$$\ln\left(\frac{C_o}{C_t}\right) = k_{app.}t \tag{2-12}$$

$$\text{or} \quad \ln\left(\frac{A_o}{A_t}\right) = k_{app.}t \tag{2-13}$$

Here: C_o and C_t are the initial concentration of the complex at the dark reaction (without radiation) and after irradiation, respectively

The percentage of photocatalytic decoloration (PDE) [135] of the complex solution was calculated by equation (2-14).

$$PDE = \frac{(A_o - A_t)}{A_o} \times 100 \tag{2-14}$$

Here: A_o and A_t are the initial absorbances of the complex at the dark reaction (without radiation) and after irradiation, respectively

2.9 Light Intensity Measurements

The light intensity for the UV-A light source which used in this work was determined using the chemical actinometric method [136]. An exact 100 mL of actinometric solution was exposed to UV-A light of photoreactor. The actinometric solution has been prepared by mixing from 40 mL of 0.15 M $Fe_2(SO_4)_3.H_2O$ with 50 mL of 0.45 M $K_2C_2O_4.H_2O$ and 10 mL of 0.05 M H_2SO_4 with the presence of atmospheric oxygen under irradiated UV-A lamp's light. The yellowish-green solution was produced; from the last solution, approximately 2 mL of irradiated solution with regular periods at (5, 10, and 15) min was taken and centrifuged at 4000 rpm with 10 min. 0.5 mL of filtered was added to 2.5 mL from 1% from $1,10 -$ phenonethroline as a reagent, that will produce reddish-orange complex as ferroxalate complex ($[Fe^{2+} (C_2O_4)^2]^{2-}$), as noted in equations from (2-15) to (2-18), which absorbed at 510 nm.

$$[Fe^{3+} (C_2O_4)_3]^{3-} + hv \longrightarrow [Fe^{2+} (C_2O_4)_2]^{2-} + C_2O_4^{\cdot -} \qquad (2\text{-}15)$$

$$[Fe^{3+} (C_2O_4)_3]^{3-} + hv \longrightarrow Fe^{2+} + 2(C_2O_4)_2^- + C_2O_4.^{\cdot -} \qquad (2\text{-}16)$$

$$[Fe^{3+} (C_2O_4)^3]^{3-} + C_2O_4.^{\cdot -} \longrightarrow [Fe^{2+} (C_2O_4)_2]^{2-} + C_2O_4.^{\cdot -} + 2CO_2 \qquad (2\text{-}17)$$

$$2[Fe^{3+} (C_2O_4)_3]^{3-} \longrightarrow 2[Fe^{2+} (C_2O_4)_2]^{2-} + C_2O_4^{\;2-} + 2CO_2 \qquad (2\text{-}18)$$
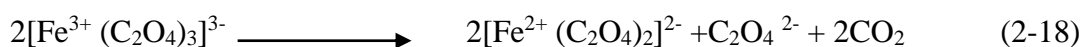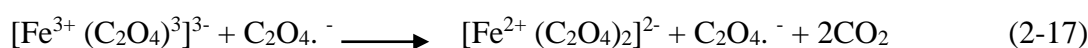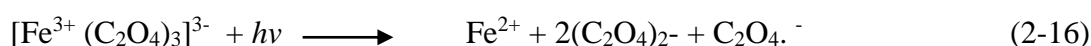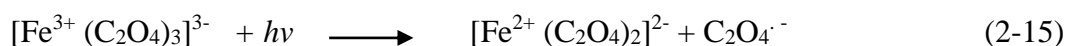
The following equations were measured the light intensity (I_o): [137]

$$\text{Moles of Fe}^{2+} = \frac{V_1 \times V_3 \times A_{(510\,nm)}}{V_2 \times l \times \varepsilon_{(510\,nm)} \times 10^3} \qquad (2\text{-}19)$$

$$I_o = \frac{\text{moles of } Fe^{+2}}{\Phi_\lambda \times t} \qquad (2\text{-}20)$$

$I_o = 1.9 \times 10^{-7}$ Ernestine s^{-1}

Here: ($V_1 = 100$ cm^3) is the total volume of irradiation chemical-actinometric solution, ($V_3 = 3$ cm^3) is the volume of irradiation solution that added to the

reagent 1, 10-phenonethroline solution, ($V_2 = 0.5$ cm^3) is the volume of filtered irradiation solution, the length of the optical path (1cm) is the quantity yield [132]; A_{510} is the average absorption of ferrioxalate solution after various internal irradiation times, which is mixed with 1,10-phenonethroline, molar absorption ($\varepsilon = 1.045$ x 10^4 L mol^{-1}cm^{-1}) and (t) the average irradiation time (10 min).

2.10 Activation Energy

The apparent activation energy (Ea) of photocatalytic decoloration of the complex solution has been found based on the Arrhenius equation. The apparent activation energy of the photo-decolorization reaction of the complex was determined from the graph's linear relationship of the Arrhenius equation [138] .

$$\ln k_{app} = \frac{-E_a}{RT} + \ln A \qquad\qquad (2\text{-}21)$$

Here. k_{app} is an apparent constant rate, T is the reaction temperature, R is a constant gas (8.314 J mol^{-1} K^{-1}) and A is a frequency constant.

2.11 Thermodynamic Parameters:

The thermodynamic parameters are deemed as vital parameters to determine the type and direction of this photo-reaction. It was found depending on Eyring equation [139], (equation 2-22) and Gibbs equation (equation 2-23), which used to calculate the enthalpy change ($\Delta H^{\#}$), the entropy change ($\Delta S^{\#}$) values and the free energy($\Delta G^{\#}$) respectively [140].

$$\ln\left(\frac{K_{app}}{T}\right) = \frac{-\Delta H^{\#}}{RT} + \left(\ln\left(\frac{K_B}{h}\right) + \frac{\Delta S^{\#}}{R}\right) \qquad\qquad (2\text{-}22)$$

$$\Delta G^{\#} = \Delta H^{\#}\text{-}T\Delta S^{\#} \qquad\qquad (2\text{-}23)$$

Here: k $_{app}$ is an apparent constant rate of photoreaction, R is a constant gas (8.314 J mol^{-1} K^{-1}), k_B is the constant of Boltzmann (1.381 x 10^{-23} J K^{-1}) [141], T is the reaction temperature and h is the constant of Plank (6.63 x 10 $^{-34}$ J s

CHAPTER THREE
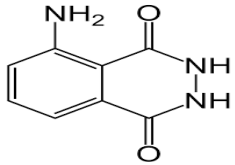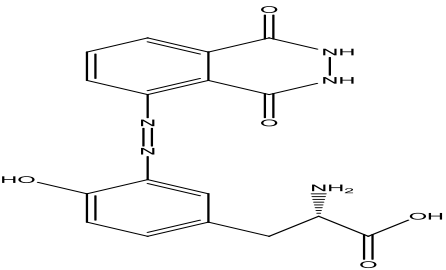
Results & Discussion
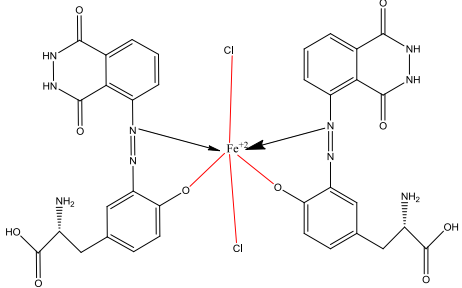
3.1 Identification of Luminol and (Luminol -Tyrosine) and of Fe(II)-(Luminol -Tyrosine) Complex.

3.1.1 Physical Properties of the Ligand Luminol and (Luminol - Tyrosine) and of Fe(II)-(Luminol -Tyrosine) Complex.

The results in Table (3-1) indicate that complexes' color and melting point differ greatly from those of ligands. The color of the ligand alters from light yellow to brown, and then it combines with iron (II) to form a complex, the color changed to chocolate. Furthermore, the melting points of the ligand and its complex were measured, they are charred. The ligands and complex are owing high stability toward the air and light. The physical characteristics of the ligand Luminol, (Luminol -Tyrosine) ligand, and the Fe (II) complex as FeL_2Cl_2 are listed in Table (3-1).

Table (3-1). The physical characteristics of the ligand Luminol and (Luminol - Tyrosine) ligand and the Fe (II) complex as FeL_2Cl_2

Compound	Color	Melting point (°C)	Structure
Luminol	Pale yellow crystal	319	
ligand Luminol -Tyrosine	brown	Roasted	

Fe(II)-(Luminol - Tyrosine) complex	chocolate	Roasted	

3.1.2 Stability of Complex

Based on the results in Table (3-2) and figure (3-1), the stability constant and the structure of the complex were estimated using the mole ratio method. The ligand: Fe^{2+} ratios was performed using the different weight for each (Luminol - Tyrosine)ligand and Fe(II) chloride salt, and combined complex using microwave instrument at 326 Watt. This different ratio was dissolved in a fixed volume of DMSO (5 mL) and found their absorbances at a maximum wavelength of 475 nm.

Table (3-2): Mole ratio method for ligand: Fe(II) with concentration 1×10^{-2} M and with a certain volume.

(L g/Fe^{2+} g)	Abs.
0.018 g/0.016 g	0.911
0.036 g/0.016 g	0.881
0.055 g/0.016 g	0.810
0.073 g/0.016 g	0.804
0.091 g/0.016 g	0.575
0.011 g/0.016 g	0.121
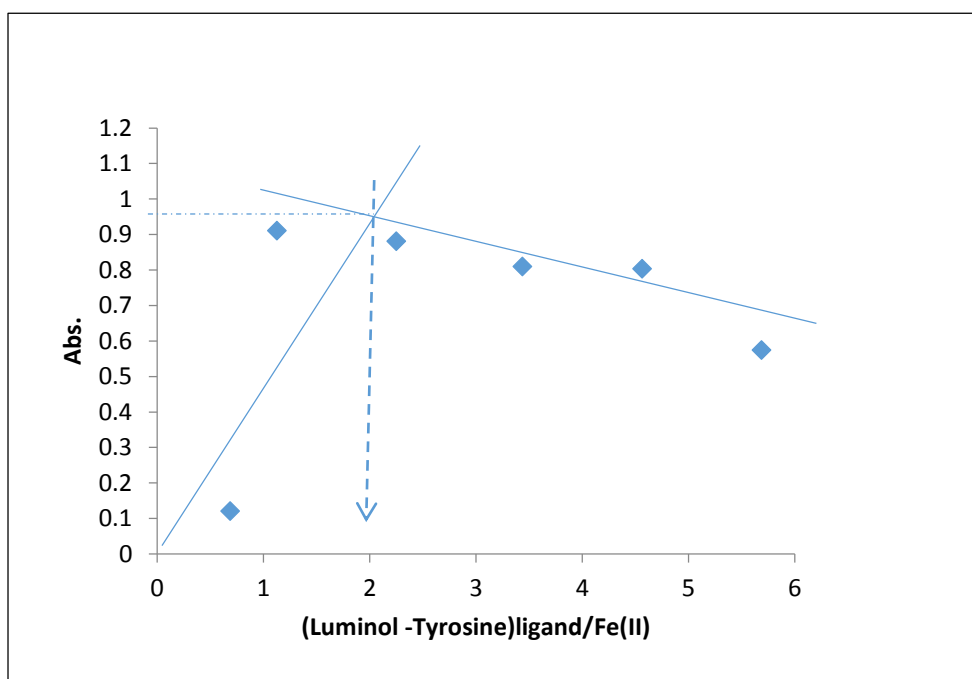
Figure (3-1). Mole ratio method for (Luminol -Tyrosine)ligand: Fe(II).

The Fe:L ratio is found to be 1:2, and the complex is having an octahedral hybridization. The interaction between Fe(II) and a prepared ligand to form Fe-complex as FeL_2Cl_2 is explained by equation (3-1).

(3-1)
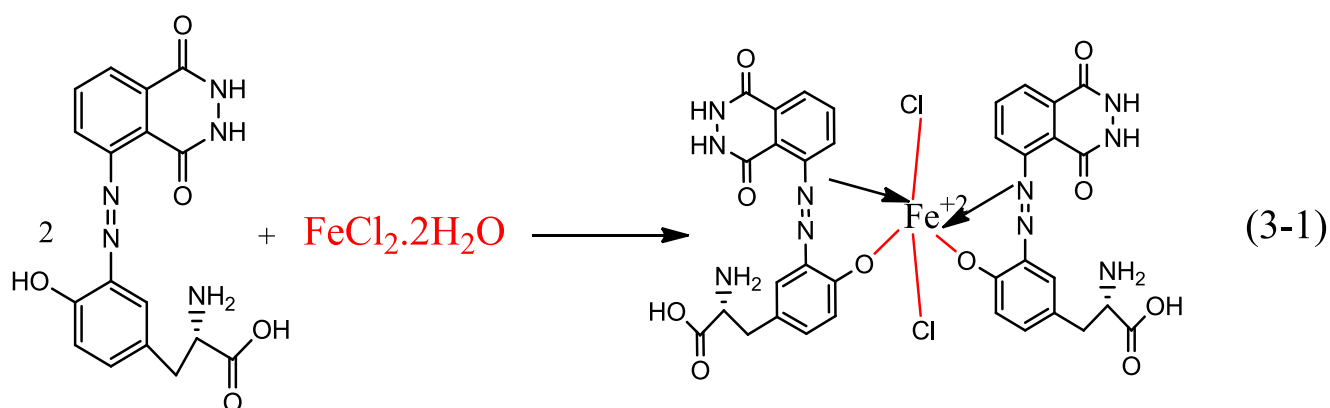
The data of the mole ratio graph is illustrated in process of calculating the instability and stability constant [142, 143]. of Complex that is based on the

equations (3-2) to (3-4). This is ensured by high Complex stability constant of $3.105 \times 10^3 \ M^{-1}$.

$$FeL_2 \rightarrow Fe^{2+} + 2\,L \tag{3-2}$$
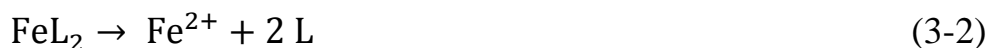
$$k_{instability} = \frac{[Fe^{2+}][L]^2}{[FeL_2]} = \frac{\left[1 - \frac{A}{A_{max}}\right]^3}{\left[\frac{A}{A_{max}}\right]} \times C_{Fe^{2+}} \tag{3-3}$$

$$= \frac{\left[1 - \frac{0.85}{0.911}\right]^3}{\left[\frac{0.85}{0.911}\right]} \times 1 \times 10^{-2} = 3.22 \times 10^{-6} M$$

$$k_{stability} = \frac{1}{k_{instability}} \tag{3-4}$$

$$= \frac{1}{3.22 \times 10^{-6}} = 3.105 \times 10^3 \ M^{-1}$$

3.1.3 UV.Vis Spectral Analysis of the Luminol Reagent, Luminol -Tyrosine Ligand, and Fe(ll)- Luminol -Tyrosine Complex.

In Figure (3-2) A, two absorption peaks appeared in the UV-Vis spectrum of the luminol reagent at (293 nm and 385 nm) for the π–π* and n–π*electronic transitions due to the C=C and C=O bond, respectively. In the UV-Vis spectrum of ligand in Figure (3-2) B, a new absorption peak appeared at (448 nm) for the n–π* electronic transitions due to the N=N bond. In addition, two absorption peaks appear at (293 nm, 385 nm) for the π–π* and n–π* electronic transitions due to the C=C and C=O bond, respectively. As for the Figure (3-2) C spectrum, when the Fe(II) complex is formed, the UV-Vis spectrum of the Fe(II) complex occurs a new absorption peak at 475 nm, for the d–d electronic transitions which are attributed to the link of the ligand with the element. In addition to the appearance of three absorption peaks at (307, 395, and 460) nm, due to the C=C, C=O, and N=N bonds, respectively.

Indeed, the red shift of the absorption peaks (for n–π* electronic transitions) is clearly obtained from 448 nm to 460 nm after formed iron complex. This case leads to produce the high stable bond between Fe and ligand [144].

A

B

Figure (3-2). UV-Vis spectra for A) reagent, B) ligand, and C) complex FeL₂Cl₂
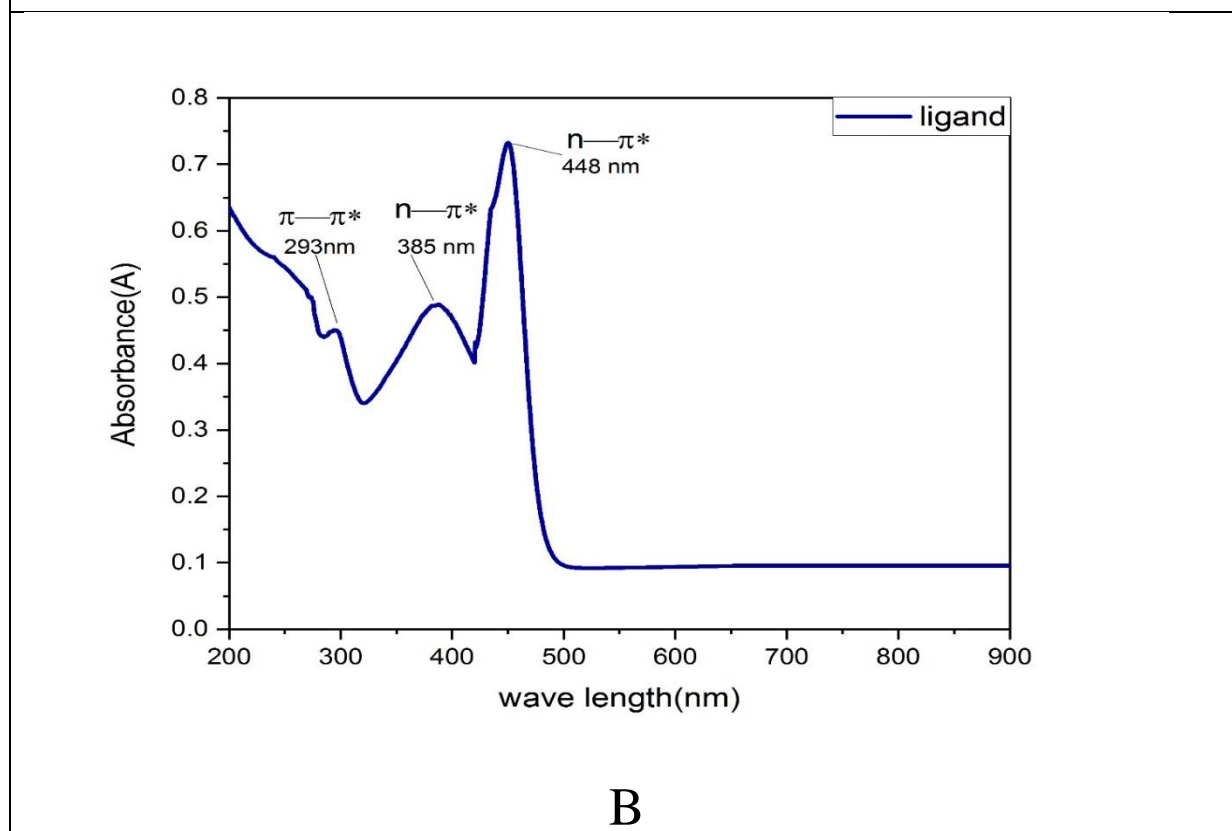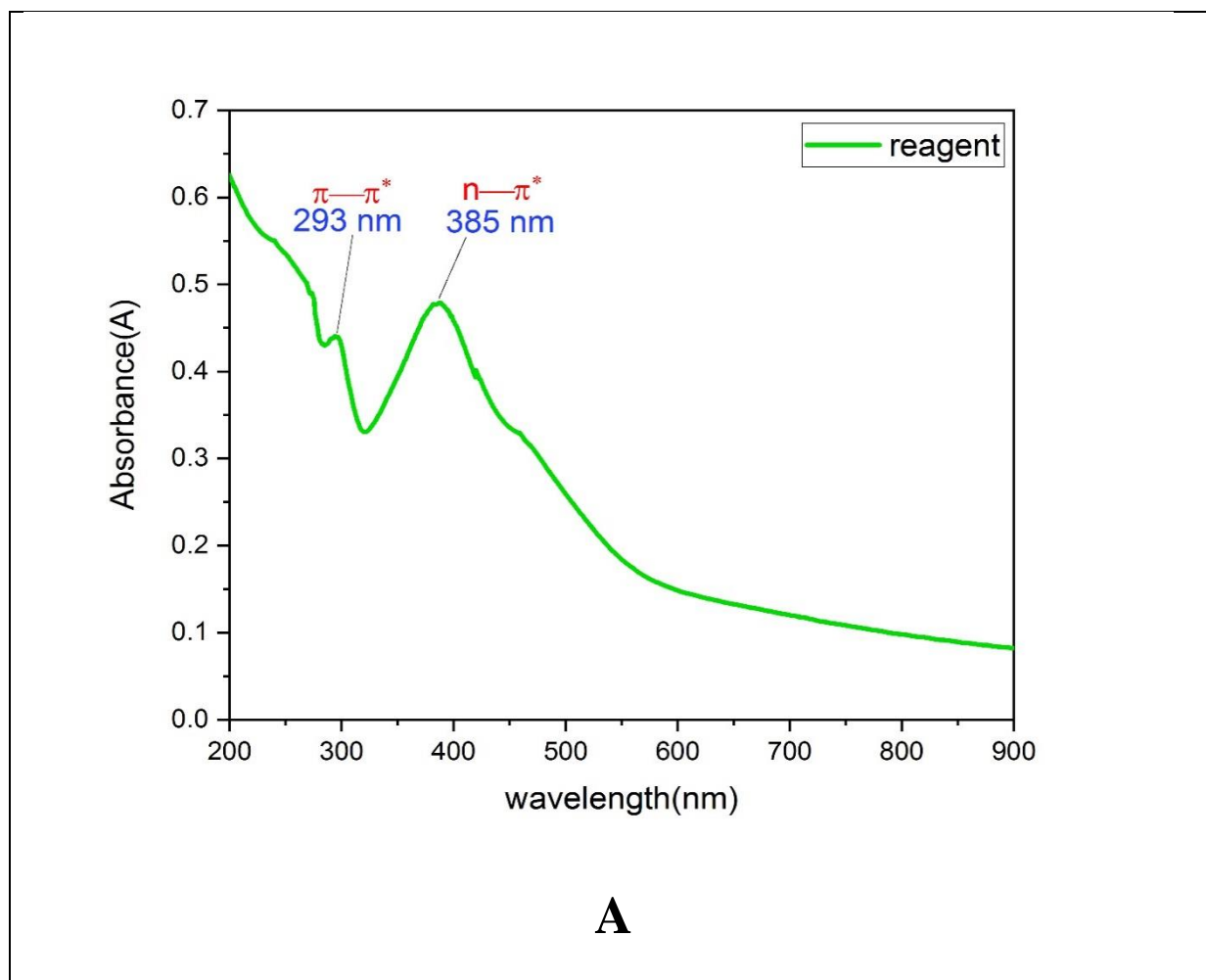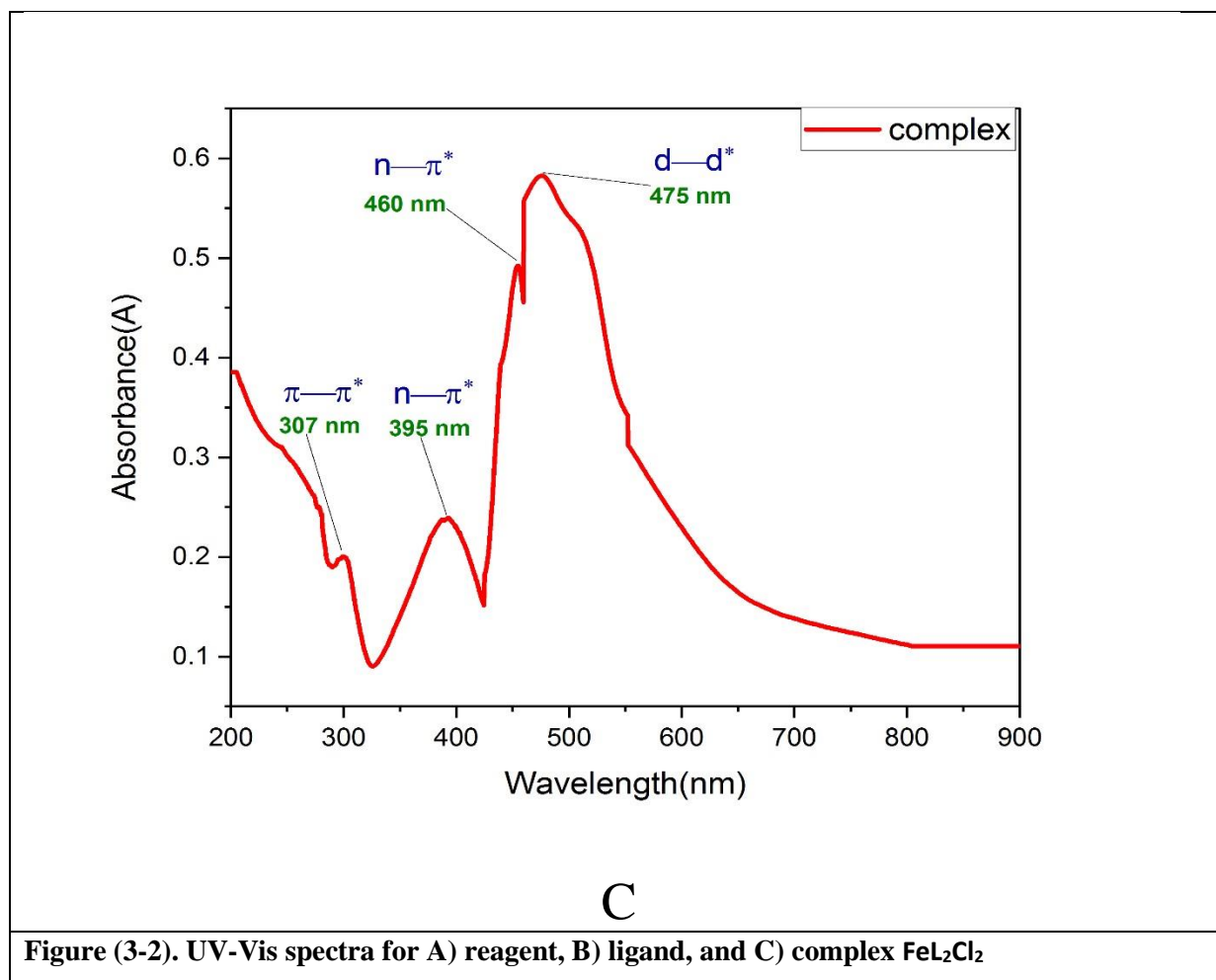
3.1.4 FTIR and ^{1}H NMR Spectral Analysis of the Luminol Reagent, Luminol -Tyrosine Ligand, and Fe(ll)- Luminol - Tyrosine Complex.

Based on FTIR spectra in Figures 3-3 to 3-5, the Luminol reagent's FTIR spectrum (Figure 3-3) displayed an absorption peak at (3445 and 3418) cm^{-1}, which was attributed to the stretching vibrations of the NH_2 bonds. Additionally, the spectra revealed absorption bands at 1653 cm^{-1} due to the stretching vibration of the C=O bonds, which corresponds to the C=O connected in the ring. The N–H bond, C=C bond, and aromatic stretching bond between C–H are also responsible for absorption peaks at 1490 cm^{-1}, 1601 cm^{-1}, and 3154 cm^{-1}, respectively.

The FTIR spectra of the Luminol -Tyrosine ligand in Figure 3-4, revealed a broad absorption peak in the region (2800-3600) cm^{-1} due to the stretching vibrations of O–H bonds in a carboxylic acid. Two absorption bands at 1587 cm^{-1} were seen, which are attributable to the stretching vibration of the C=O bonds that are similar to the C=O in carboxylic acids. The carboxylic C–O bond stretching is responsible for the absorption peak at 1246 cm^{-1} [145,146]. At 1425 cm^{-1}, an absorption band was observed, which was attributed to the N=N band. The Fe (ll)-Luminol-Tyrosine combination has an FTIR spectrum. The new peaks at (233 cm^{-1}) and (574 cm^{-1}) have similar appearances in the spectra of Fe-complexes that attitudes to building Fe-N and Fe-O bonds, respectively. The coordination between Fe and this ligand via the N-Ligand side is exceedingly close[147,148], as shown in Figure (3-5).

C:\Users\Lenovo\Documents\Bruker\OPUS_7.5.18\DATA\MEAS\Sample description.2086   Sample description   Instrument type and / or a 24/11/2020
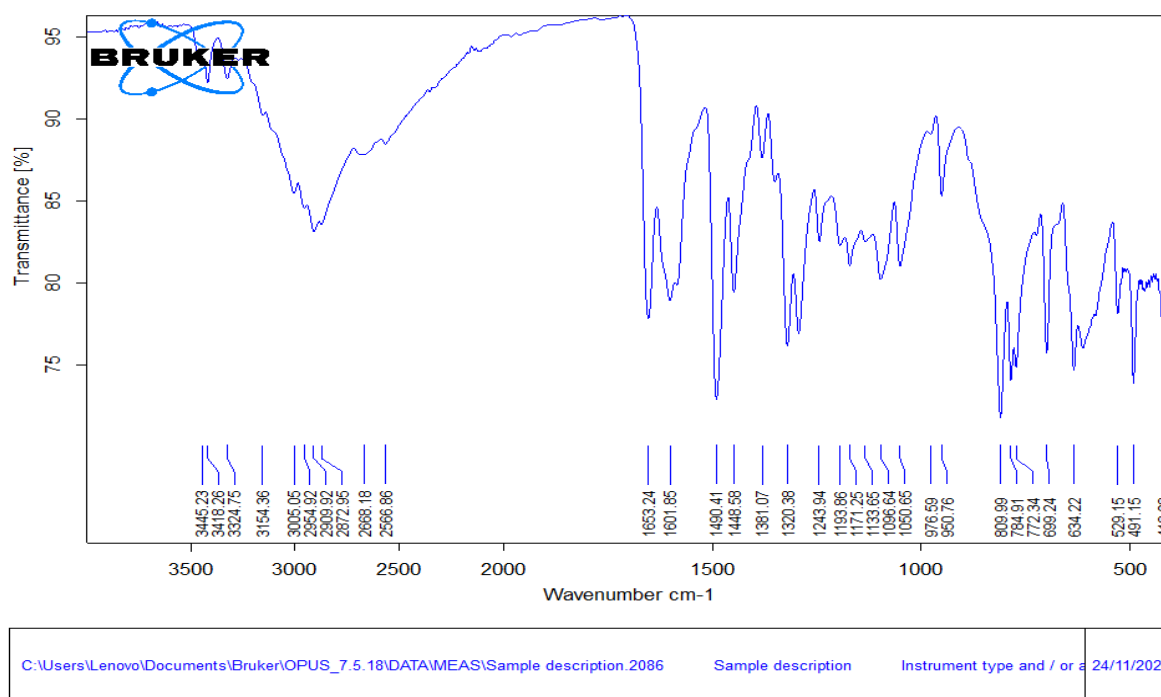
Page 1/1

Figure (3-3). FTIR spectrum of Luminol reagent.
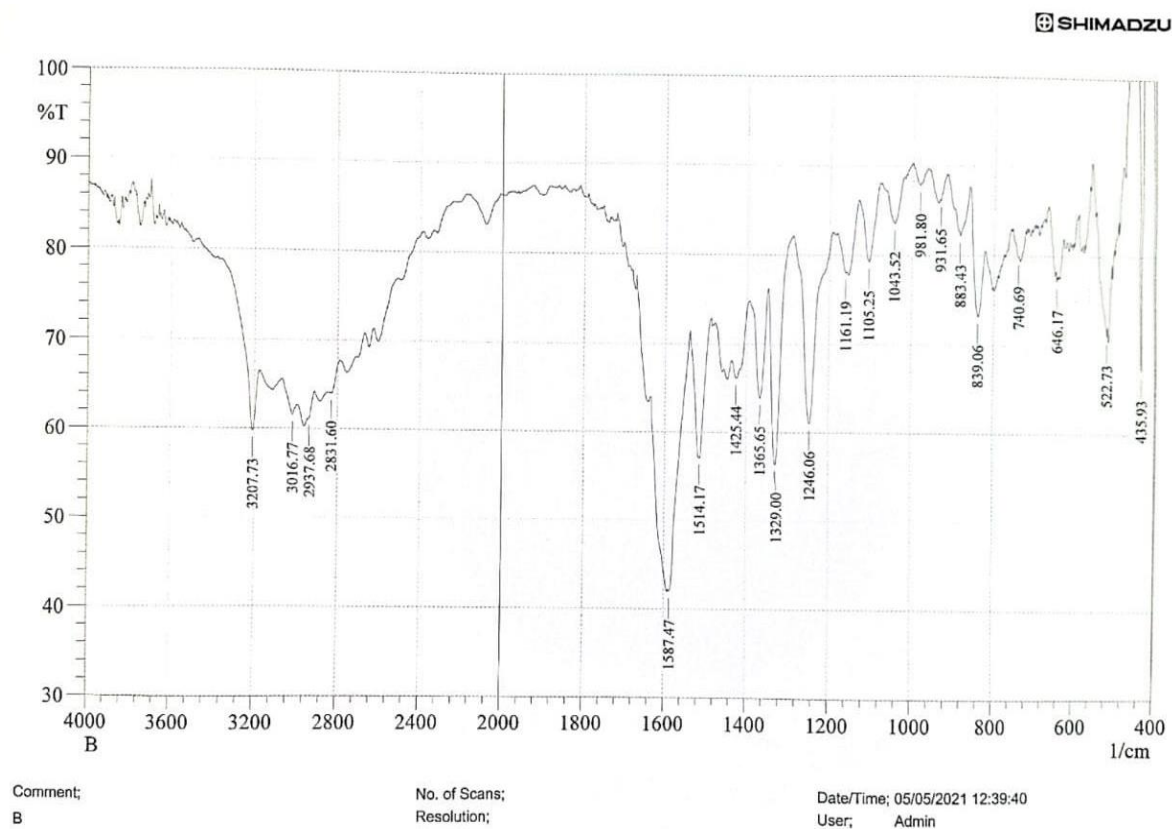
Figure (3-4). FTIR spectrum of the Luminol -Tyrosine ligand.
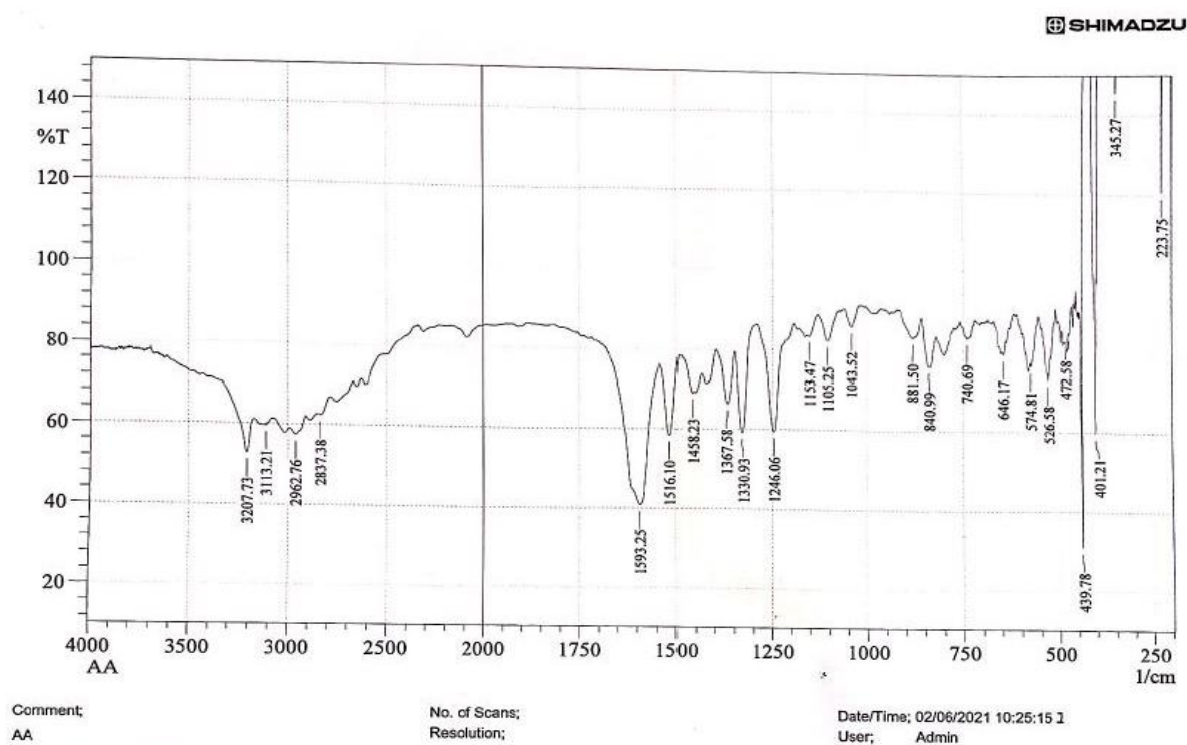
Figure (3-5). FTIR spectrum of the Fe(ll)-Luminol -Tyrosine complex.

The proton nuclear magnetic resonance (^{1}HNMR) spectra for all stages of compound synthesis in Figures 3-6 to 3-8 were analyzed. This analysis has been used DMSO-d6 dimethyl oxide as a solvent and TMS as a standard reference. Figure 3-6 displays the Luminol's ^{1}HNMR spectrum, which reveals a doublet band with a chemical shift $\delta = 6.88$ ppm. It all comes down to groups being in positions 3 and 5. While another doublet package with a chemical shift of $\delta=$ 6.95 ppm has still appeared in positions 1 and 2. As for the triplet package at chemical shift $\delta=7.45$ ppm, it goes back to having groups in positions 4 and 6.
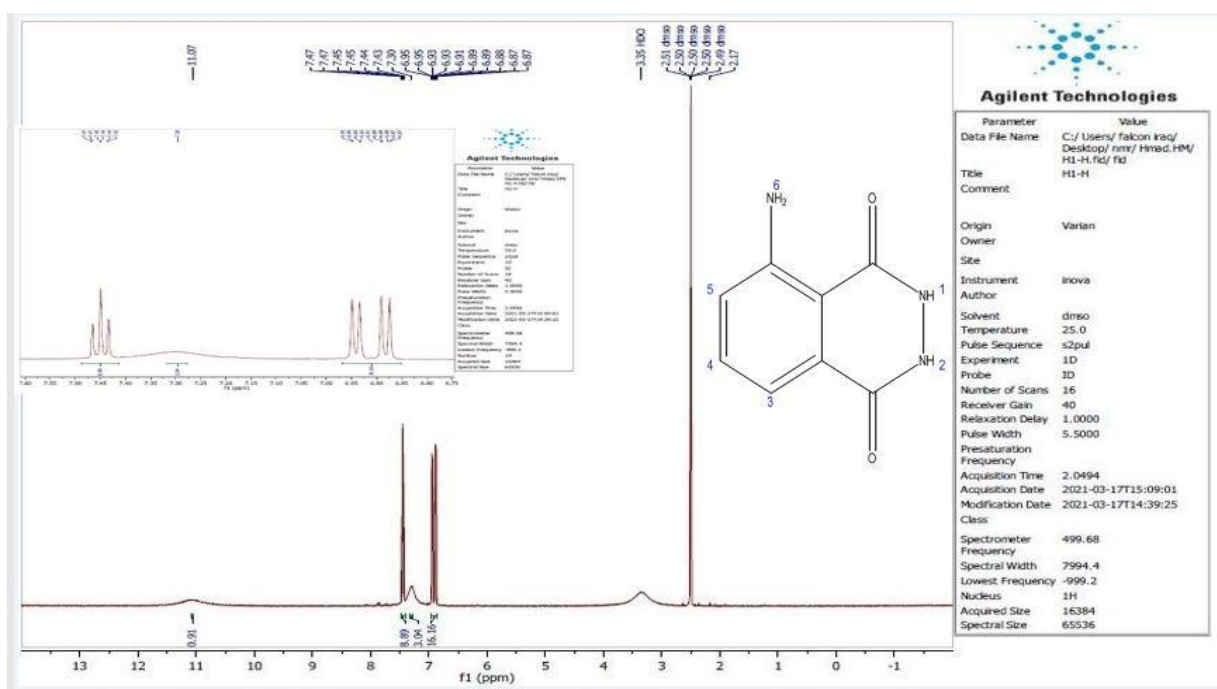
Figure (3-6). ^{1}H NMR spectrum of Luminol reagent.

Figure (3-7) explains a doublet band at chemical shifts ($\delta=8.30$ ppm, $\delta=3.40$ ppm, $\delta=7.90$ ppm, $\delta=7.0$ ppm, and $\delta=6.86$ppm). It all comes back to groups being in positions (1,2), (3,5), (6,12), 7, and 8. As for the triplet package at chemical shifts ($\delta=3.6$ ppm, $\delta=7.4$ ppm, and $\delta=8.0$ ppm), it goes back to having groups in positions 4,10, and 11.Single package at chemical shift $\delta=4.1$ in position 9. The disappearance of the (OH) group beam is an indication of its participation incoordination due to the loss of its proton and the formation of the Fe complex, where there was a change in the intensity and location of the beams

belonging to the complex spectrum compared to the spectrum of the ligand, as in Figure (3-8)[149,150].
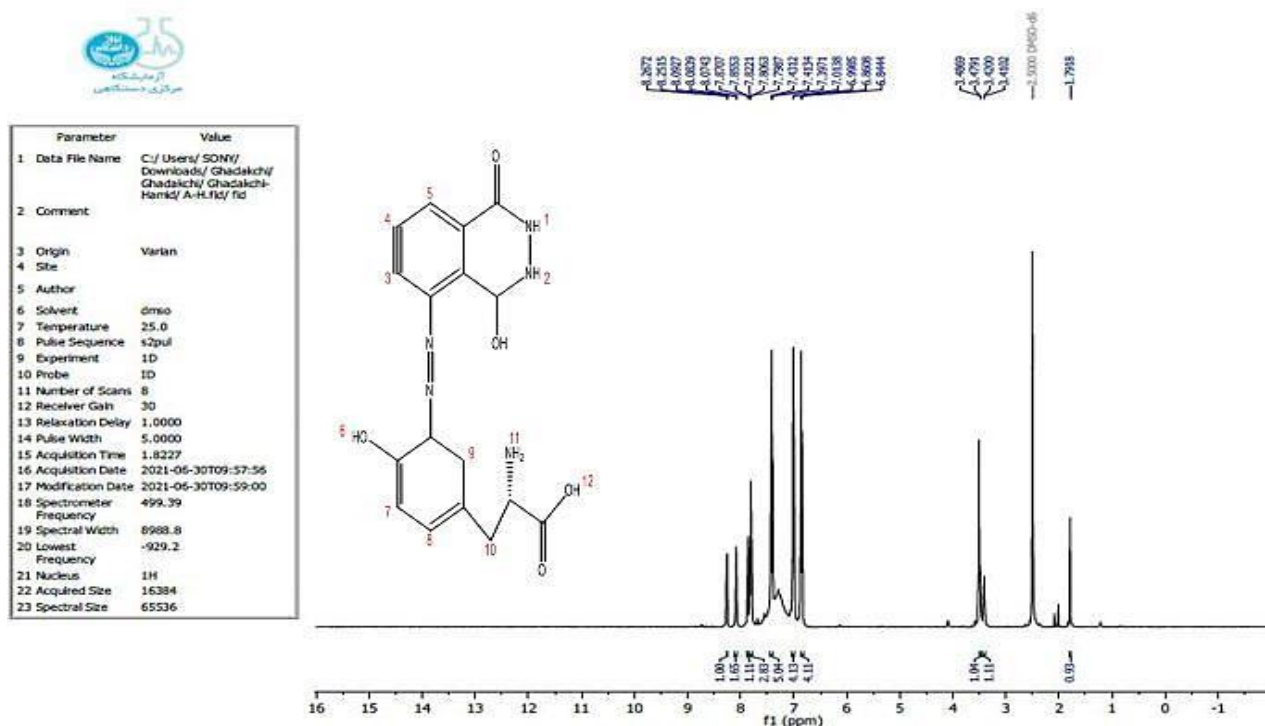
Figure (3-7) ^{1}H NMR spectrum of Luminol -Tyrosine ligand
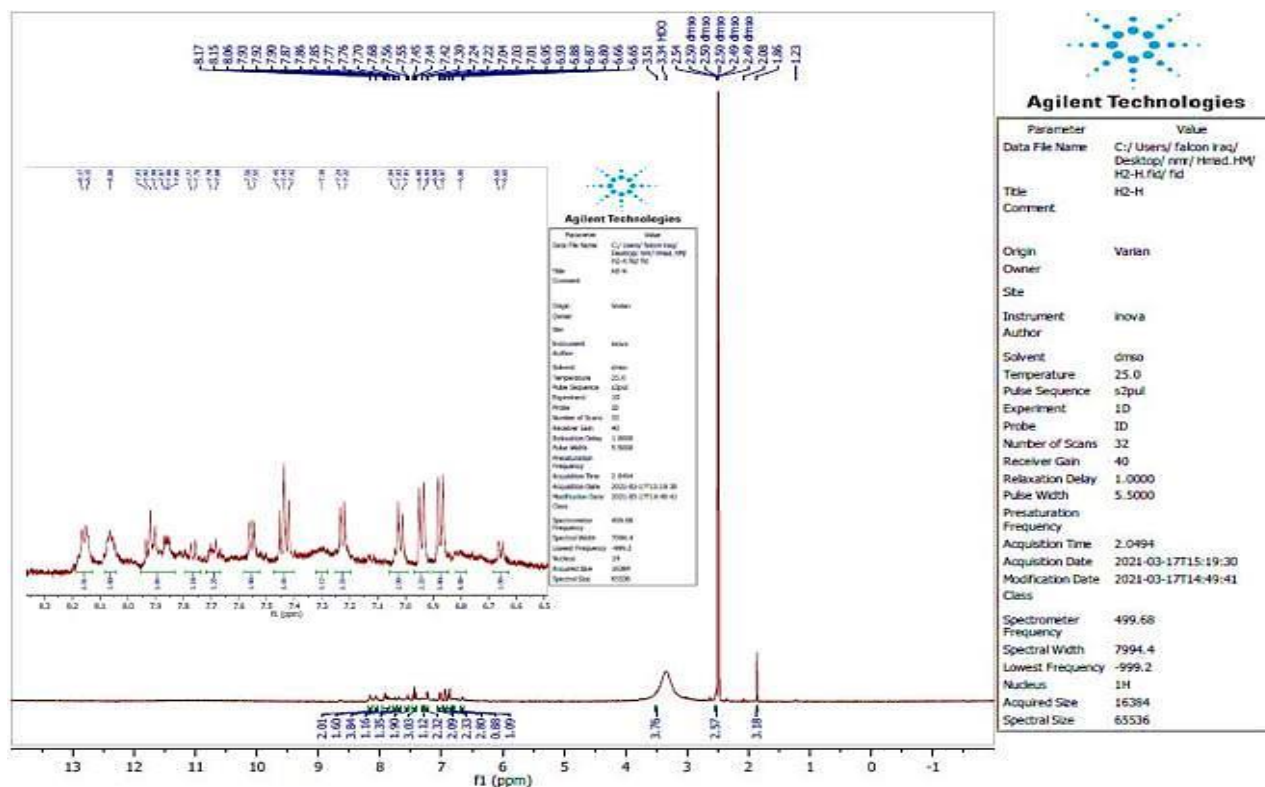
Figure (3-8). ^{1}H NMR spectrum of Fe(ll)-Luminol -Tyrosine complex

3.1.5 Magnetic Susceptibility

According to the stereotypes of complexes, the complex will have paramagnetic properties if the central atom includes one or more single electrons. The absence of single electrons in the core atom will result in the formation of diamagnetic characteristics in the complex under investigation, As the center atom has one or more electrons, the complex will exhibit paramagnetic characteristics [151,152]. The magnetic sensitivity of the prepared metal complexes was determined at 298 K. Pascal's constants were also used to adjust the magnetic characteristics of atoms in molecules, inorganic radicals, and metal ions. The following formulae were used to obtain the values (3-5) to (3-9) of the magnetic moment (μeff):

$$\mu_{eff} = 2.828 \sqrt{X_A \, T} \ \text{B.M} \qquad\qquad (3\text{-}5)$$

$$X_A = X_m - D \qquad\qquad (3\text{-}6)$$

$$X_m = X_g \times \text{M.wt} \qquad\qquad (3\text{-}7)$$

$$X_g = CL/10^9 \ m \ x \ (R\text{-}R_O) \qquad\qquad (3\text{-}8)$$

$$\mu_{eff} = \sqrt{n(n+2)} \qquad\qquad (3\text{-}9)$$

Where μ_{eff}, denotes the effective magnetic moment, M.wt is gram molecular weight, B.M is magnetic moment unit (Bohr magneton), C is 1.53, L is 1 cm, R is tube sensitivity with substance, R_O is empty tube sensitivity and m is the weight of the Sample = weight of the tube with the material - the weight of the tube when it is empty.

Fe(II)-Complex

Theoretical accounts

$_{26}$Fe $[Ar]_{18}$ $4s^2$ $3d^6$

$_{26}$Fe^{+2} $[Ar]_{18}$ $4s^0$ $3d^6$

3d⁶   **4s⁰**   **4p⁰**   **4d⁰**

| ↑↓ | ↑ | ↑ | ↑ | ↑ |

L   L   L   L   L   L
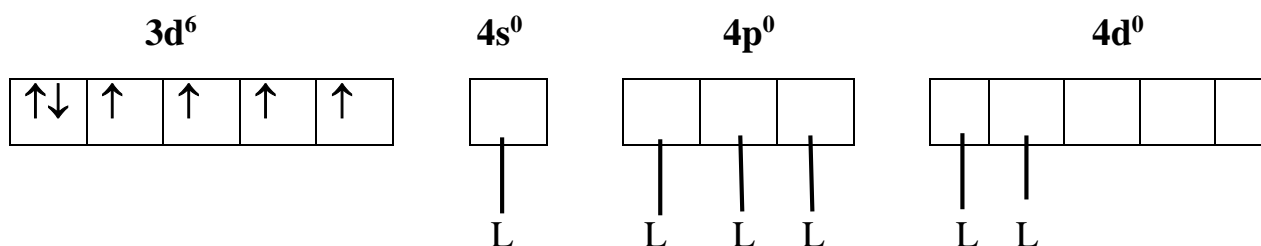
$$\mu_{eff} = \sqrt{n(n+2)}$$

$$\mu_{eff} = \sqrt{4(4+2)} \quad = 4.9 \text{ B.M}$$

practical calculations

Fe(II)-Complex

$$Xg = CL/10^9 m \times (R-R_o)$$

$$Xg = 1.53 \times 1 cm/10^9 (2.079-2.0636) \times (120\text{-zero})$$

$$Xg = 1.1922 \times 10^{-5}$$

$$Xm = Xg \times Mwt = 1.1922 \times 10^{-5} \times 863.40 = 1029.35 \times 10^{-5}$$

$$XA = Xm - D$$

$D =$ The sum of the atoms of each element x Pascal modulus x 10^{-6}

$$D = -62.2 \times 10^{-5}$$

$$XA = Xm - D = 1029.35 \times 10^{-5} - (-62.2 \times 10^{-5}) = 10.9155 \times 10^{-3}$$

$$\mu_{eff} = 2.828\sqrt{XA\ T}\ \text{B.M} = 2.828\sqrt{10.9155 \times 10^{-3} \times 298k}$$

$$\mu_{eff} = 5 \text{ BM}$$

Based on the top calculations, it concluded that the theoretical value of the magnetic susceptibility of the complex exactly matches the calculated value. Therefore, the complex is of an octahedral type with paramagnetic properties.

3.1.6 Elemental Micro Analysis (C.H.N.)

The reagent, ligand, and complex were diagnosed by accurate quantitative analysis of the elements (C.H.N), by matching theoretical and practical calculations of carbon, hydrogen, nitrogen, and the metal ion in those compounds.

The results of these analyses were recorded in Table (3-3). When comparing the practically obtained values with the theoretically calculated values, a great convergence was observed between them. This confirms the correctness of the added ratios of (metal: ligand), which supports the validity of the proposed formula for the complex.

Table (3-3) results of the precise elemental analysis (C.H.N) for each of the reagent, ligand, and complex.

Compounds	Molecular formula (molecular weight)	(theoretical) practical %			
		C	H	N	M
Reagent	$C_8H_7N_3O_2$ (177.16 g/mol)	(54.18) 54.24	(3.95) 3.98	(23.70) 23.73	-
Ligand	$C_{17}H_{15}N_5O_5$ (369.33 g/mol)	(55.23) 55.28	(4.06) 4.09	(18.95) 18.98	-
complex	$C_{34}H_{28}Cl_2FeN_{10}O_{10}$ (863.40 g/mol)	(47.45) 47.30	(3.24) 3.27	(16.21) 16.22	(6.46) 6.47

3.2 Characterizations of Photocatalysts

In this project, the characterizations of examined photocatalysts were investigated using XRD, SEM, EDX, and UV-Visible analyses to identify the band gaps.

3.2.1 X-ray Diffraction Patterns (XRD):

In Figure (3-9), XRD analysis was utilized to detect the structure and phase of spinel $CoCr_2O_4$ powder and a produced spinel $CoCr_2O_4$-ZrO_2 nanocomposite. The $CoCr_2O_4$'s key diffraction peaks are located at 30.3779^o, 35.8022^o, 43.3839^o, 57.5052^o, and 63.1014^o with miller indexes (220), (311), (400), (511), and (440) planes, respectively (JCPDS Card No. 00-022-1084) as shown in black color line, and are in strong agreement with findings in references [153,154]. On the other hand, monoclinic- ZrO_2 peaks in the red line exist at diffraction angles (111), (200), (220), and (311) with two locations of $30.2973°$, $35.0778°$, $50.4580°$, and $59.9693°$, respectively(JCDS card No.00-049-1642) [154,155]. The XRD analysis for the prepared composites confirms these findings match with the standard diffraction data for $CoCr_2O_4$ and m-ZrO_2. The essential peaks of ZrO_2 shift toward high diffraction angle after incorporating the crystal lattice, which indicates the formation of a metallic connection between Zr and Co in the spinel structure because both have a coordination number of six [156]. This case is an attitude to Co^{2+} in spinel has less ionic radii compared with Zr^{4+} and equal to 0.709 Å and 0.747 Å respectivelty[157,158]. Whereas the green line and blue line are given, the position of diffraction peaks for composites 1:2 and 1:3, which appeared the (111) peaks for ZrO_2 shifted toward large 2 thata after incorporated ZrO_2 with spinel, that due to link Zr with Co and Cr via metal bonds. On the other hand, the mean crystal sizes (L) for all samples were found using Scherer's equations [159-164], and found to be 15.5823 nm, 8.1785 nm, 9.6355 nm, and 9.0929 nm for the spinel $CoCr_2O_4$, ZrO_2, and the 1:2, and 1: 3 ratios as spinel $CoCr_2O_4$/ZrO_2 composites, respectively. Moreover, the elevated ZrO_2 with fixing the spinel $CoCr_2O_4$ amount, which leads to reducing the mean crystal sizes and enhancing the surface and optical characteristics.
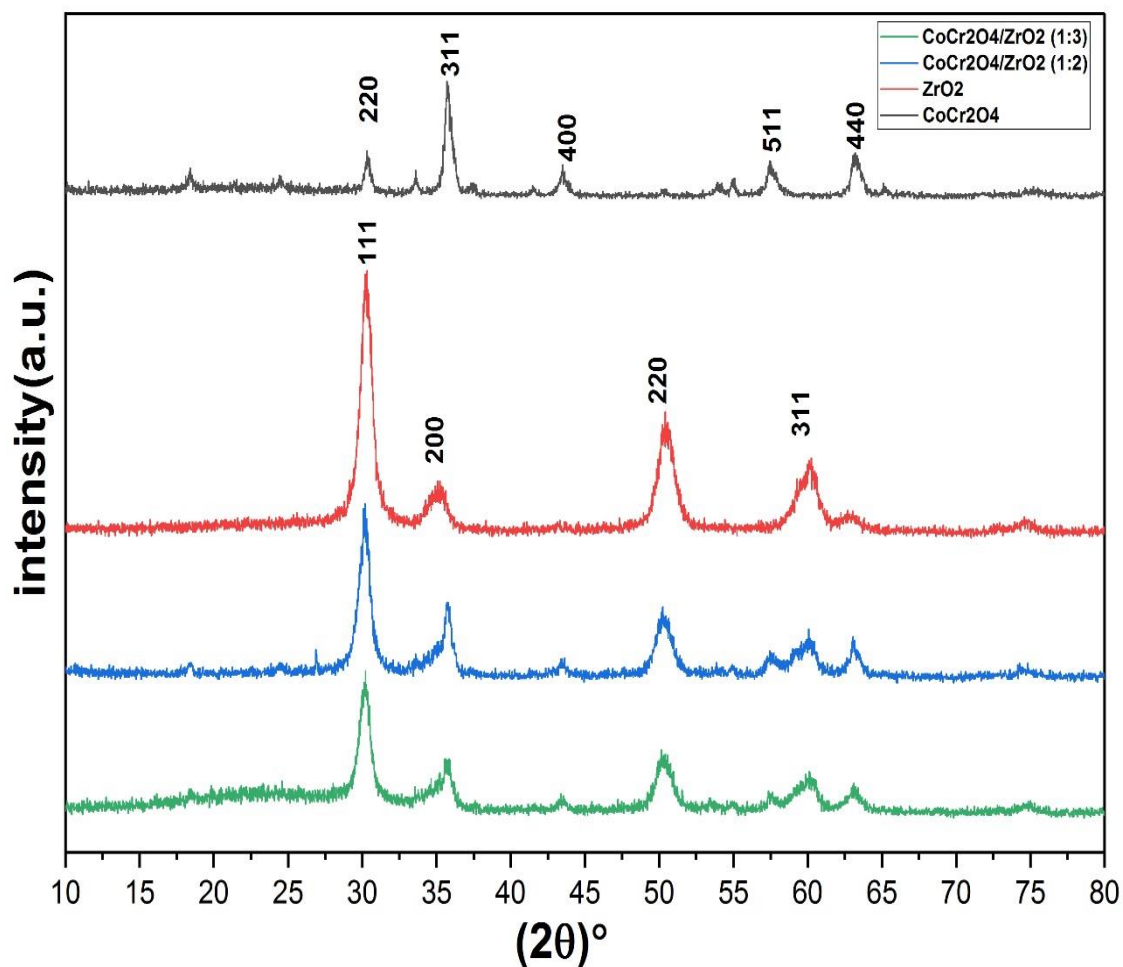
Figure (3-9). XRD patterns of spinelCoCr$_2$O$_4$, ZrO$_2$, CoCr$_2$O$_4$- ZrO$_2$ (1:2) nanocomposite and CoCr$_2$O$_4$-ZrO$_2$ (1:3) nanocomposite.

3.2.2 Scan Electron Microscopy (SEM)

The surface morphology of the samples was discovered using the SEM spactra of spinel CoCr$_2$O$_4$, ZrO$_2$, and their nanocomposites surfaces in Figure (3-10). The SEM images demonstrate that ZrO$_2$ is having a spherical micron-scale structure with particle sizes ranged (20.03 – 27.10) micrometr, that attitude to the high ability to agglomerate with fine powder. The synthesized spinel CoCr$_2$O$_4$ is shaped like spherical nanocrystals [165] with particle sizes ranged (30.10 – 34.98)nm. However, the spinel CoCr$_2$O$_4$-ZrO$_2$ composites un both ratios 1:2 and 1:3 appear a quasi-spherical shape with particles ranged (17.89 – 22.25)nm and (28.43 – 52.62) nm, respectively.
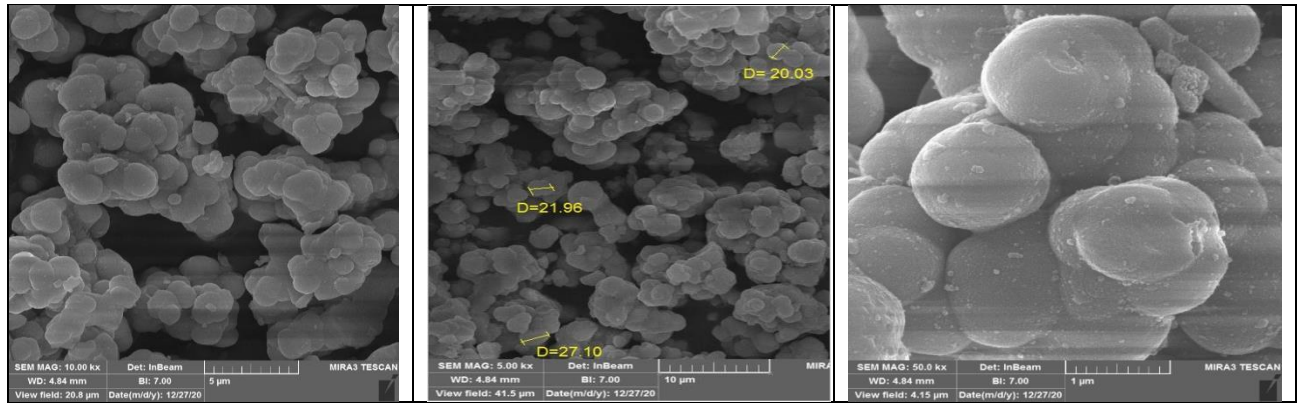
A
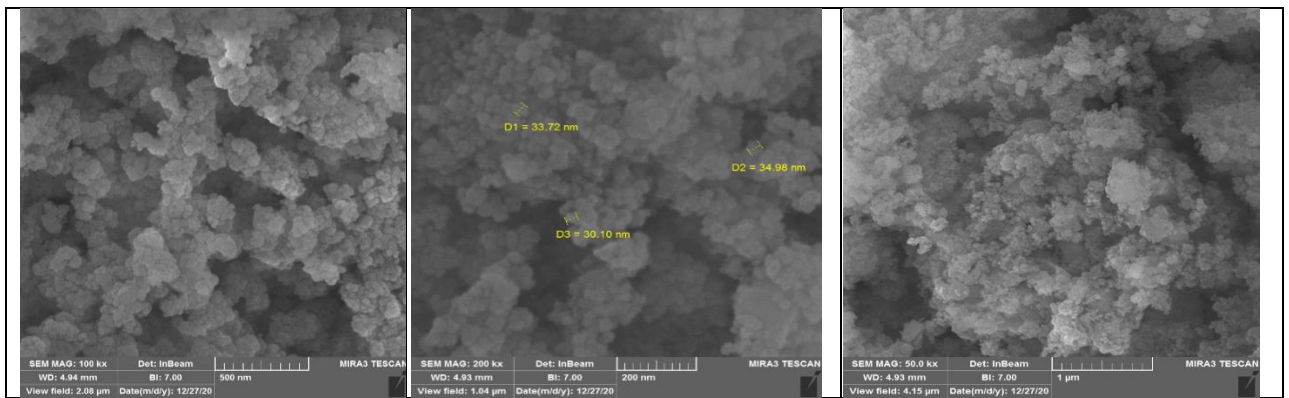
B
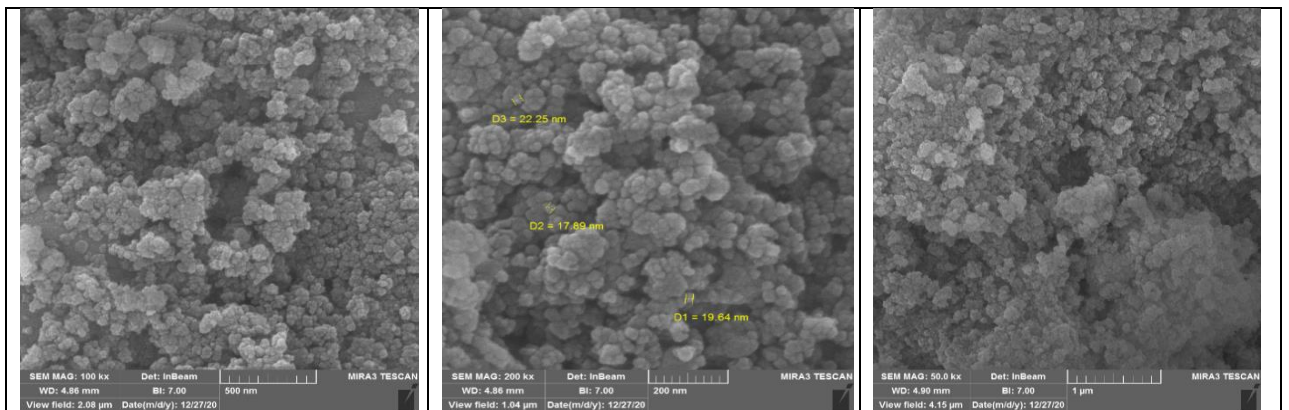
C
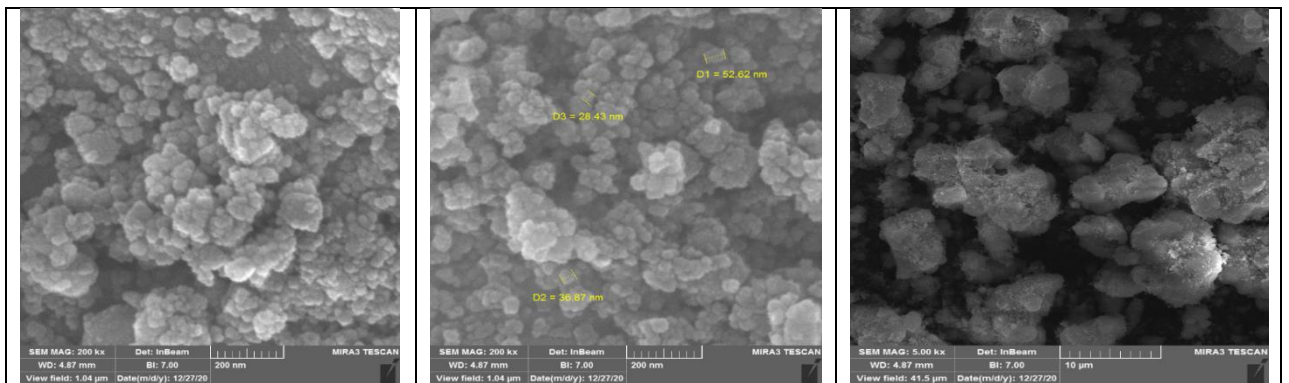
D

Figure (3-10). SEM of (a) commercial ZrO_2 , (b) prepared spinel $CoCr_2O_4$ nanoparticle , (c) composites 1:2 and (d) composites 1:3.

3.2.3 Energy Dispersive X-Rays (EDX)

The results of the EDX spectra have demonstrated the composition of all stages in the catalyst preparation process, as illustrated in(Figures 3-11 to 3-14)and (tables 3-4 to 3-7). The spinel $CoCr_2O_4$ nanoparticles are made up of Co, Cr, and O, ZrO_2 NPs are made up of Zr and O, And the nanocomposites for spinel $CoCr_2O_4$-ZrO_2 NPs are made up of Co, Zr, Cr, and O. The sum of atom % (A%) and weight % (W%) was discovered to equal 100%.
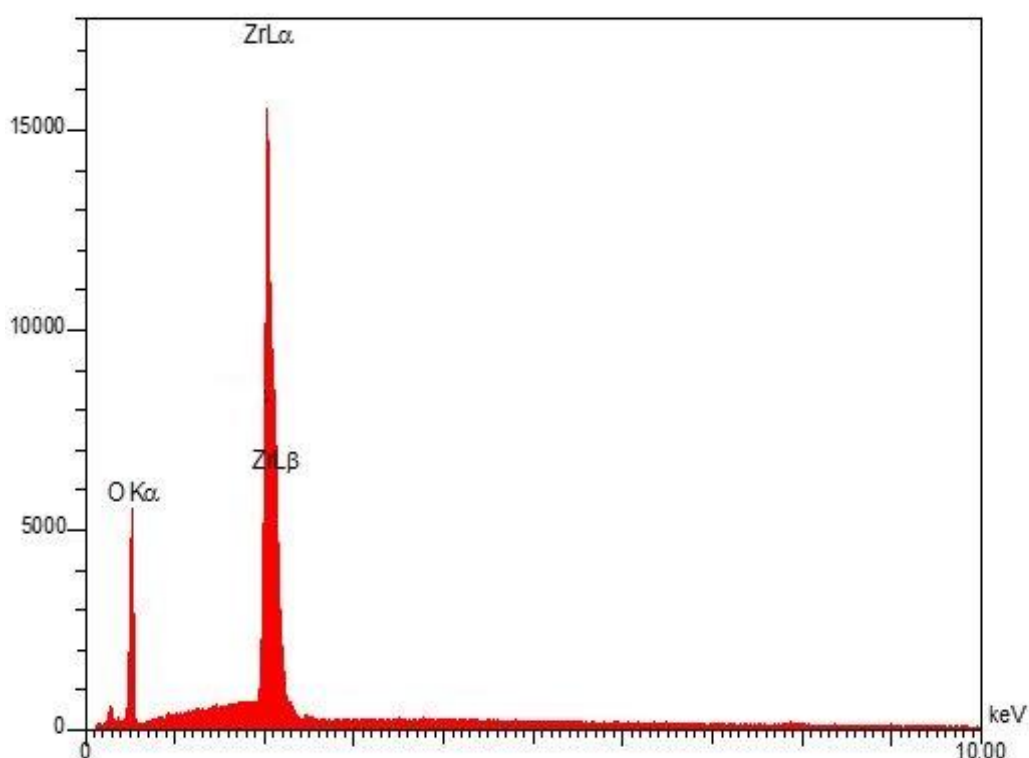
Figure 3-11. EDX spectrum of ZrO_2 commercial

Table 3.4. The value of the chemical composition obtained from EDX spectrum for ZrO_2

Elt	Line	Int	Error	K	Kr	W%	A%	ZAF F	Ox%	Pk/Bg	Class
O	Ka	534.6	125.6961	0.2547	0.14245	44.41	75.04	0.1867	0.00	297.23	A
Zr	La	2526.4	204.8345	0.7453	0.41685	55.59	24.96	0.7347	0.00	300.47	A
				1.0000	0.5593	100.00	100.00		0.00		
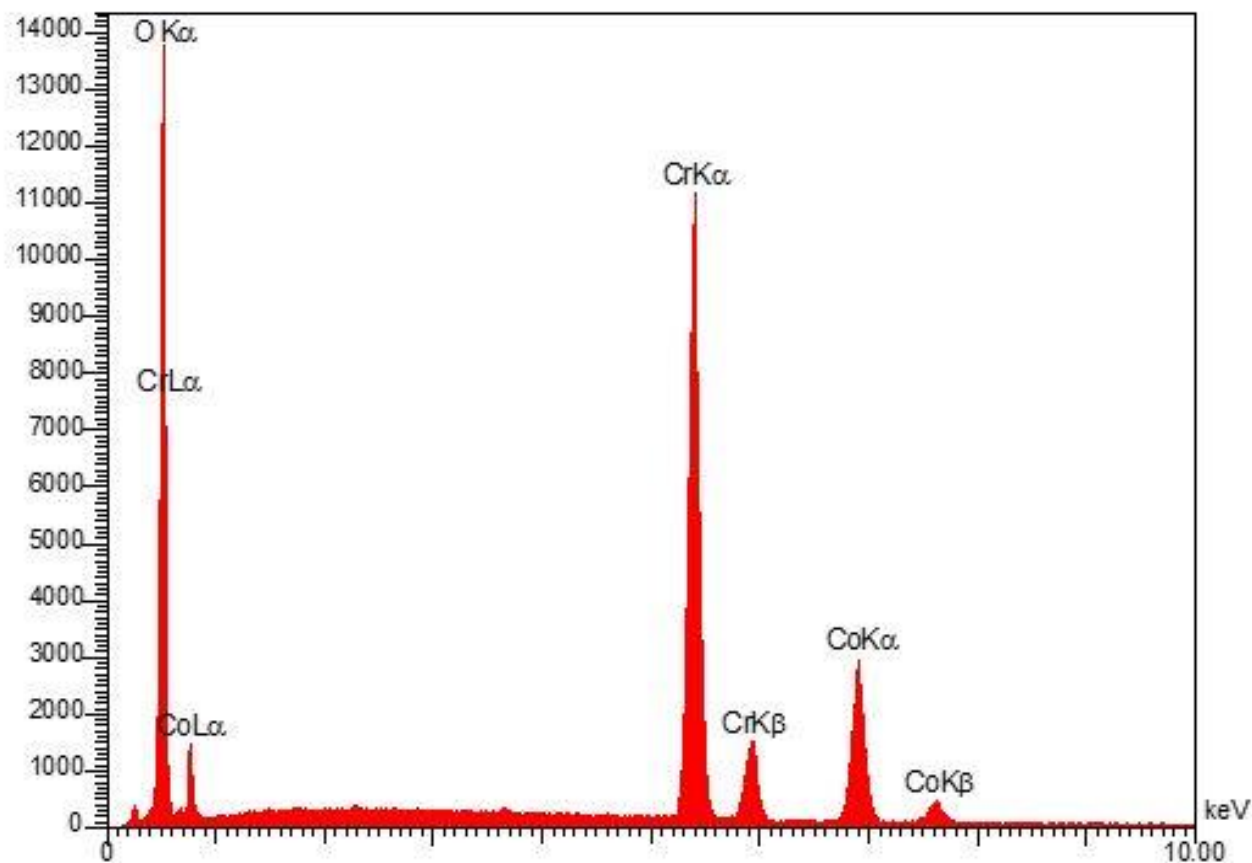
Figure(3-12). EDX spectrum of spinel CoCr$_2$O$_4$

Table 3-5. The value of the chemical composition obtained from EDX
spectrum for CoCr$_2$O$_4$

Elt	Line	Int	Error	K	Kr	W%	A%	ZAF	Formula	Ox%	Pk/Bg	Class	Cat#
O	Ka	1383.8	76.8611	0.2518	0.2163	30.74	59.79	0.7039		0.00	998.56	A	0.00
Cr	Ka	2387.8	0.8612	0.5727	0.4921	51.52	30.84	0.9552		0.00	52.41	A	0.00
Co	Ka	680.8	0.7436	0.1755	0.1508	17.75	9.37	0.8497		0.00	18.90	A	0.00
				1.0000	0.8592	100.00	100.00			0.00			0.00
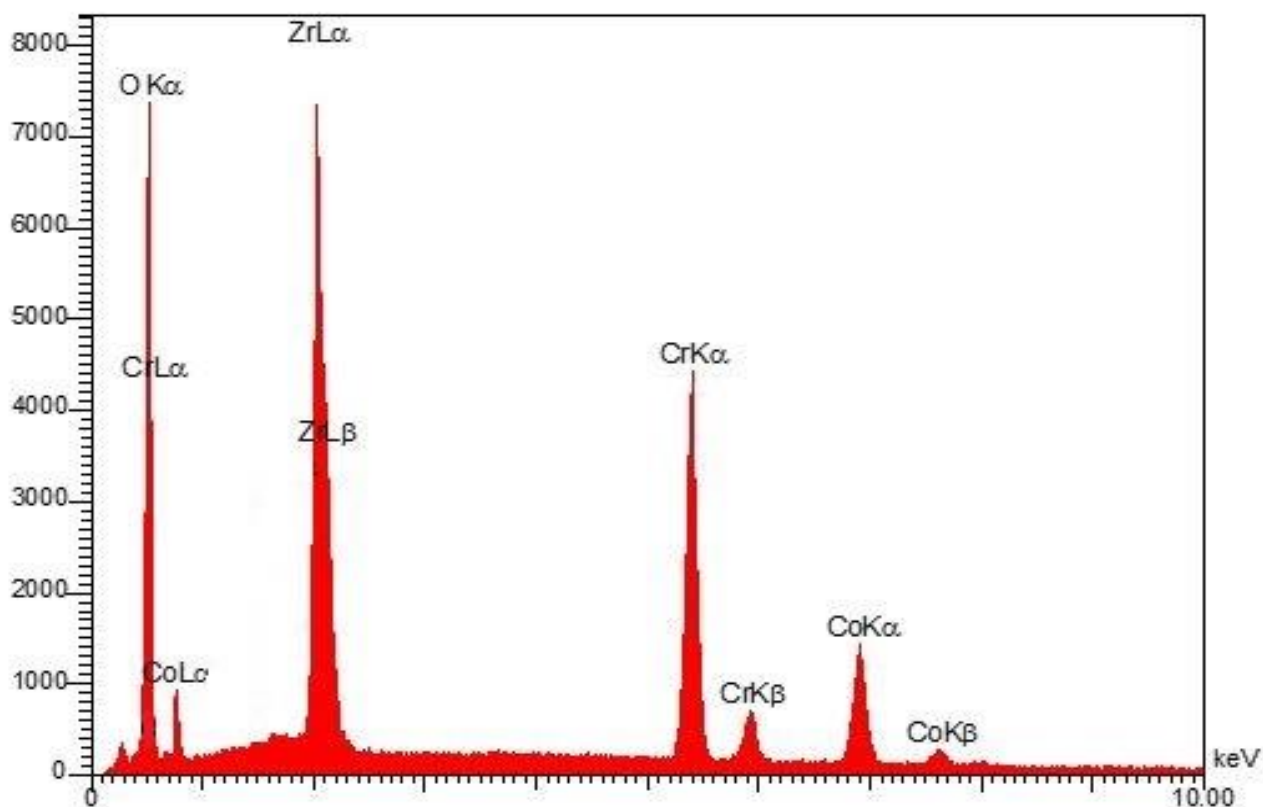
Figure 3-13. EDX spectrum of CoCr$_2$O$_4$- ZrO$_2$ (1:2) nanocomposite

Table 3.6. The   value of the chemical composition obtained from EDX spectrum for CoCr$_2$O$_4$- ZrO$_2$ (1:2) nanocomposite

Elt	Line	Int	Error	K	Kr	W%	A%	ZAF	Formula	Ox%	Pk/Bg	Class	Cat#
O	Ka	1161.4	94.9839	0.2639	0.1476	45.62	71.10	0.2990		0.00	739.07	A	0.00
Cr	Ka	1056.8	1.0204	0.3087	0.1726	20.68	12.44	0.8832		0.00	22.76	A	0.00
Co	Ka	340.0	1.2212	0.1325	0.0742	9.75	6.71	0.8512		0.00	9.11	A	0.00
Zr	La	1203.6	99.3362	0.2949	0.1650	23.95	9.77	0.7039		0.00	52.29	A	0.00
				1.0000	0.5594	100.00	100.00			0.00			0.00
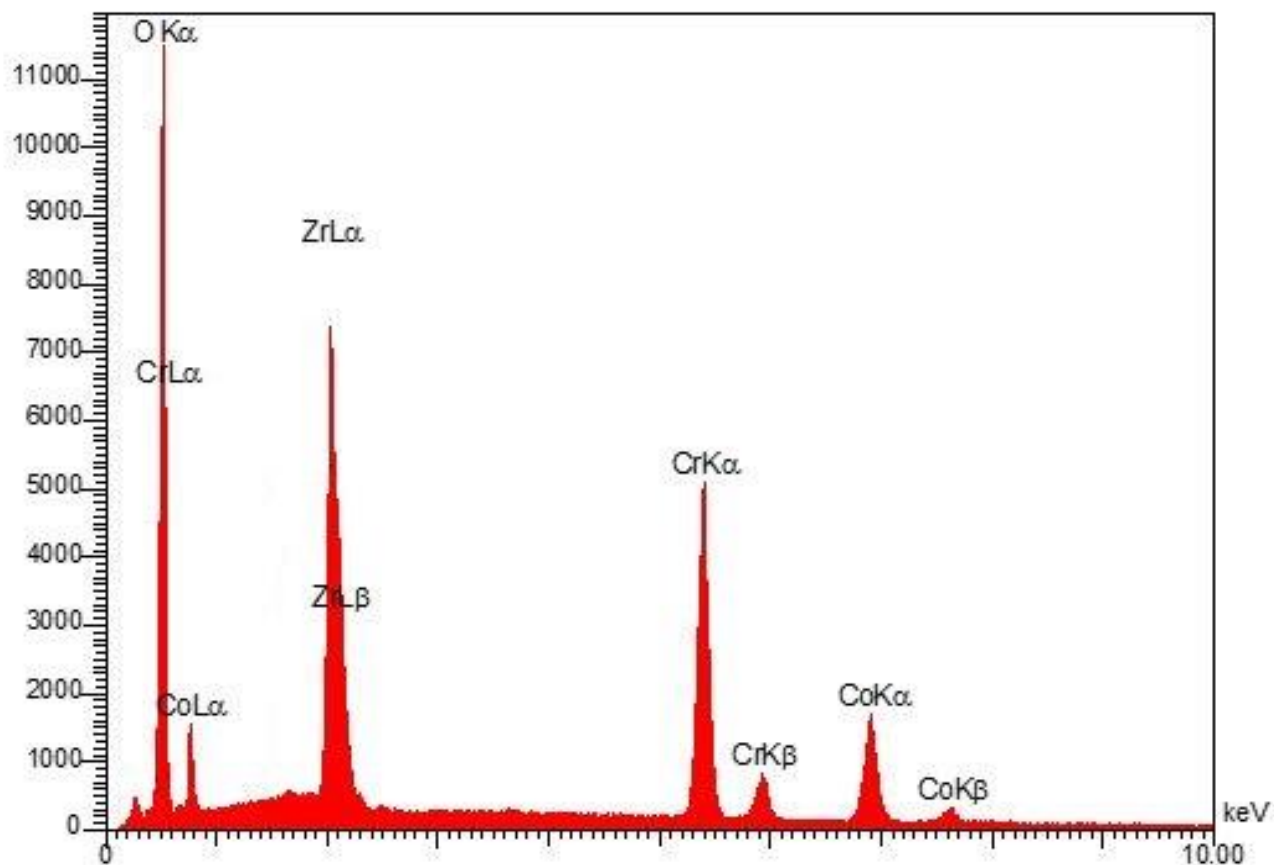
Figure (3-14). EDX spectrum of $CoCr_2O_4$- ZrO_2 (1:3) nanocomposite

Table 3.7. The value of the chemical composition obtained from EDX spectrum for $CoCr_2O_4$- ZrO_2 (1:3) nanocomposite

Elt	Line	Int	Error	K	Kr	W%	A%	ZAF	Formula	Ox%	Pk/Bg	Class
O	Ka	735.9	55.7847	0.2099	0.1231	40.39	68.35	0.2807		0.00	510.00	A
Cr	Ka	905.0	0.5365	0.3212	0.1884	22.01	13.73	0.8946		0.00	20.97	A
Co	Ka	285.1	0.6299	0.1292	0.0758	9.65	6.74	0.8636		0.00	8.38	A
Zr	La	1155.4	74.0248	0.3397	0.1993	27.95	11.18	0.7252		0.00	52.96	A
				1.0000	0.5868	100.00	100.00			0.00		

3.2.4 . Band Gap Energy Measurements

The direct bandgap energies for examined samples were measured based on the Tauc equation plots [166, 167] in figure (3-15). The high value of bandgap appears for commercial ZrO_2, which equals 5 eV(248 nm), but the low value of bandgap occurs for spinel $CoCr_2O_4$ and equals 3.18 eV(289.937 nm). The prepared composite in ratios 1:2 and 1:3 gave the medium values, with values of 4.7 eV(263.829 nm) and 4.8 eV(258.333 nm), respectively. In fact, the raised in bandgap values lead to a decrease in the mean crystal size of studied nanoparticles, which is a vital step in improving their optical properties when used as a photocatalyst.
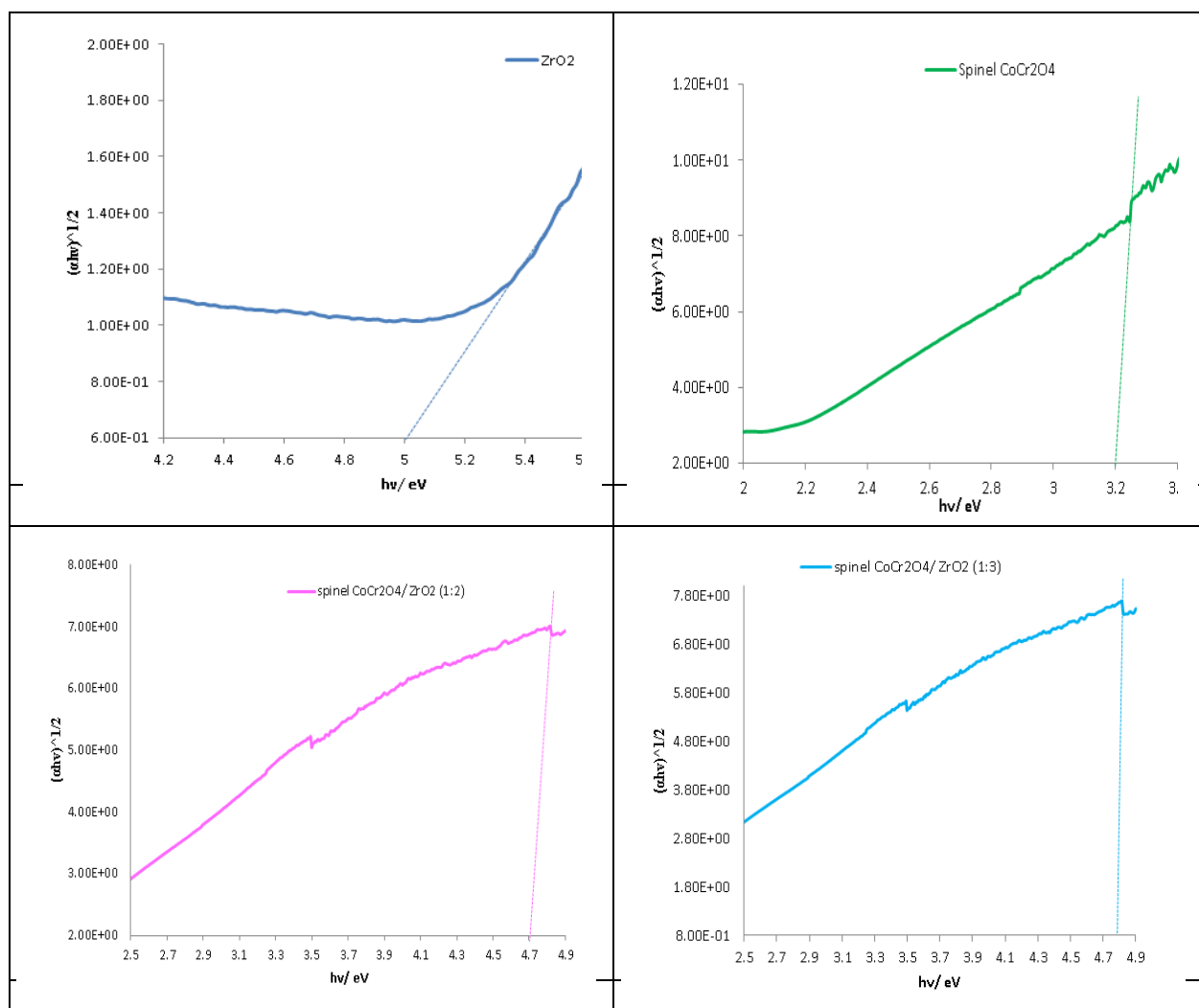
Figure (3-15). Band gap as a direct of (a) commercial ZrO_2 , (b) prepared spinel $CoCr_2O_4$ nanoparticle, (c) composites 1:2 and (d) composites 1:3.

3.2.5 Preliminary Experiments

Because the stability of Luminol -Fe^{2+} complex is very high under using UV-light in photolysis or photocatalyst (using ZrO_2 or $CoCr_2O_4$ or composites) that will enhance generated blue ring from Luminol-Fe^{2+} complex. As pictured in Figure (3-16).

Figure (3- 16). The real image for the generated blue ring between Luminol and Fe^{2+} under UV- light.

Hence, the using photolysis and photocatalysts under Uv-light are not active to decolorize it according to (equations 3-10 and 3-11).

luminol-Fe^{+2} complex + UV ⟶ No reaction   (3-10)

luminol-Fe^{+2} complex + photocatalyst + UV⟶ No reaction   (3-11)
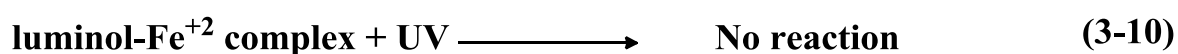
But, the illumination of the new complex of Fe(II)-(Luminol -Tyrosine) to UV – light is being controlled kinetically and lead to decolorize of this complex at neutral medium (pH = 7.3) [169,170]. As suggested in equation (3-12)

Fe(II)-(luminol-Tyrosine) + photocatalyst + UV⟶ reaction   (3-12)

3.3 Effect of Different Pomplex as Colored Solution

3.3.1. Effect of ZrO₂ Dose

These experiments were conducted at different ZrO_2 doses ranging from 0.1 g to 0.3 g / 100 mL at pH 7.3 and temperature 20 ºC and 100 mL of complex, light, intensity equivalent to (3.189×10^{-7} Enstine s^{-1}). Tables (3-8), (3-9), and Figure(3-17) exhibit the findings and statistics. The photo-decolorization effectiveness with using ZrO_2 increases with increasing the catalyst dosage and the best weight was found at 0.1 g/100 mL, with PDE% equal to 20.7017% at 40 min. After 0.1 g/100 mL, the rates of reaction decrease that due to a decrease in the penetration of light and caused the screen effect[168].

Table (3-8). The relationship between ln (A_o/A_t) and irradiation time at a different dose of commercial ZrO₂ via photocatalytic decolorization of Fe(II)-(Luminol -Tyrosine) complex.

Time of irradiation	Dose / g	$ln\,(A_o/A_t)$		
		0.1	0.2	0.3
0		0	0	0
5		0.0430	0.0069	0.0146
10		0.0879	0.0424	0.0332
15		0.1151	0.0680	0.0370
20		0.1431	0.0866	0.0484
30		0.1594	0.1019	0.0873
40		0.2319	0.1816	-
k_{app}/min^{-1}		**0.0061**	0.0042	0.0028

Table (3-9). The relationship between (PDE %) and irradiation time at a different dose of commercial ZrO₂ via photocatalytic decolorization of Fe(II)-(Luminol -Tyrosine) complex.

Time of irradiation	Dose/ g	PDE%		
		0.1	0.2	0.3
0		0	0	0
5		4.2105	0.6920	1.4545
10		8.4210	4.1522	3.2727
15		10.8771	6.5743	3.6363
20		13.3333	8.3044	4.7272
30		14.7368	9.6885	8.3636
40		**20.7017**	16.6089	-
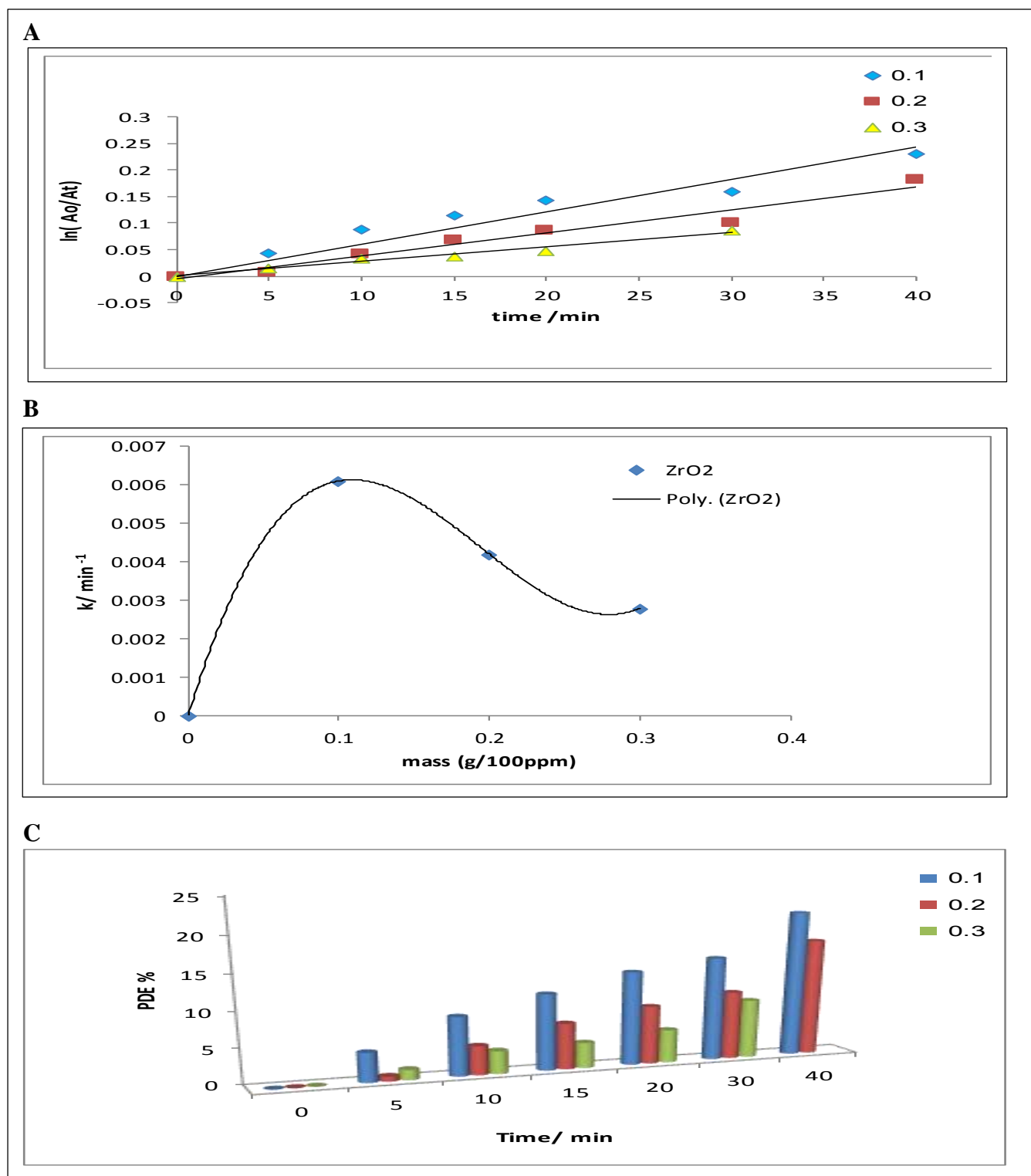
Figure (3-17). (A) The change of ln (A_o/A_t) with different dose of commercial ZrO_2, (B) Effect of k_{app} different dose of commercial ZrO_2 on photodecolorization efficiency. (C) relationship between (PDE %) and irradiation time at a different dose of ZrO_2

3.3.2. Effect of Spinel CoCr₂O₄ Dose

These experiments were conducted at different doses ranging from 0.1 g to 0.3 g/100 mL CoCr$_2$O$_4$ at pH 7.3 and temperature 20 ºC 100 mL of complex, light, intensity equivalent to (3.189×10^{-7} Enstine s^{-1}). In tables (3-10), (3-11) and Figure(3-18), the photo-decolorization effectiveness with employing of CoCr$_2$O$_4$ elevates with increasing the CoCr$_2$O$_4$ dosage and the best weight was occurred at 0.2 g/100 mL with PDE% equal to 36.8600 % at 40 min, while, after this dose, the rates of reaction depresses that also an attitude to screen effect.

Table (3-10). The relationship between ln (A$_o$/A$_t$) and irradiation time at a different dose of CoCr$_2$O$_4$ via photocatalytic decolorization of Fe(II)-(Luminol -Tyrosine) complex.

Time of irradiation t/min	Dose/ g	$ln\,(A_o/A_t)$		
		0.1	0.2	0.3
0		0	0	0
5		0.0536	0.0453	0.0367
10		0.1024	0.0854	0.0796
15		0.1291	0.0854	0.0894
20		0.1705	0.1667	0.1931
30		0.1933	0.2163	0.2787
40		0.2344	0.4598	0.3592
k$_{app}$/min^{-1}		0.0067	**0.0094**	0.0089

Table (3-11)). The relationship between (PDE %) and irradiation time at a different dose of commercial ZrO$_2$ via photocatalytic decolorization of Fe(II)-(Luminol -Tyrosine) complex.

Time of irradiation t/min	Dose/ g	PDE%		
		0.1	0.2	0.3
0		0	0	0
5		5.2256	4.4368	3.6036
10		9.7387	8.1911	7.6576
15		12.1140	8.1911	8.5585
20		15.6769	15.3583	17.5675
30		17.5771	19.4539	24.3243
40		20.9026	**36.8600**	30.1801

A

B

C

Figure (3-18).(A) The change of ln (A_o/A_t) with different dose of commercial $CoCr_2O_4$, (B) Effect of $k_{app.}$ different dose of commercial $CoCr_2O_4$ on photodecolorization efficiency. (C) relationship between (PDE %) and irradiation time at a different dose of $CoCr_2O_4$

3.3.3. Effect of Composite CoCr$_2$O$_4$/ ZrO$_2$ (1:2) Dose

These experiments were conducted at different doses ranging from 0.1g to 0.3 g/100 mL CoCr$_2$O$_4$ / ZrO$_2$ at pH 7.3 and temperature 20 °C 100 mL of complex, light, intensity equivalent to (3.189×10^{-7} Enstine s^{-1}). Based on tables (3-12), (3-13) and Figure(3-19), the photo-decolorization effectiveness with using CoCr$_2$O$_4$/ZrO$_2$ increases with increasing CoCr$_2$O$_4$/ZrO$_2$ dosage, and the best weights were at 0.1 g/100 mL with PDE% equal to 30.6772% at 30 min, and after 0.1 g/100, the rates of reaction depresses that also attitude to screen effect.

Table (3-12). The relationship between ln (A$_o$/A$_t$) and irradiation time at a different dose of CoCr$_2$O$_4$ / ZrO$_2$ (1:2) via photocatalytic decolorization of Fe(II)-(Luminol - Tyrosine) complex.

Time of irradiation t/min	Dose/ g	$ln\,(A_o/A_t)$		
		0.1	**0.2**	**0.3**
0		0	0	0
5		0.1138	0.1424	0.081
10		0.1688	0.1715	0.1245
15		0.1927	0.2061	0.1245
20		0.1975	0.2536	0.2170
30		0.3663	0.2918	0.3601
k$_{app}$/min^{-1}		**0.0122**	0.0117	0.0113

Table (3-13). The relationship between (PDE %) and irradiation time at a different dose of CoCr$_2$O$_4$ / ZrO$_2$ (1:2) via photocatalytic decolorization of Fe(II)-(Luminol -Tyrosine) complex.

Time of irradiation t/min	Dose/ g	PDE%		
		0.1	**0.2**	**0.3**
0		0	0	0
5		10.7569	13.2780	7.804878
10		15.5378	15.7676	11.7073
15		17.5298	18.6307	11.7073
20		17.9282	22.4066	19.5121
30		**30.6772**	25.3112	30.2439

A

B

C
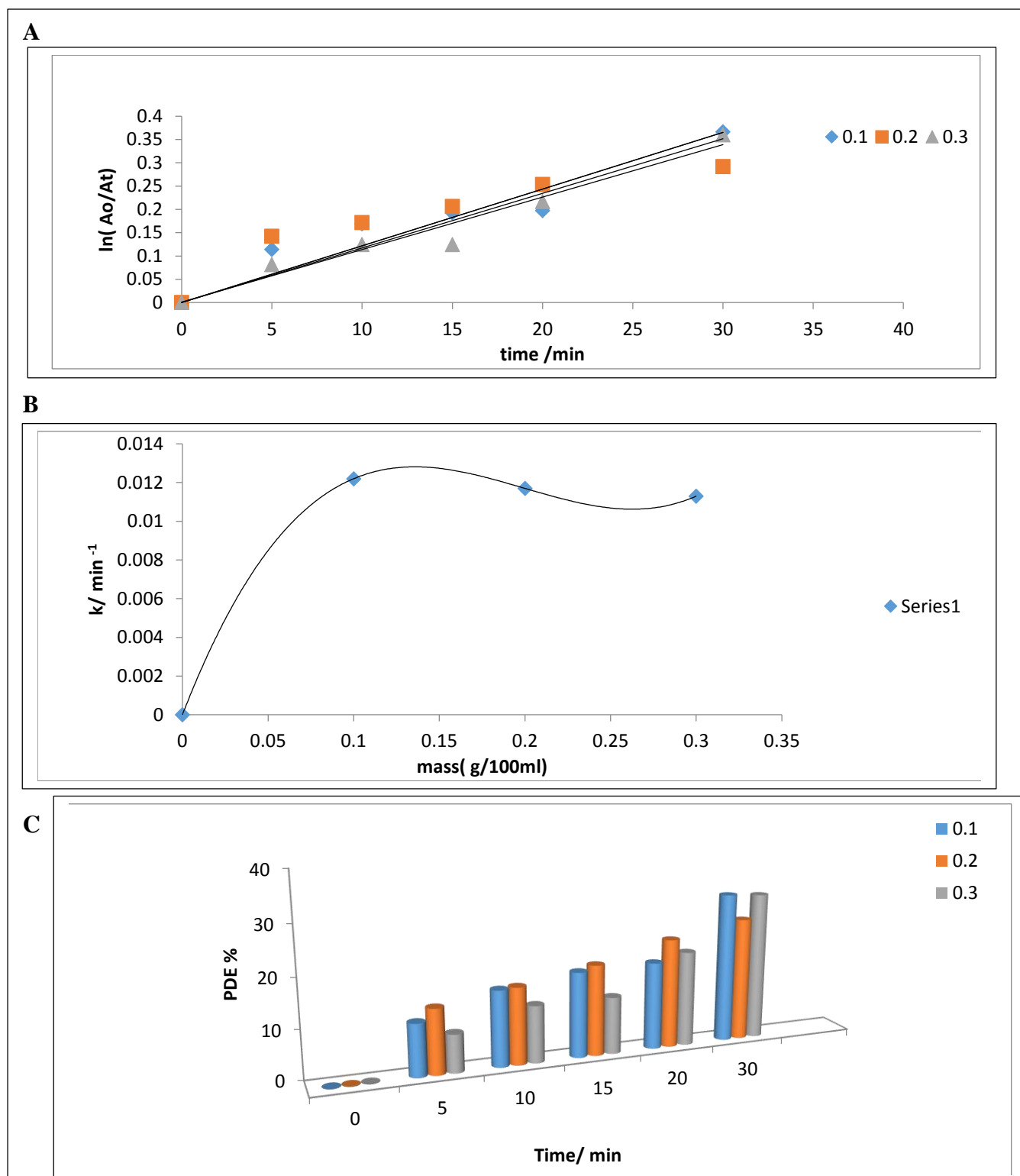
Figure (3-19). (A) The change of ln (A_0/A_t) with different dose of commercial $CoCr_2O_4$ / ZrO_2 (1:2), (B) Effect of $k_{app.}$ different dose of commercial $CoCr_2O_4/ZrO_2$ (1:2) on photodecolorization efficiency. (C) relationship between (PDE %) and irradiation time at a different dose of $CoCr_2O_4$ / ZrO_2 (1:2)

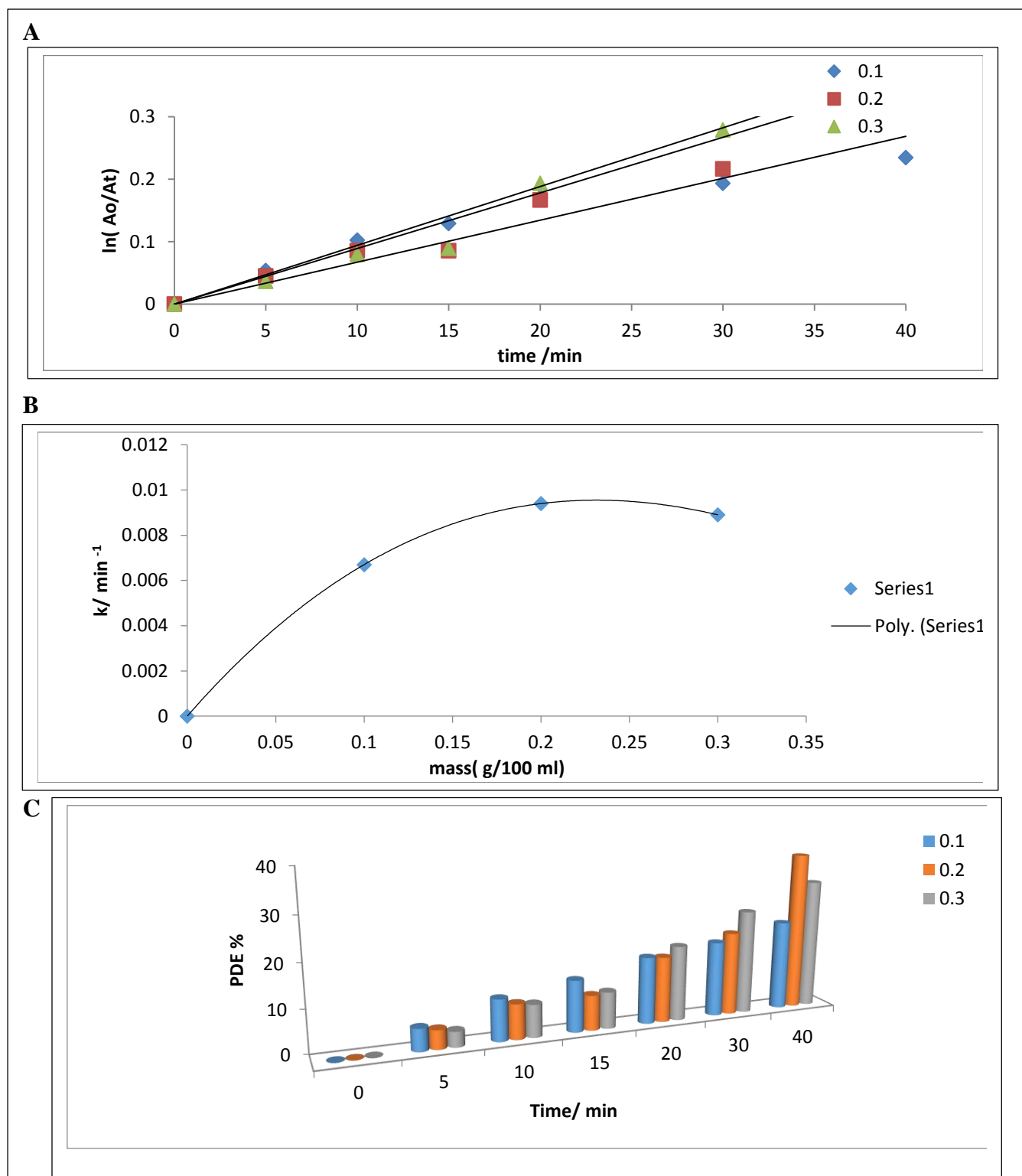## 3.3.4. Effect of Composite CoCr$_2$O$_4$/ ZrO$_2$ (1:3) Dose

These experiments were conducted at different doses ranging from 0.1g to 0.3 g/100 mL CoCr$_2$O$_4$ / ZrO$_2$ at pH 7.3 and temperature 20 °C 100 mL of complex, light, intensity equivalent to (3.189×10^{-7} Enstine s^{-1}). According to results in tables (3-14), (3-15) and Figure(3-20), the photo-decolorization effectiveness with the use of CoCr$_2$O$_4$ / ZrO$_2$ increases with increasing catalyst dosage and the best weight was at 0.1 g/100 with PDE% equal to 41.9718 % at 30 min, and then the rates of reaction depress that also the attitude to screen effect.

Table (3-14)   The relationship between ln (A$_o$/A$_t$) and irradiation time at a different dose of CoCr$_2$O$_4$ / ZrO$_2$ (1:3) via photocatalytic decolorization of Fe(II)-(Luminol - Tyrosine) complex.

Time of irradiation t/min	Dose/ g	ln (A$_o$/ A$_t$)		
		0.1	0.2	0.3
0		0	0	0
5		0.1919	0.0595	0.0616
10		0.2126	0.1562	0.1093
15		0.2302	0.2685	0.1363
20		0.3466	0.2685	0.2321
30		0.5442	0.3593	0.4440
k$_{app}$/min^{-1}		**0.0181**	0.0134	0.0130

Table (3-15). The relationship between (PDE %) and irradiation time at a different dose of CoCr$_2$O$_4$ / ZrO$_2$ (1:2) via photocatalytic decolorization of Fe(II)-(Luminol - Tyrosine) complex.

Time of irradiation t/min	Dose/ g	PDE%		
		0.1	0.2	0.3
0		0	0	0
5		17.4647	5.7851	5.9760
10		19.1549	14.4628	10.3585
15		20.5633	23.5537	12.7490
20		29.2957	23.5537	20.7171
30		**41.9718**	30.1886	35.8565

A

B

C
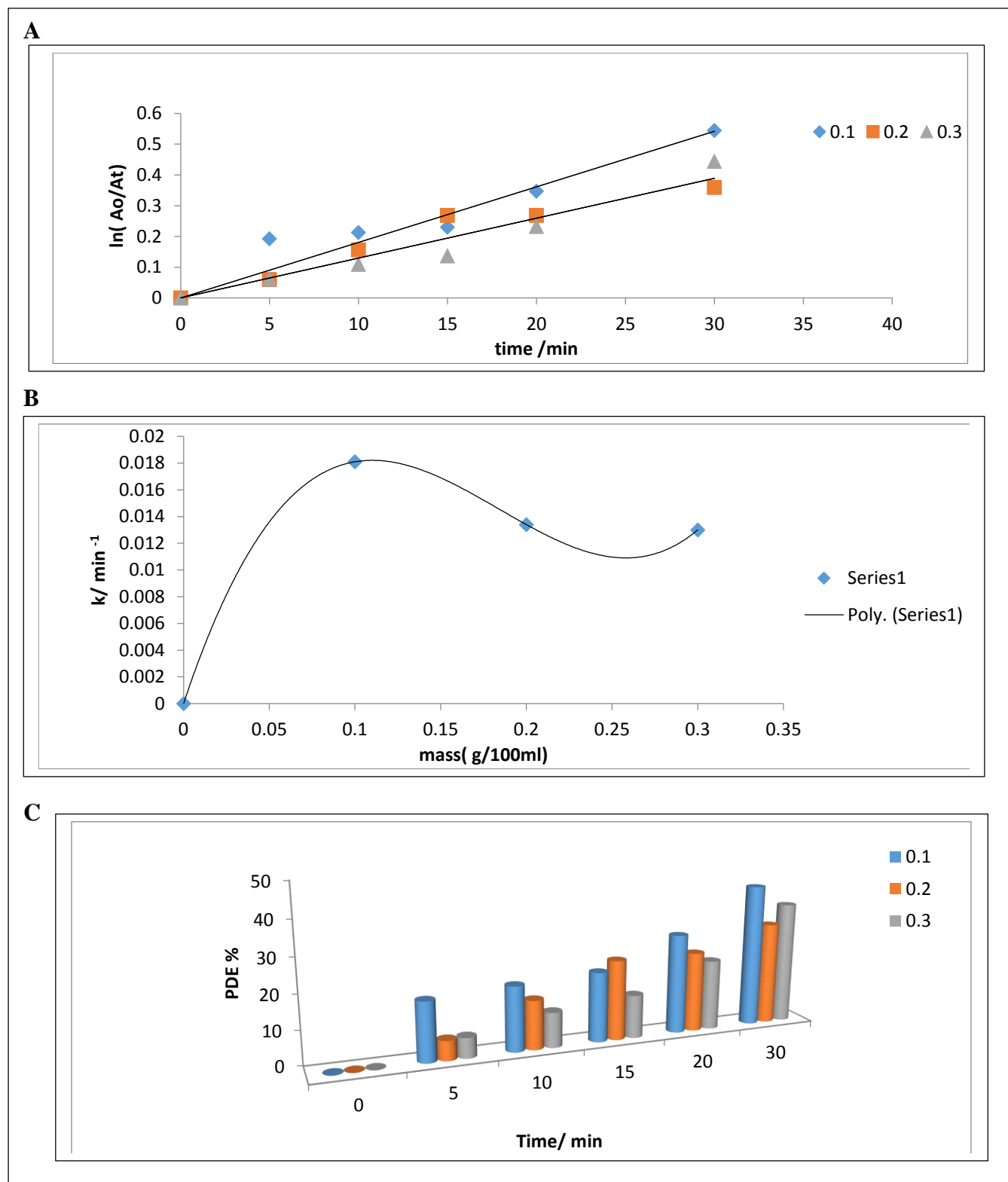
Figure (3-20). (A) The change of ln (A_0/A_t) with different dose of commercial $CoCr_2O_4$ / ZrO_2 (1:3), (B) Effect of k_{app} different dose of commercial $CoCr_2O_4/ZrO_2$(1:3) on photodecolorization efficiency.(C) relationship between (PDE %) and irradiation time at a different dose of $CoCr_2O_4$ / ZrO_2 (1:3).

3.4 Effect of Temperature

The photocatalytic decolorization of the Fe(II) complex was researched at various temperatures under the top mention conditions with ranged (20-35) °C.

A. Effect of temperature by Using Commercial ZrO₂

Table (3-16)   The relationship between Ln (A$_o$/A$_t$) and irradiation time at different temperatures by commercial ZrO₂ via photocatalytic decolorization of Fe(II)-(Luminol -Tyrosine) complex.

Time of irradiation t/min	T/ °C	$ln\ A_o/\ A_t$			
		20	25	30	35
0	0	0	0	0	0
5		0.0430	0.0920	0.0027	0.4977
10		0.0879	0.1321	0.0191	0.6193
15		0.1151	0.2013	0.0443	1.1032
20		0.1431	0.2174	0.1147	1.2140
25		-	0.2296	0.1269	1.3039
30		0,.1594	0.2715	0.5589	1.5122
40		0.2319	-	-	-
kapp/min⁻¹		0.0061	0.0101	0.0102	**0.056**
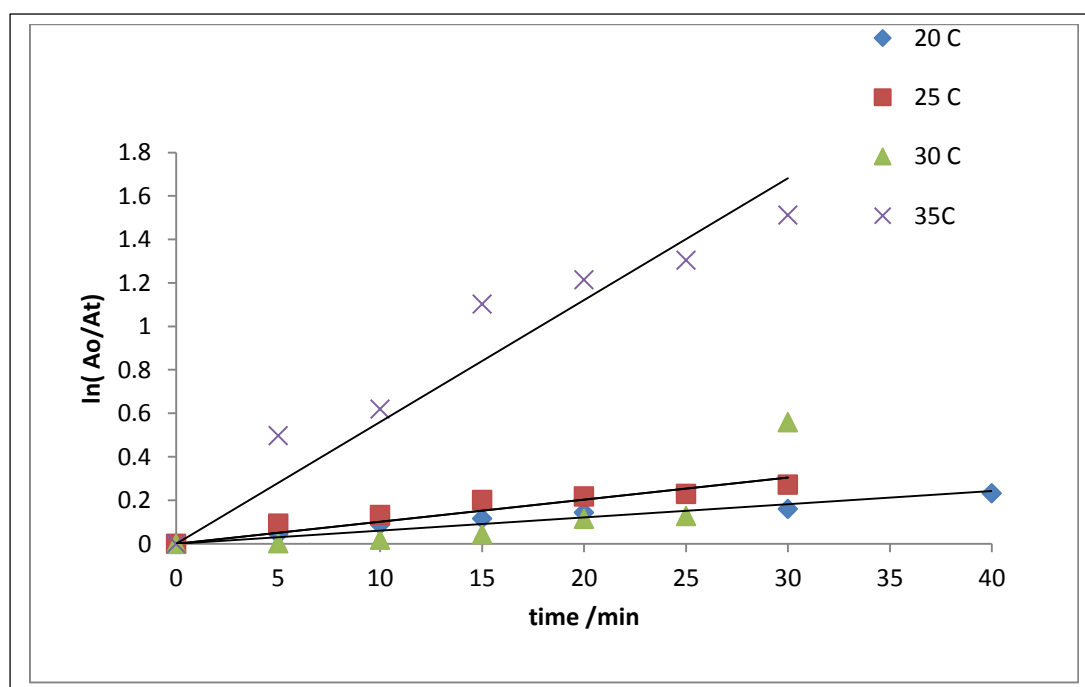
Figure (3-21). The change of ln(A$_o$/A$_t$) with Irradiation time at different temperatures of color solution for commercial ZrO₂.
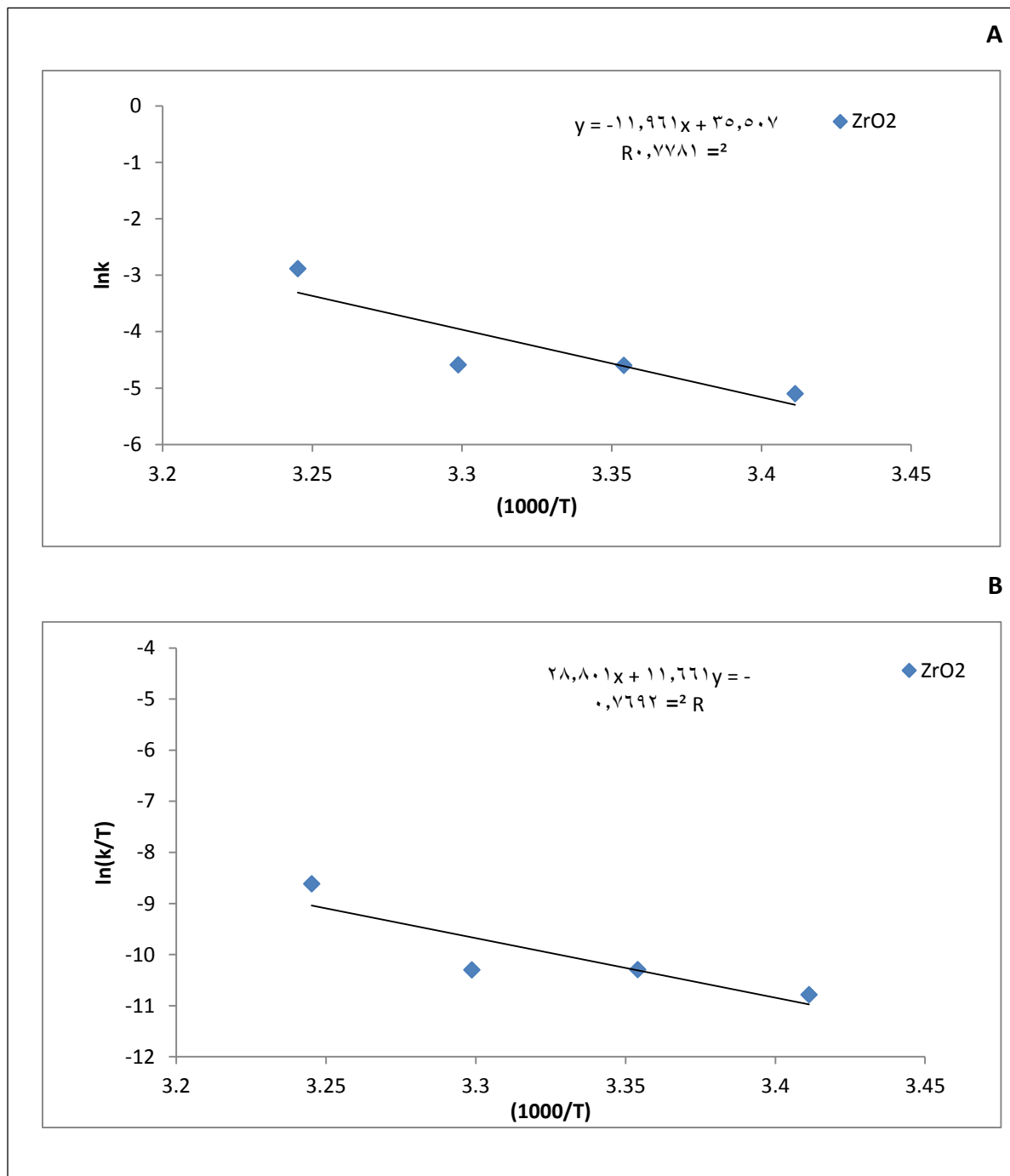
Figure (3-22). (A) Arrhenius plot by commercial ZrO_2,(B) Eyring-Polanyi plot ln(k/T) VS. 1000/T.

B. Effect of Temperature by Using Spinel $CoCr_2O_4$

Table (3-17). The relationship between Ln (A_o/A_t) and irradiation time at different temperatures by spinel $CoCr_2O_4$via photocatalytic decolorization of Fe(II)-(Luminol - Tyrosine) complex.

Time of irradiation t/min	T/ °C	ln A_o/A_t			
		20	25	30	35
0	0	0	0	0	0
5		0.0453	0.0268	0.0156	0.0049
10		0.0854	0.0451	0.0224	0.0099
15		0.0854	0.0948	0.0617	0.0149
20		0.1667	0.1120	0.0783	0.0351
25		-	0.1678	0.1175	0.0480
30		0.4598	0.2381	0.1530	0.0532
40		0.4598	-	-	-
kapp/min^{-1}		**0.0117**	0.0069	0.0045	0.0017
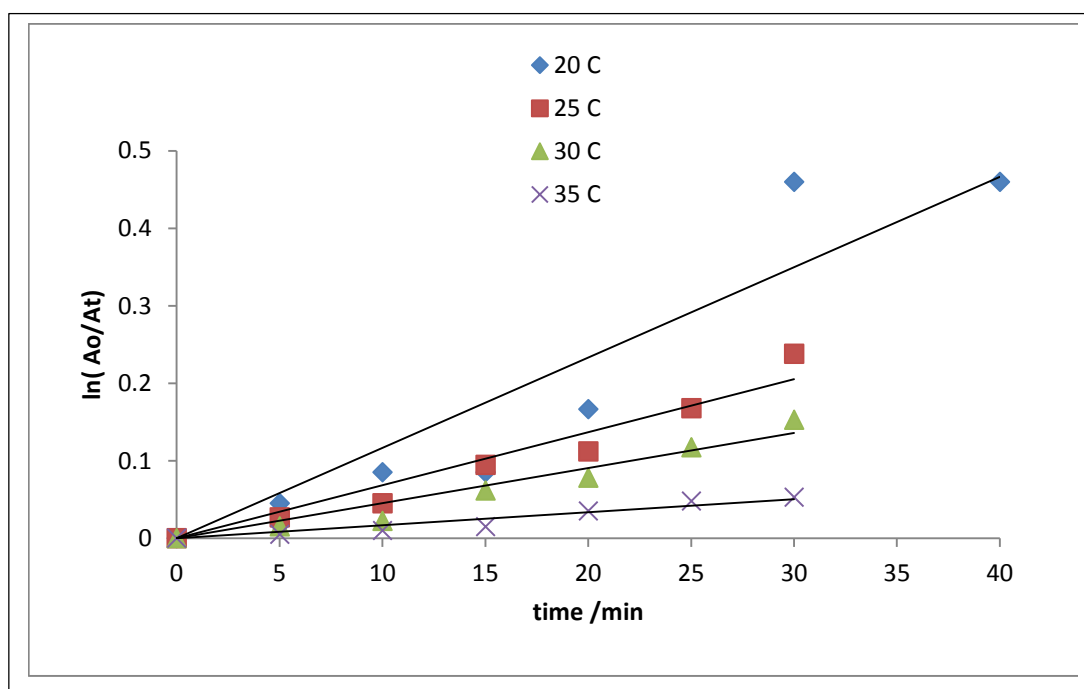
Figure (3-23). The change of ln(A_o/A_t) with Irradiation time at different temperatures of color solution for commercial $CoCr_2O_4$.
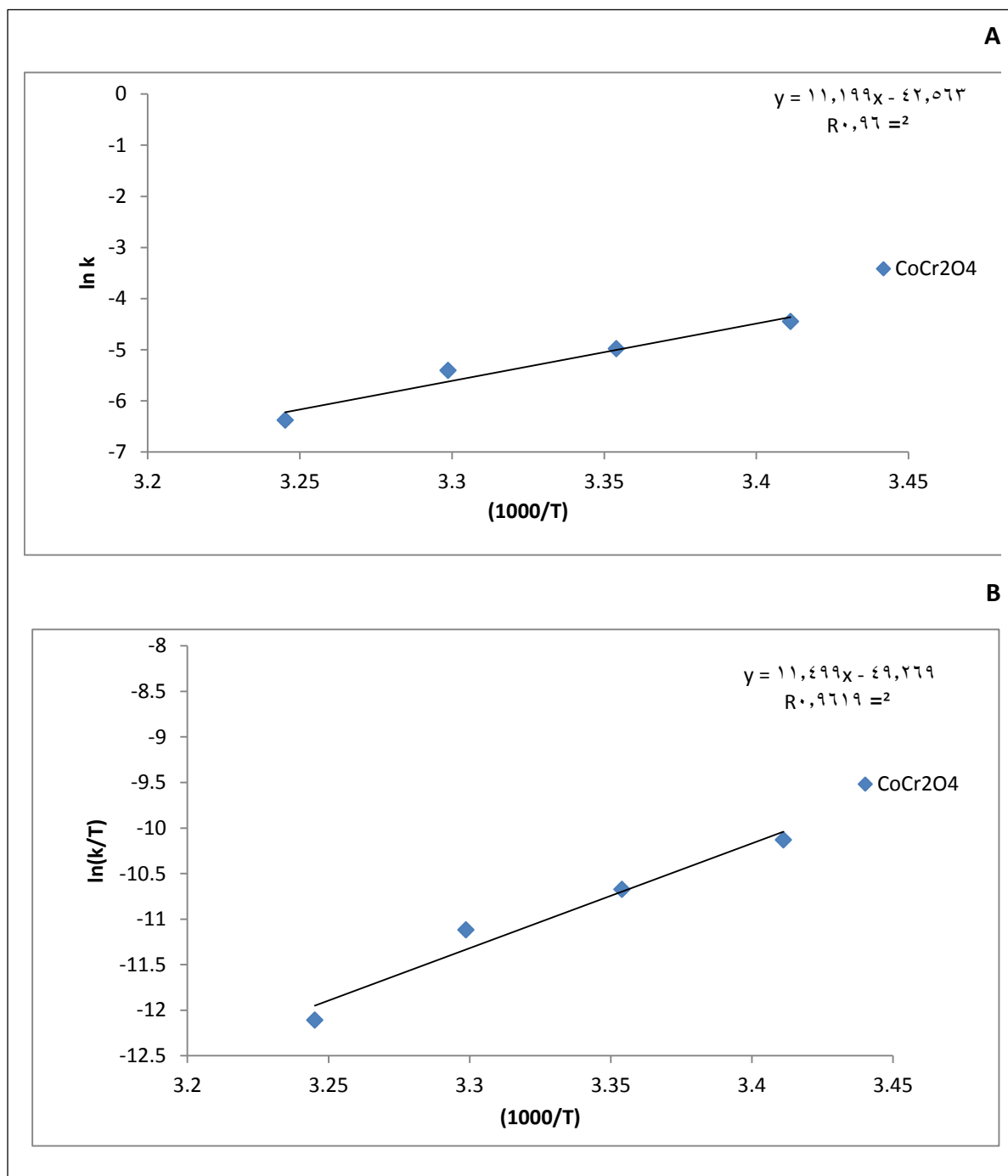
Figure (3-24). (A) Arrhenius plot by commercial CoCr₂O₄,(B) Eyring-Polanyi plot ln(k/T) VS. 1000/T.

C. Effect of Temperature by Using Composite CoCr$_2$O$_4$ / ZrO$_2$ (1:3)

Table (3-18))   The relationship between Ln (A$_o$/A$_t$) and irradiation time at different temperatures by CoCr$_2$O$_4$ / ZrO$_2$ (1:3) via photocatalytic decolorization of Fe(II)-(Luminol -Tyrosine) complex.

Time of irradiation t/min	T/ °C	ln A_o/ A_t			
		20	25	30	35
0	0	0	0	0	0
5		0.1138	0.0151	0.0157	0.0133
10		0.1688	0.0278	0.0236	0.0517
15		0.1927	0.0698	0.0643	0.0601
20		0.1975	0.1025	0.0839	0.0657
25		-	0.1221	0.0953	0.0743
30		-	0.1595	0.1694	0.1892
40		-	-	-	-
kapp/min^{-1}		**0.0121**	0.0005	0.0046	0.0045
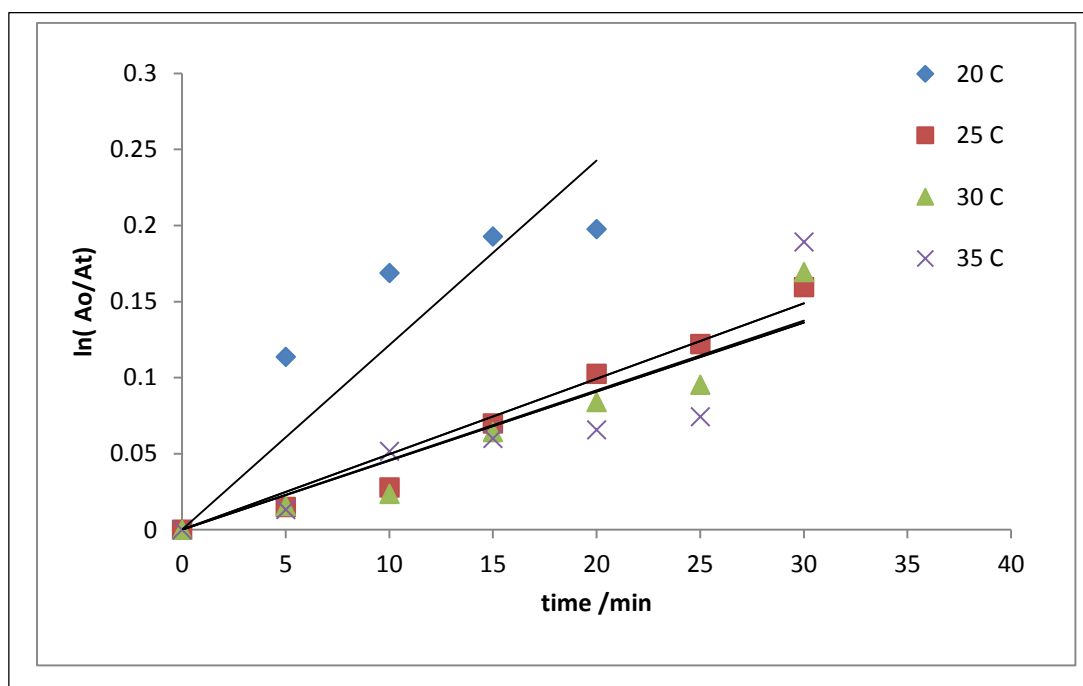
Figure (3-25). The change of ln(A$_o$/A$_t$) with Irradiation time at different temperatures of color solution for (1:3) spinel CoCr$_2$O$_4$/ZrO$_2$ composite.
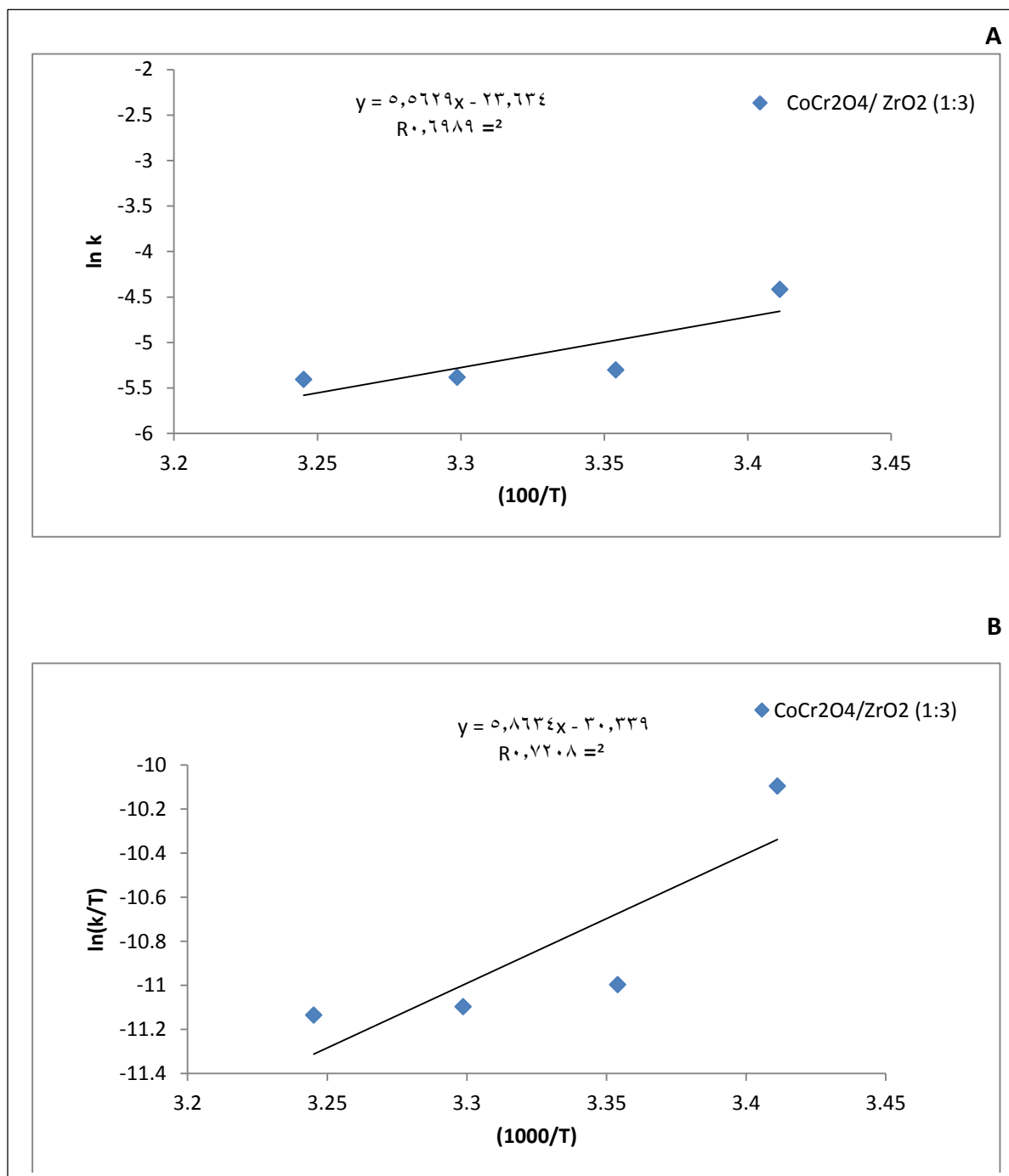
Figure (3-26). (A) Arrhenius plot by commercial CoCr$_2$O$_4$/ZrO$_2$ (1:3),(B) Eyring-Polanyi plot ln(k/T) VS. 1000/T.

Table (3-19) **Calculated activation energies and thermodynamic functions for decolorization of** FeL_2Cl_2**- complex with using commercials ZrO₂ and prepared Spinel CoCr₂O₄ and prepared (Spinel CoCr₂O₄/ ZrO₂) composite (1:3)**.

Samples	E_a /kJ mol^{-1}	$\Delta H^{\#}$/kJ mol^{-1}	$\Delta S^{\#}$/J mol^{-1} K^{-1}	$\Delta G^{\#}$/kJ mol^{-1}
ZrO₂	99.4437	96.9495	41.9108	105.6733
Spinel CoCr₂O₄	-93.1084	-95.6035	-607.1631	30.7768
(Spinel CoCr₂O₄/ ZrO₂) composite (1:3)	-46.2499	-48.7483	-449.7865	44.8754

The results in figures (3- 21), (3-23) and (3-25) and table (3-19) illustrated the ZrO₂ has a maximum value of activation energy that due to having a large bandgap (The activation energy is a less amount of energy that needed to eliminate the electron from valance band to the conductive band), while when incorporated it with the Spinel CoCr₂O₄. The activation energy is decreased clearly.

The activation energies befor and after incorporation of ZrO₂ with Spinel CoCr₂O₄ surface found to be negative values, that may indicate to happen the photoreaction in multi-steps binding, one of which may be exothermic then conversion at a very low positive activation energy value via a series of chain reactions. This behaver investigates to the spinel stracture, which involves Co(II) in tetrahydral hybridize and Cr(III) in octahedral bybridze, hence a fast binding step may be occured on Co(II) position in crystal lattice, but the less fast step (at very low positive activation energy value) may be obtained on Cr(III) position in crystal lattice. This case leads to produce a negative enthalpy values using spinel and its composite.

The photoreaction for decolorization of FeL_2Cl_2 - complex in present ZrO₂ obtain endothermic beaver. In contrast, the photoreaction for this complex in present spinel CoCr₂O₄ and its composite (1:3) is an exothermic and low change

in entropy for using composite and depress from 41.9108 J mol^{-1} K^{-1} to -449.7865 J mol^{-1} K^{-1}. The positive value of change in enthalpy and change in Gibbs energy for using spinel ZrO_2 refer to elevate the solvated between the hydroxyl radical and the transition state for the used complex in the transition state. This case is similar to the reported in the refernces [171,172].

3.5 Effect of Initial pH of the Solution

The study of the influence of pH of the solution is a vital factor, because of it's affected on the complex formation and the surface of the used catalyst. In this work, the best pH for formed this complex is 7.3, while, the pH less or more this value is not led to produce a FeL_2Cl_2- complex that due to change the structure and wavelength.

3.6 Conclusions

From this study, the sequence of conclusions was determined.

1. The synthesis of ligands as Luminol, (Luminol -Tyrosine) and of Fe(II)-(Luminol -Tyrosine) complex were confirmed by ^{1}H-NMR, altering in melting points, FT-IR, Elemental Micro Analysis (C.H.N), and UV-Visible scans.

2. The FeL_2Cl_2 complex was found to be highly stable and the ratio between Fe(II): L is 1:2 and had an octahedral hybridize.

3. By measuring the magnetic susceptibility of the prepared complex, it was found that the prepared complex is having a magnetic property due to the presence of repulsive electrons in the outer shell (d^6).

4. The spaniel $CoCr_2O_4$ was successfully synthesized by the co-precipitation method.

5. Spinel $CoCr_2O_4$ surface was modified by incorporating it with ZrO_2 by ultrasonic technique to form a composite in different ratios (1:2 and 1:3) respectively.

6. According to XRD analysis, the spinel $CoCr_2O_4$ were proved to the synthesized really with nano-sizes. Spinel $CoCr_2O_4$ /ZrO_2 composites in different ratios (1:2 and 1:3) found to be a nano quantum dots (NQDs) compounds.

7. SEM analysis detected the morphology of studied photocatalysts and found all samples are quasi-spherical shape except ZrO_2 is having a spherical shape.

8. The particle sizes for all studied photocatalysts are large than the crystal sizes. Hence, these samples regard as poly-crystals.

9. Based on optical analysis using the Tauc equation and found all studied photocatalysts are having a direct bandgaps. Moreover, an elevated amount of ZrO_2 in a prepared composite leads to a rise in the bandgap values in composite.

10. The best decolorization of FeL_2Cl_2 complex at pH 7.3 , in present spaniel $CoCr_2O_4$ or ZrO_2 or spaniel $CoCr_2O_4$/ZrO_2 nanocomposite in ratio1:3. This photoreaction is obeyed to pseudo-first-order kinetics.

11. The incorporation of ZrO_2 with spinel $CoCr_2O_4$ leads to elevate the efficiency of decolorizing the complex and depress the activation energy of this photoreaction.

12. The thermodynamic parameters for decolorization of the complex using ZrO_2, spinel $CoCr_2O_4$ and composite $CoCr_2O_4$/ ZrO_2 (1:3) are studied. By comparing them, it is clear that the reaction with using photocatalysts is fast, less random, and non-spontaneous, and the photoreaction in present ZrO_2 is endothermic, while in present spinel $CoCr_2O_4$ and it composite (1:3) are an exothermic.

3.7 Future Works

1. Possibility of studying the usage of the Ligand (luminol-tyrosine) in Forensic science and criminalistics.

2. The possibility of using the ligand in the preparation of another complex with other elements such as Zn, Cu, and Co.

3. The possibility of preparing new azo ligands derived from luminol to obtain new ligands.

4. Possibility of using spinel and other compounds in applications such as solar cells and gas sensors.

5. Determined the other characterizations for these prepared composites, such as surface area, TEM, and XPS.

6. Preparation composites with other oxides such as TiO_2 or ZnO

7. Measured the biological activity of the prepared spinel, composites, and complex. The decrease in the number of micro-organisms in water is performed with the photo-oxidation process.

8. The usage of photocatalyst in this study to remove other organic pollutants such as drugs, fertilizers, medicines, etc. Also, it is possible to study the adsorption of catalytic diodes prepared for heavy ions polluting the water.

References

References

[1]M. I, P. S. Kumar, V. Selvam, and S. G. Babu, "Recent advances in nanomaterials for wastewater treatment," *Adv. Nanostructured Mater. Environ. Remediat.*, pp. 21–58, 2019.

[2]V. V Pokropivny and V. V Skorokhod, "Classification of nanostructures by dimensionality and concept of surface forms engineering in nanomaterial science," *Mater. Sci. Eng. C*, vol. 27, no. 5–8, pp. 990–993, 2007.

[3]A. Kausar, "Proton exchange fuel cell membranes of poly (benzimidazole-amide)/sulfonated polystyrene/titania nanoparticles-grafted-multi-walled carbon nanotubes," *J. Plast. Film Sheeting*, vol. 31, no. 1, pp. 27–44, 2015.

[4]A. Kausar, I. Rafique, and B. Muhammad, "Aerospace application of polymer nanocomposite with carbon nanotube, graphite, graphene oxide, and nanoclay," *Polym. Plast. Technol. Eng.*, vol. 56, no. 13, pp. 1438–1456, 2017.

[5]A. Kausar, "A review of filled and pristine polycarbonate blends and their applications," *J. Plast. Film Sheeting*, vol. 34, no. 1, pp. 60–97, 2018.

[6]A. Kausar, "State-of-the-Art overview on polymer/POSS nanocomposite," *Polym. Plast. Technol. Eng.*, vol. 56, no. 13, pp. 1401–1420, 2017.

[7]A. Kausar, "Scientific potential of chitosan blending with different polymeric materials: A review," *J. Plast. Film Sheeting*, vol. 33, no. 4, pp. 384–412, 2017.

[8]A. Kausar, "Bucky papers of poly (methyl methacrylate-co-methacrylic acid)/polyamide 6 and graphene oxide-montmorillonite," *Dispers. Sci. Technol.,* vol. 37, no. 1, pp. 66–72, 2016.

[9]R. Aversa, M. H. Modarres, S. Cozzini, R. Ciancio, and A. Chiusole, "The first annotated set of scanning electron microscopy images for nanoscience," *Sci. data*, vol. 5, no. 1, pp. 1–10, 2018.

[10]B.W. Shiau,C.H. Lin,Y.Y. Liao,Y.R. Lee,S.H. Liu,W.C. Ding and J.R.Lee, "The characteristics and mechanisms of Au nanoparticles processed by functional centrifugal procedures," *J. Phys. Chem. Solids*, vol. 116, pp. 161–167, 2018.

[11]A.S.Lozhkomoev,A.V.Pervikova,A.V.Chumaevskya,E.S.Dvilisb,V.D.Pa yginb , O.L.Khasanovb and M.I.Lerner, "Fabrication of Fe-Cu composites from electroexplosive bimetallic nanoparticles by spark plasma sintering," *Vacuum*, vol. 170, p. 108980, 2019.

[12]Y. Oh, J. Lee, and M. Lee, "Fabrication of Ag-Au bimetallic nanoparticles by laser-induced dewetting of bilayer films," *Appl. Surf. Sci.*, vol. 434, pp. 1293–1299, 2018.

[13]R. M. Abozaid ,Z. Ž. Lazarević,L. Radović,M. Gilić,D. Šević, M.S. Rabasović and V. Radojević , "Optical properties and fluorescence of quantum dots CdSe/ZnS-PMMA composite films with interface modifications," *Opt. Mater. (Amst).*, vol. 92, pp. 405–410, 2019.

[14]A. S. Abdulhameed, A.-T. Mohammad, and A. H. Jawad, "Application of response surface methodology for enhanced synthesis of chitosan tripolyphosphate/TiO2 nanocomposite and adsorption of reactive orange 16 dye," *J. Clean. Prod.,* vol. 232, pp. 43–56, 2019.

[15]H. L. Parker, A. J. Hunt, V. L. Budarin, P. S. Shuttleworth, K. L. Miller, and J. H. Clark, "The importance of being porous: polysaccharide-derived mesoporous materials for use in dye adsorption," *RSC Adv.,* vol. 2, no. 24, pp. 8992–8997, 2012.

[16] C. Klingshirn, "Review of the Linear Optical Properties," *Semicond. Opt.*, pp. 461–465, 2007.

[17]D. Liang and J. E. Bowers, "Recent progress in lasers on silicon," *Nat. Photonics*, vol. 4, no. 8, pp. 511–517, 2010.

[18] K. Seeger,"Semiconductor Physics An Introduction **",** 9th edition, Springer-Verlag Berlin Heidelberg, Germany, CH1, 2004.

[19] Kasap, S. and Capper,Optoelectronic Devices and Materials, Springer Handbook of Electronic and Photonic Materials,Springer US,p.887–916 ,2007 .

[20]S. W. Shin, I. H. Song, and S. H. Um, "Role of physicochemical properties in nanoparticle toxicity," *Nanomaterials*, vol. 5, no. 3, pp. 1351–1365, 2015.

[21]M. L. Hassan, A. F. Ali, A. H. Salama, and A. M. Abdel-Karim, "Novel cellulose nanofibers/barium titanate nanoparticles nanocomposites and their electrical properties," *J. Phys. Org. Chem.*, vol. 32, no. 2, p. e3897, 2019.

[22]R. Lamouri, O. Mounkachi, E. Salmani, M. Hamedoun, A. Benyoussef, and H. Ez-Zahraouy, "Size effect on the magnetic properties of CoFe2O4 nanoparticles: a Monte Carlo study," *Ceram. Int.*, vol. 46, no. 6, pp. 8092–8096, 2020.

[23]V. G. Shrimali et al., "Size dependent dielectric, magnetic, transport and magnetodielectric properties of BiFe0. 98Co0. 02O3 nanoparticles," *J. Alloys Compd.*, vol. 817, p. 152685, 2020.

[24]H. R. Lakshmiprasanna, V. J. Angadi, B. R. Babu, M. Pasha, K. Manjunatha, and S. Matteppanavar, "Effect of Pr3+-doping on the structural, elastic and magnetic properties of Mn–Zn ferrite nanoparticles prepared by

solution combustion synthesis method," *Chem. Data Collect.*, vol. 24, p. 100273, 2019.

[25]H. S. Mansur, "Quantum dots and nanocomposites," *Wiley Interdiscip. Rev. Nanomedicine Nanobiotechnology*, vol. 2, no. 2, pp. 113–129, 2010.

[26]A. P. Alivisatos, "Semiconductor clusters, nanocrystals, and quantum dots," *Science (80-.).*, vol. 271, no. 5251, pp. 933–937, 1996.

[27]J. Zheng, J. Zhang, Z. Wang, L. Zhong, Y. Sun, Z. Liang, Y. Li, L. Jiang, X. Chen, L. Chie , "Programmable Negative Differential Resistance Effects Based on Self-Assembled Au@ PPy Core–Shell Nanoparticle Arrays," *Adv. Mater.,* vol. 30, no. 35, p. 1802731, 2018.

[28]J. Low, J. Yu, M. Jaroniec, S. Wageh, and A. A. Al-Ghamdi, "Heterojunction photocatalysts," *Adv. Mater.*, vol. 29, no. 20, p. 1601694, 2017.

[29]Z. Ma, C. Wu, D. U. Lee, F. Li, and T. W. Kim, "Carrier transport and memory mechanisms of multilevel resistive memory devices with an intermediate state based on double-stacked organic/inorganic nanocomposites," *Org. Electron.*, vol. 28, pp. 20–24, 2016.

[30]P. Reiss, M. Protiere, and L. Li, "Core/shell semiconductor nanocrystals," *small*, vol. 5, no. 2, pp. 154–168, 2009.

[31]D. A. Badounas, M. Souliotis, and C. S. Garoufalis, "Theoretical Study of Linear and Nonlinear Optical Properties of ZnO/MgO Core/Shell and Inverted Core/Shell Quantum Dots," *J. Adv. Phys.*, vol. 6, no. 4, pp. 477–481, 2017.

[32]S. Kim, B. Fisher, H.-J. Eisler, and M. Bawendi, "Type-II quantum dots: CdTe/CdSe (core/shell) and CdSe/ZnTe (core/shell) heterostructures," *J. Am. Chem.* Soc., vol. 125, no. 38, pp. 11466–11467, 2003.

[33]J. Shen, Y. Zhu, X. Yang, and C. Li, "Graphene quantum dots: emergent nanolights for bioimaging, sensors, catalysis and photovoltaic devices," *Chem. Commun.*, vol. 48, no. 31, pp. 3686–3699, 2012.

[34]S. J. Phang and L.-L. Tan, "Recent advances in carbon quantum dot (CQD)-based two dimensional materials for photocatalytic applications," *Catal. Sci. Technol.,* vol. 9, no. 21, pp. 5882–5905, 2019.

[35]P. Devi, S. Saini, and K.-H. Kim, "The advanced role of carbon quantum dots in nanomedical applications," *Biosens. Bioelectron.*, vol. 141, p. 111158, 2019.

[36]K. J. Mintz, Y. Zhou, and R. M. Leblanc, "Recent development of carbon quantum dots regarding their optical properties, photoluminescence mechanism, and core structure," *Nanoscale*, vol. 11, no. 11, pp. 4634–4652, 2019.

[37]Y. Dong, N. Zhou, X. Lin, J. Lin, Y. Chi, and G. Chen, "Extraction of electrochemiluminescent oxidized carbon quantum dots from activated carbon," *Chem. Mater.*, vol. 22, no. 21, pp. 5895–5899, 2010.

[38]W. Kuang, H. Tolner, and Q. Li, "Cathode-luminescence diagnostics of MgO, MgO: Si, MgO: Sc, and MgCaO," J. Soc. Inf. Disp., vol. 20, no. 1, pp. 63–69, 2012.

[39]R. Tomar, A. A. Abdala, R. G. Chaudhary, and N. B. Singh, "Photocatalytic degradation of dyes by nanomaterials," *Mater. Today Proc.*, vol. 29, pp. 967–973, 2020.

[40]E. Roduner, "Size matters: why nanomaterials are different," *Chem. Soc. Rev.*, vol. 35, no. 7, pp. 583–592, 2006.

[41]E. Roduner, "Quantum confinement: Size on the grill!," *J. Phys. Chem. Solids*, vol. 140, p. 109320, 2020.

[42]S. K. Krishnan, E. Singh, P. Singh, M. Meyyappan, and H. S. Nalwa, "A review on graphene-based nanocomposites for electrochemical and fluorescent biosensors," *RSC Adv.*, vol. 9, no. 16, pp. 8778–8881, 2019.

[43]Q. Wu, W. Miao, H. Gao, and D. Hui, "Mechanical properties of nanomaterials: A review," *Nanotechnol. Rev.,* vol. 9, no. 1, pp. 259–273, 2020.

[44]W. Zhu, Y. Guo, B. Ma, X. Yang , Y. Li, P. Li, Y. Zhou and M. Shuai, "Fabrication of highly dispersed Pd nanoparticles supported on reduced graphene oxide for solid phase catalytic hydrogenation of 1, 4-bis (phenylethynyl) benzene," *Int. J. Hydrogen Energy*, vol. 45, no. 15, pp. 8385–8395, 2020.

[45]X. Liu, M. Xu, L. Wan, L. Wan, H. Zhu, K.Yao, R. Linguerri, G.Chambaud, Y.Han, and C.Meng, "Superior catalytic performance of atomically dispersed palladium on graphene in CO oxidation," *ACS Catal.*, vol. 10, no. 5, pp. 3084–3093, 2020.

[46]P. Makvandi, "C. y. Wang, EN Zare, A. Borzacchiello, L. n. Niu, FR Tay," *Adv. Funct. Mater*, vol. 30, p. 1910021, 2020.

[47]E. Castro, A. H. Garcia, G. Zavala, and L. Echegoyen, "Fullerenes in biology and medicine," *J. Mater. Chem. B*, vol. 5, no. 32, pp. 6523–6535, 2017.

[48]F. Davar and M. R. Loghman-Estarki, "Synthesis and optical properties of pure monoclinic zirconia nanosheets by a new precursor," *Ceram. Int.*, vol. 40, no. 6, pp. 8427–8433, 2014.

[49]L.Renuka,K.S.Anantharajubc,S.C.Sharmade,H.Nagabhushanaf,Y.S.Vidy -ag,H.P.Nagaswarupaa and S.C.Prashantha , "A comparative study on the structural, optical, electrochemical and photocatalytic properties of ZrO2

nanooxide synthesized by different routes," *J. Alloys Compd.,* vol. 695, pp. 382–395, 2017.

[50]R. Dwivedi, A. Maurya, A. Verma, R. Prasad, and K. S. Bartwal, "Microwave assisted sol–gel synthesis of tetragonal zirconia nanoparticles," *J. Alloys Compd.,* vol. 509, no. 24, pp. 6848–6851, 2011.

[51]S. Li, M. Li, C. Zhang, S. Wang, X. Ma, and J. Gong, "Steam reforming of ethanol over Ni/ZrO$_2$ catalysts: Effect of support on product distribution," *Int. J. Hydrogen Energy*, vol. 37, no. 3, pp. 2940–2949, 2012.

[52]D. Min, N. Hoivik, G. U. Jensen, F. Tyholdt, C. Haavik, and U. Hanke, "Dielectric properties of thin-film ZrO$_2$ up to 50 GHz for RF MEMS switches," *Appl. Phys. A*, vol. 105, no. 4, pp. 867–874, 2011.

[53]H. H. Zender, H. Leistner, and H. R. Searle, "ZrO$_2$ materials for application in the ceramics industry," *Interceram*, vol. 39, no. 6, pp. 33–36, 1990.

[54]Y. Zhao, Y. Zhang, J. Li, and X. Du, "Solvothermal synthesis of visible-light-active N-modified ZrO$_2$ nanoparticles," *Mater. Lett.*, vol. 130, pp. 139–142, 2014.

[55]J. Zhang, L. Li, D. Liu, J. Zhang, Y. Hao, and W. Zhang, "Multi-layer and open three-dimensionally ordered macroporous TiO$_2$–ZrO$_2$ composite: diversified design and the comparison of multiple mode photocatalytic performance," *Mater. Des.*, vol. 86, pp. 818–828, 2015.

[56]T. Lopez, M. Alvarez, F. Tzompantzi, and M. Picquart, "Photocatalytic degradation of 2, 4-dichlorophenoxiacetic acid and 2, 4, 6-trichlorophenol with ZrO$_2$ and Mn/ZrO$_2$ sol-gel materials," *J. sol-gel Sci. Technol.*, vol. 37, no. 3, pp. 207–211, 2006.

[57] G. J. Kumar, A. Banerjee, A. S. K. Sinha, Y. Su, K. Nemkovski, and C. Rath, "Cation distribution and magnetic properties of Zn-substituted $CoCr_2O_4$ nanoparticles," *J. Appl. Phys.*, vol. 123, p. 223905, 2018.

[58] R. Z. Rasool, K. Nadeem, M. Kamran, F. Zeb, N. Ahmad, and M. Mumtaz, "Comparison of anomalous magnetic properties of non-collinear $CoCr_2O_4$ and $NiCr_2O_4$ nanoparticles," *J. Magn. Magn. Mater.*, vol. 514, p. 167225, 2020.

[59] S. T. Fardood, R. Forootan, F. Moradnia, Z. Afshari, and A. Ramazani, "Green synthesis, characterization, and photocatalytic activity of cobalt chromite spinel nanoparticles," *Mater. Res. Express*, vol. 7, no. 1, p. 15086, 2020.

[60] P. Mohanty, G. B. Geetha, E. Carleschi, C. J. Sheppard, and A. R. E. Prinsloo, "Multiferroic nanoparticles of Ni doped CoCr2O4: An XPS study," *Surf. Sci. Spectra*, vol. 27, no. 1, p. 14003, 2020.

[61] F. H. Murdaka, K. Nakamura, and A. A. Nugroho, "Estimation of muon stopping site in $CoCr_2O_4$ using density functional theory," *in IOP Conference Series: Materials Science and Engineering*, 2020, vol. 924, no. 1, p. 12027.

[62] K. Manjunatha, V. J. Angadi, R. A. P. Ribeiro, M. C. Oliveira, S. R. de Lázaro, M. R. D. Bomio, S. Matteppanavar, S. Rayaprol, P. D. Babug and U. M.Pasha, "Structural, electronic and magnetic properties of Sc 3+ doped $CoCr_2O_4$ nanoparticles," *New J. Chem.*, vol. 44, no. 33, pp. 14246–14255, 2020.

[63] K. Manjunatha, V. J. Angadi, K. M. Srinivasamurthy, S. Matteppanavar, V. K. Pattar, and U. M. Pasha, "Exploring the Structural, Dielectric and Magnetic Properties of 5 Mol% Bi^{3+}-Substituted $CoCr_2O_4$Nanoparticles," *J. Supercond. Nov. Magn.*, pp. 1–11, 2020.

[64]P. Choudhary, P. Saxena, A. Yadav, V. N. Rai, and A. Mishra, "Dielectric and ferroelectric properties of CoCr$_2$O$_4$ nanoceramics," *J. Adv. Dielectr.*, vol. 9, no. 03, p. 1950015, 2019.

[65]S. Chamyani, A. Salehirad, N. Oroujzadeh, and D. S. Fateh, "Effect of fuel type on structural and physicochemical properties of solution combustion synthesized CoCr$_2$O$_4$ ceramic pigment nanoparticles*," Ceram. Int.*, vol. 44, no. 7, pp. 7754–7760, 2018.

[66]M. A. Kassem, A. A. El-Fadl, A. M. Nashaat, and H. Nakamura, "Structure, optical and varying magnetic properties of insulating MCr$_2$O$_4$ (M= Co, Zn, Mg and Cd) nanospinels," *J. Alloys Compd.*, vol. 790, pp. 853–862, 2019.

[67]G. J. Kumar and C. Rath, "Study of exchange bias and memory effect in core-shell CoCr$_2$O$_4$ nanoparticles," *J. Magn. Magn. Mater.*, vol. 466, pp. 69–74, 2018.

[68]I. Bibi , N.Nazar,M.Iqbal,S.Kamal ,H.Nawaz ,S.Nouren,Y.Safa ,K.Jilani ,M.Sultan,S.Ata,F.Rehman and M.Abbas et al., "Green and eco-friendly synthesis of cobalt-oxide nanoparticle: characterization and photo-catalytic activity," *Adv. Powder Technol.*, vol. 28, no. 9, pp. 2035–2043, 2017.

[69]Z. Wang, J.Deng,Y.Liu,H.Yang,S.Xie,Z.Wu and H.Dai , "Three-dimensionally ordered macroporous CoCr2O4-supported Au–Pd alloy nanoparticles: highly active catalysts for methane combustion," *Catal. Today*, vol. 281, pp. 467–476, 2017.

[70] C.C. Lin and C.C. L. McCrory, "Effect of Chromium Doping on Electrochemical Water Oxidation Activity by Co$_3$–x Cr x O$_4$ Spinel Catalysts," *ACS Catal.*, vol. 7, no. 1, pp. 443–451, 2017.

[71]T.-T. Zhang, J.-D. Song, J.-X. Chen, A.-P. Jia, M.-F. Luo, and J.-Q. Lu, "Catalytic combustion of dichloromethane over supported $CoCr_2O_4$/TUD-1 catalysts: The effect of $CoCr_2O_4$ particle size on the modification of surface properties and the catalytic performance," *Appl. Surf. Sci.*, vol. 425, pp. 1074–1081, 2017.

[72]L. Liao , H.Zhang,W.Li , X.Huang,Z.Xiao,K.Xu,J.Yang,R.Zou and J.Hua , "Facile synthesis of maguey-like $CuCo_2O_4$ nanowires with high areal capacitance for supercapacitors," *J. Alloys Compd.*, vol. 695, pp. 3503–3510, 2017.

[73]M. Han , Z.Wang,Y.Xu,R.Wu,S.JiaoY.Chen and S.Feng , "Physical properties of $MgAl_2O_4$, $CoAl_2O_4$, $NiAl_2O_4$, $CuAl_2O_4$, and $ZnAl_2O_4$ spinels synthesized by a solution combustion method," *Mater. Chem. Phys.*, vol. 215, pp. 251–258, 2018.

[74]M. Kamran, K. Nadeem, and M. Mumtaz, "Negative and anomalous T-dependent magnetization trend in CoCr2O4 nanoparticles," *Solid State Sci.*, vol. 72, pp. 21–27, 2017.

[75] A.Nanda, S.Nanda, T.A. Nguyen, Y. Slimani, and S. Rajendran, (Eds.). *Nanocosmetics: Fundamentals, Applications and Toxicity*. Micro and Nano Technologies,2020.

[76] O.Fesenko, and L. Yatsenko, (Eds.). *Nanooptics and Photonics, Nanochemistry and Nanobiotechnology, and Their Applications: Selected Proceedings of the 7th International Conference Nanotechnology and Nanomaterials (NANO2019), 27–30 August 2019, Lviv, Ukraine* (Vol. 247). Springer Nature,2020.

[77] V.Met, Characterization of the spatial distribution of irradiance and spectrum in concentrating photovoltaic systems and their effect on multi-junction solar cells. Prog Photovolt es Appl 21(3):308–318, 2013.

[78] L. HW ,Multi-junction solar cell devices. Google Patents, 2011.

[79]K. Ali, A. Khalid, M. R. Ahmad, H. M. Khan, I. Ali, and S. K. Sharma, "Multi-junction (III–V) solar cells: From basics to advanced materials choices," *in Solar Cells, Springer*, pp. 325–350, 2020.

[80]A. Xia, C. Jin, D. Du, and G. Zhu, "Comparative study of structural and magnetic properties of NiZnCu ferrite powders prepared via chemical coprecipitation method with different coprecipitators," *J. Magn. Magn. Mater.*, vol. 323, no. 12, pp. 1682–1685, 2011.

[81]Y. Slimani , B.Unal,M.A.Almessiere,A. Demir Korkmaz,S. E.Shirsath,Ghulam Yasin,A.V.Trukhanov,A.Baykal, "Investigation of structural and physical properties of Eu3+ ions substituted Ni0. 4Cu0. 2Zn0. 4Fe2O4 spinel ferrite nanoparticles prepared via sonochemical approach," *Results Phys.,* vol. 17, p. 103061, 2020.

[82]Y.Slimani,M.A.Almessiere,A.DemirKorkmaz,S.Guner,H.Güngüneş,M.S ertkol,A.Manikandan,A.Yildiz,S.Akhtar,S.E.Shirsath, A.Baykal, "Ni0. 4Cu0. 2Zn0. 4TbxFe$_2$-xO$_4$ nanospinel ferrites: ultrasonic synthesis and physical properties," *Ultrason. Sonochem.*, vol. 59, p. 104757, 2019.

[83]M. A. Almessiere, Y.Slimani,A.D.Korkmaz,S.Guner,M.Sertkol,S. E.Shirsath and A.Baykal , "Structural, optical and magnetic properties of Tm^{3+} substituted cobalt spinel ferrites synthesized via sonochemical approach," *Ultrason. Sonochem.*, vol. 54, pp. 1–10, 2019.

[84]M. Vinatoru and T. J. Mason, "Can sonochemistry take place in the absence of cavitation?–a complementary view of how ultrasound can interact with materials," *Ultrason. Sonochem.,* vol. 52, pp. 2–5, 2019.

[85]V. Grosjean, C. Julcour, O. Louisnard, and L. Barthe, "Axial acoustic field along a solid-liquid fluidized bed under power ultrasound," *Ultrason. Sonochem.*, vol. 56, pp. 274–283, 2019.

[86]B. Zhu , C.Fei, C.Wan, Y.Zhu, X.Yang, H.Zhen, Q.Zhou and K. K. Shung, "Self-focused AlScN film ultrasound transducer for individual cell manipulation," *ACS sensors*, vol. 2, no. 1, pp. 172–177, 2017.

[87]S. Sabrina , M.Tasinkevych, S.Ahmed, A.M. Brooks, Monica

O.de L.Cruz, T. E. Mallouk and K. J. M. Bishop , "Shape-directed microspinners powered by ultrasound," *ACS Nano*, vol. 12, no. 3, pp. 2939–2947, 2018.

[88]S. Vinoth, M. Govindasamy, S.-F. Wang, and S. Anandaraj, "Layered nanocomposite of zinc sulfide covered reduced graphene oxide and their implications for electrocatalytic applications," *Ultrason. Sonochem.*, vol. 64, p. 105036, 2020.

[89]M. Govindasamy, S.-F. Wang, S. Kumaravel, R. J. Ramalingam, and H. A. Al-Lohedan, "Facile synthesis of copper sulfide decorated reduced graphene oxide nanocomposite for high sensitive detection of toxic antibiotic in milk," *Ultrason. Sonochem.*, vol. 52, pp. 382–390, 2019.

[90]Y. Asakura, "Experimental methods in sonochemistry," in Sonochemistry and the Acoustic Bubble, *Elsevier*, 2015, pp. 119–150.

[91]J. K. Rajput, P. Arora, G. Kaur, and M. Kaur, "$CuFe_2O_4$ magnetic heterogeneous nanocatalyst: Low power sonochemical-coprecipitation preparation and applications in synthesis of 4H-chromene-3-carbonitrile scaffolds," *Ultrason. Sonochem.,* vol. 26, pp. 229–240, 2015.

[92]P. A. Bozkurt, "Sonochemical green synthesis of Ag/graphene nanocomposite," Ultrason. Sonochem., vol. 35, pp. 397–404, 2017.

[93] S. S. Sabnis, R. Raikar, and P. R. Gogate, "Evaluation of different cavitational reactors for size reduction of DADPS," *Ultrason. Sonochem.*, vol. 69, p. 105276, 2020.

[94] P. Van Neer, A. Rasidovic, and A. W. F. Volker, "A study of nanoparticle manipulation using ultrasonic standing waves," in 2013 IEEE International Ultrasonics Symposium (IUS), 2013, pp. 1915–1918.

[95] S. Pilli, P. Bhunia, S. Yan, R. J. LeBlanc, R. D. Tyagi, and R. Y. Surampalli, "Ultrasonic pretreatment of sludge: a review," *Ultrason. Sonochem.*, vol. 18, no. 1, pp. 1–18, 2011.

[96] G. Ruecroft, D. Hipkiss, T. Ly, N. Maxted, and P. W. Cains, "Sonocrystallization: the use of ultrasound for improved industrial crystallization," *Org. Process Res. Dev.*, vol. 9, no. 6, pp. 923–932, 2005.

[97] O. Acisli, A. Khataee, R. D. C. Soltani, and S. Karaca, "Ultrasound-assisted Fenton process using siderite nanoparticles prepared via planetary ball milling for removal of reactive yellow 81 in aqueous phase," *Ultrason. Sonochem.*, vol. 35, pp. 210–218, 2017.

[98] P. Gholami, L. Dinpazhoh, A. Khataee, and Y. Orooji, "Sonocatalytic activity of biochar-supported ZnO nanorods in degradation of gemifloxacin: synergy study, effect of parameters and phytotoxicity evaluation," *Ultrason. Sonochem.*, vol. 55, pp. 44–56, 2019.

[99] R. A. Torres-Palma and E. A. Serna-Galvis, "Sonolysis," in Advanced oxidation processes for waste water treatment, *Elsevier*, 2018, pp. 177–213.

[100] M. Bagheri and S. A. Mirbagheri, "Critical review of fouling mitigation strategies in membrane bioreactors treating water and wastewater," *Bioresour. Technol.*, vol. 258, pp. 318–334, 2018.

[101]L. H. Thompson and L. K. Doraiswamy, "Sonochemistry: science and engineering," *Ind. Eng. Chem. Res.*, vol. 38, no. 4, pp. 1215–1249, 1999.

[102]T. H. Fatoki, "In-Silico Investigation of Luminol, Its Analogues and Improved Mechanism of Chemiluminescence for Blood Identification Beyond Forensics," *bioRxiv*, 2020.

[103]B. M. Cassidy , Z.Lu, J. P.Martin,S. K.Tazik,K. W.Kellogg,S. A.DeJong,E. O.Belliveau,K. E.Kilgore,S. M.Ervin,M,M.Rayle,A. M.Abraham,M. L.Myrick,S.L.Morgan, "A quantitative method for determining a representative detection limit of the forensic luminol test for latent bloodstains," *Forensic Sci. Int.*, vol. 278, pp. 396–403, 2017.

[104]A. Giussani, P. Farahani, D. Martínez-Muñoz, M. Lundberg, R. Lindh, and D. Roca-Sanjuan, "Molecular basis of the chemiluminescence mechanism of luminol," *Chem. Eur. J.*, vol. 25, no. 20, pp. 5202–5213, 2019.

[105]B. Jones, J. Britton, D. Mafukidze, and T. Nyokong, "Photodegradation of 4-chlorophenol using Zn and In phthalocyanines substituted with pyrrole without hetero atoms linkers and supported on polyacrylonitrile electrospun fibres," *Polyhedron*, vol. 178, p. 114329, 2020.

[106]V. Selvaraj, T. S. Karthika, C. Mansiya, and M. Alagar, "An over review on recently developed techniques, mechanisms and intermediate involved in the advanced azo dye degradation for industrial applications," *J. Mol. Struct.*, p. 129195, 2020.

[107]G. Chen, F. Liu, Y. Qiao, and B. Tao, "Photodegradation of tefuryltrione in water under UV irradiation: Identification of transformation products and elucidation of photodegradation pathway," *Chemosphere,* vol. 227, pp. 133–141, 2019.

[108]S. M. T. H. Moghaddas, B. Elahi, and V. Javanbakht, "Biosynthesis of pure zinc oxide nanoparticles using Quince seed mucilage for photocatalytic dye degradation," *J. Alloys Compd.,* vol. 821, p. 153519, 2020.

[109]M. H. H. Ali, K. M. Al-Qahtani, and S. M. El-Sayed, "Enhancing photodegradation of 2, 4, 6 trichlorophenol and organic pollutants in industrial effluents using nanocomposite of TiO2 doped with reduced graphene oxide," *Egypt. J. Aquat. Res.*, vol. 45, no. 4, pp. 321–328, 2019.

[110]H. Lin, K. Pang, Y. Ma, and J. Hu, "Photodegradation of fluazaindolizine in water under simulated sunlight irradiation: Identification of transformation products and elucidation of transformation mechanism," *Chemosphere*, vol. 214, pp. 543–552, 2019.

[111]K. I. Predick, S. R. Archer, S. M. Aguillon, D. A. Keller, H. L. Throop, and P. W. Barnes, "UV-B radiation and shrub canopy effects on surface litter decomposition in a shrub-invaded dry grassland," *J. Arid Environ.,* vol. 157, pp. 13–21, 2018.

[112]T. Sano, N. Negishi, K. Uchino, J. Tanaka, S. Matsuzawa, and K. Takeuchi, "Photocatalytic degradation of gaseous acetaldehyde on TiO2 with photodeposited metals and metal oxides," *J. Photochem. Photobiol. A Chem.,* vol. 160, no. 1–2, pp. 93–98, 2003.

[113]H. Zabihi-Mobarakeh and A. Nezamzadeh-Ejhieh, "Application of supported TiO2 onto Iranian clinoptilolite nanoparticles in the photodegradation of mixture of aniline and 2, 4-dinitroaniline aqueous solution," *J. Ind. Eng. Chem.,* vol. 26, pp. 315–321, 2015.

[114]F.p. Zee, "Anaerobic azo dye reduction," *Netherlands Wegeningen Univ.*, 2002.

[115]K. Kalpana and V. Selvaraj, "A novel approach for the synthesis of highly active $ZnO/TiO_2/Ag_2O$ nanocomposite and its photocatalytic applications," *Ceram. Int.*, vol. 41, no. 8, pp. 9671–9679, 2015.

[116]L. G. Wang, C. M. Zhu, L. Chen, and S. L. Yuan, "Exchange bias effect in $CoCr_2O_4/NiO$ system prepared by two-step method," *Solid State Commun.*, vol. 251, pp. 39–42, 2017.

[117]Y. Hao, L. Li, J. Zhang, H. Luo, X. Zhang, and E. Chen, "Multilayer and open structure of dendritic crosslinked CeO2-ZrO2 composite: Enhanced photocatalytic degradation and water splitting performance," *Int. J. Hydrogen Energy*, vol. 42, no. 9, pp. 5916–5929, 2017.

[118]E. Berei , O. Ştefănescu, C. Muntean, T. Vlase, B. O. Ţăranu, A. Dabici and M. Ştefănescu , "A novel route for the preparation of $CoCr_2O_4/SiO_2$ nanocomposite starting from Co (II)–Cr (III) carboxylate complex combinations," *J. Mater. Sci.*, vol. 53, no. 6, pp. 4159–4172, 2018.

[119]E. Hong, C. Kim, D.-H. Lim, H.-J. Cho, and C.-H. Shin, "Catalytic methane combustion over Pd/ZrO_2 catalysts: Effects of crystalline structure and textural properties," *Appl. Catal. B Environ.*, vol. 232, pp. 544–552, 2018.

[120]J.-Y. Huang and W.-R. Liu, "Synthesis and characterizations of $CoCr_2O_4/C$ composite using high energy ball-milling technique as novel anode materials for Li-ion batteries," *J. Taiwan Inst. Chem. Eng.*, vol. 96, pp. 205–213, 2019.

[121]X. Zhang , M.Zhang,J.Zhang,Q.Zhang,N.Tsubaki,Y.Tan and Y.Han, "Methane decomposition and carbon deposition over Ni/ZrO2 catalysts: comparison of amorphous, tetragonal, and monoclinic zirconia phase," *Int. J. Hydrogen Energy*, vol. 44, no. 33, pp. 17887–17899, 2019.

[122]K. Nadeem, H,Ur Rehman,F.Zeb,E.Ali,M.Kamran,N.A.Noshahi and H.Abbasa , "Magnetic phase diagram and dielectric properties of Mn doped CoCr2O4 nanoparticles," *J. Alloys Compd.*, vol. 832, p. 155031, 2020.

[123]M. Zhang , J.Zhang, Z. Zhou, S.Chen, T.Zhang, F.Song,Q.Zhang, N.Tsubaki,Y.Tan and Y.Han, "Effects of the surface adsorbed oxygen species tuned by rare-earth metal doping on dry reforming of methane over Ni/ZrO$_2$ catalyst," *Appl. Catal. B Environ.*, vol. 264, p. 118522, 2020.

[124] K. L. Lin, T. Yang, F. F. Zhang, G. Lei, H. Y. Zou, Y. F. Li and C. Z. Huang . Luminol and gold nanoparticle-co-precipitated reduced graphene oxide hybrids with long-persistent chemiluminescence for cholesterol detection. *Journal of Materials Chemistry B*, *5*(35), 7335-7341. 2017.

[125] L. Zhang, Z. Tang, and Y. Dong. Silicon quantum dot involved luminol chemiluminescence and its sensitive detection of dopamine. *Analytical methods*, *10*(34), 4129-4135. 2018.

[126] L. Yue, and Y. T. Liu. Mechanistic Insight into pH-Dependent Luminol Chemiluminescence in Aqueous Solution. *The Journal of Physical Chemistry B, 124*(35), 7682-7693,2020 .

[127]A. A. Ali, T. A. Fahad, and A. A. Al-muhsin, "Preparation and Spectroanalytical Studies of Two New Azo Dyes Based on Luminol," *in IOP Conference Series: Materials Science and Engineering*, 2020, vol. 928, no. 5, p. 52007.

[128]R. Aswathy and K. Mohanan, "Microwave Assisted Synthesis, Characterisation and Fluorescence Studies of some Transition Metal Complexes with a Luminol Derivative.," *J. Fluoresc.*, vol. 27, no. 3, pp. 1171–1181, 2017.

[129]D. A. Skoog, D. M. West, F. J. Holler, and S. R. Crouch, Fundamentals of analytical chemistry. *Cengage learning*, 2013.

[130]K. Robards and S. Dilli, "Analytical chemistry of synthetic food antioxidants. *A review," Analyst*, vol. 112, no. 7, pp. 933–943, 1987.

[131]Z. J. Shanan, H. F. Al-Taay, N. Khaleel, R. Nader, E. Kaddum, and S. Talal, "Structural and optical properties of chemically sprayed ZnS nanostructure," *IOSR-JAP*, vol. 8, no. 5, pp. 66–72, 2016.

[132]A. Raidou et al., "Characterization of ZnO thin films grown by SILAR method," *Open Access Libr. J.*, vol. 1, no. 3, pp. 1–9, 2014.

[133] D. Moore and R. Reynolds," X-Ray Diffraction and the Identification and Analysis of Clay minerals", 2nd edition, Oxford University Press, *Oxford, UK, CH 3*, 1997.

[134]H. L. Lee, A. M. Issam, M. Belmahi, M. B. Assouar, H. Rinnert, and M. Alnot, "Synthesis and characterizations of bare CdS nanocrystals using chemical precipitation method for photoluminescence application," *J. Nanomater.*, vol. 2009, 2009.

[135]B. Barrocas, O. C. Monteiro, M. E. M. Jorge, and S. Sério, "Photocatalytic activity and reusability study of nanocrystalline TiO_2 films prepared by sputtering technique," *Appl. Surf. Sci.*, vol. 264, pp. 111–116, 2013.

[136]S. Ahmed, "Photo electrochemical study of ferrioxalate actinometry at a glassy carbon electrode," *J. Photochem. Photobiol. A Chem.*, vol. 161, no. 2–3, pp. 151–154, 2004.

[137]A. W. Adamson, A. Vogler, H. Kunkely, and R. Wachter, "Photocalorimetry. Enthalpies of photolysis of trans-azobenzene, ferrioxalate

and cobaltioxalate ions, chromium hexacarbonyl, and dirhenium decarbonyl," *J. Am. Chem.* Soc., vol. 100, no. 4, pp. 1298–1300, 1978.

[138]S. I. Zuafuani and L. M. Ahmed, "Photocatalytic decolourization of direct orange Dye by zinc oxide under UV irradiation," *Int. J. Chem. Sci*, vol. 13, no. 1, pp. 187–196, 2015.

[139]M. A. Tabbara and M. M. El Jamaf, "BYNa, SO, COMPARISON WITH NaOH," *J. Univ. Chem. Technol. Metall.*, vol. 47, no. 3, pp. 275–282, 2012.

[140] P. Atkins and J. Paula, "Atkins' Physical Chemistry", 8th edition, W. H. Freeman and Company, *New York*, CH3, p. 96, 2006.

[141] S. Han, "Microstructural Properties of Nanostructures",1st edition, *Springer, Berlin*, *CH7*, pp. 198-199, 2012

[142] T. P. Hadjiioannoy, G. D. Christian, C. E. Efstathion and D. P. Nikolelis, "Problem and Solvent in Analytical Chemistry", Pergamon Press, *New York*, pp. 341- 342, 1988.

[143] J. D. Ingle, R. C. Stanley, "Spectrochemical Analysis", 1st edition, Prentice Halli, *New York*, pp. 386 –387, 1988.

[144]P. E. Aranha, M. P. dos Santos, S. Romera, and E. R. Dockal, "Synthesis, characterization, and spectroscopic studies of tetradentate Schiff base chromium (III) complexes," *Polyhedron*, vol. 26, no. 7, pp. 1373–1382, 2007.

[145]F. Adam, K. M. Hello, and H. Osman, "Synthesis of mesoporous silica immobilized with 3-[(Mercapto or amino)propyl]trialkoxysilane by a simple one-pot reaction," *Chinese J. Chem.*, vol. 28, no. 12, pp. 2383–2388, 2010.

[146]T. J. Al-Hasani, H. H. Mihsen, K. M. Hello, and F. Adam, "Catalytic esterification via silica immobilized p-phenylenediamine and dithiooxamide solid catalysts," *Arab. J. Chem.*, vol. 10, pp. S1492–S1500, 2017.

[147]E. A. Saratovskikh, B. L. Psikha, and N. A. Sanina, "The reaction of the iron thiosulfate-nitrosyl complex with adenosine triphosphoric acid," *Scientific Research*,2013.

[148]F. B. Miguel, J. A. Dantas, S. Amorim, G. F. S. Andrade, L. A. S. Costa, and M. R. C. Couri, "Synthesis, spectroscopic and computational characterization of the tautomerism of pyrazoline derivatives from chalcones," *Spectrochim. Acta Part A Mol. Biomol. Spectrosc.*, vol. 152, pp. 318–326, 2016.

[149]K. J. AL-Adilee, A. K. Abass, and A. M. Taher, "Synthesis of some transition metal complexes with new heterocyclic thiazolyl azo dye and their uses as sensitizers in photo reactions," *J. Mol. Struct.*, vol. 1108, pp. 378–397, 2016.

[150]K. Al-Adilee and H. A. K. Kyhoiesh, "Preparation and identification of some metal complexes with new heterocyclic azo dye ligand 2-[2−-(1-Hydroxy-4-Chloro phenyl) azo]-imidazole and their spectral and thermal studies," *J. Mol. Struct.*, vol. 1137, pp. 160–178, 2017.

[151]Sulekh, M. Tyagi, and Kjj. Sharma, "Mn (II), Co (II), Ni (II) and Cu (II) complexes of a tertraaza macrocyclic ligand: Synthesis, characterization and biological screening," *J. Iran. Chem. Soc.*, vol. 6, no. 2, pp. 310–316, 2009.

[152]C. E. Housecroft and A. G. Sharpe, "Inorganic chemistry third edition," *Harlow Pearson Educ. Ltd.*, 2008.

[153] Z.Tian, C. Zhu, J. Wang, Z. Xia, Y. Liu, and S.Yuan, Size dependence of structure and magnetic properties of $CoCr_2O_4$ nanoparticles synthesized by hydrothermal technique, *J. Magn. Magn. Mater.*, 377, 176–182, 2015.

[154]P. Choudhary, A. Yadav, and D.Varshney, Structural and optical studies of nanocrystalline $ZnCr_2O_4$ and $CoCr_2O_4$ spinel, *AIP Conference Proceedings,* 1832 (1), 50051,2017.

[155] B.Granados, N. and Restrepo-Baena, O. J., Flame spray pyrolysis synthesis of ceramic nanopigments CoCr2O4: The effect of key variables, *J. Eur. Ceram. Soc.,* 37(15), 5051–5056,2017.

[156] M.K.Hayawi, M.M.Kareem, , and L.M.Ahmed, , Synthesis of Spinel Mn3O4 and Spinel Mn3O4/ZrO2 Nanocomposites and Using Them in Photo-Catalytic Decolorization of Fe (II)-(4, 5-Diazafluoren-9-One 11) Complex, *Periódico Tchê Química*, 17(34), 689–699,2020.

[157] M.A.Kassem, A.A. El-Fadl, A.M.Nashaat, and H.Nakamura, Structure, optical and varying magnetic properties of insulating MCr_2O_4 (M= Co, Zn, Mg and Cd) nanospinels, *J. Alloys Compd.,* 790, 853–862,2019.

[158] D.C.Ghosh, and R. Biswas, Theoretical Calculation of Absolute Radii of Atoms and Ions. Part 2. The Ionic Radii, *Int. J. Mol. Sci.*, 4(6), 379-407,2003.

[159] E.S.Fadhil, L.M.Ahmed, and A.F.Mohammed, Effect of Silver Doping On Structural and Photocatalytic Circumstances of ZnO Nanoparticles, *Iraqi Journal of Nanotechnology*, synthesis and application 1, 13-20,2020.

[160] L.M.Ahmed, F.H.Hussein, and A. Mahdi, Photocatalytic Dehydrogenation of Aqueous Methanol Solution by Naked and Platinized TiO2 Nanoparticles, *Asian Journal of Chemistry*. 24(12). 5564-5568,2012.

[161] L.M.Ahmed, I.Ivanova, F.H.Hussein, and D.W.Bahnemann, Role of Platinum Deposited on TiO2 in Photocatalytic Methanol Oxidation and Dehydrogenation Reactions, *International Journal of Photoenergy*, 1-9, 2014.

[162]M. Al-Shakban, A.M. Abbas and L.M. Ahmed, Chemical Vapour Deposition of CdS Thin Films at Low Temperatures from Cadmium Ethyl Xanthate, *Egyptian Journal of Chemistry*, 64(5), 2533 - 2538, 2021.

[163] B.M.Mohammed, and L.M.Ahmed, Improvement the Photo Catalytic Properties of ZnS nanoparticle with Loaded Manganese and Chromium by Co-Precipitation Method, *Journal of Global Pharma Technology*, 10(7), 129- 138, 2018.

[164] S.M. Ali, M.A.Alali, and L.M.Ahmed, Flower-like Hierarchical Nanostructures Synthesis of Polyoxometalate- Dopamine and loading Furosemide on its surface and aging them using microwave technique,*Acceptance in AIP Conference Proceedings* ,2021.

[165] Y.Dai, H.Wang, S. Liu, K.J. Smith, M.O. Wolf, and M.J.MacLachlan, $CoCr_2O_4$ nanospheres for low temperature methane oxidation*, Cryst. Eng. Comm,* 22(26), 4404–4415,2020.

[166]F. H. Fakhri and L. M. Ahmed, "Incorporation Cds with Zns as Composite and Using in Photo-Decolorization of Congo Red Dye," *Indones. J. Chem.*, vol. 19, no. 4, pp. 936–943, 2019.

[167] S. T. Fardood, R. Forootan, F. Moradnia, Z. Afshari, and A. Ramazani, "Green synthesis, characterization, and photocatalytic activity of cobalt chromite spinel nanoparticles," *Mater. Res. Express*, vol. 7, no. 1, p. 15086, 2020.

[168]B. M. Pirzada, N. A. Mir, N. Qutub, O. Mehraj, S. Sabir, and M. Muneer, "Synthesis, characterization and optimization of photocatalytic activity of TiO$_2$/ZrO$_2$ nanocomposite heterostructures," *Mater. Sci. Eng. B,* vol. 193, pp. 137–145, 2015.

[169]L. M. Ahmed, S. I. Saaed, and A. A. Marhoon, "Effect of Oxidation Agents on Photo-Decolorization of Vitamin B 12 in the Presence of ZnO/UV-A System," *Indones. J. Chem.*, vol. 18, no. 2, pp. 272–278, 2018.

[170]S. H. Bossmann, E.Oliveros, S.Göb, S.Siegwart, E. P. Dahlen, L.Payawan, M.Straub, M.Wörner, and A. M. Braun , "New evidence against hydroxyl radicals as reactive intermediates in the thermal and photochemically enhanced Fenton reactions," *J. Phys. Chem. A*, vol. 102, no. 28, pp. 5542–5550, 1998.

[171]K. M. Jasim and L. M. Ahmed, "TiO$_2$ nanoparticles sensitized by safranine O dye using UV-A light system," *in IOP Conference series: Materials science and Engineering*, 2019, vol. 571, no. 1, p. 12064.

[172] K. O. Kzar, Z. F.Mohammed, S. I. Saeed1, L. M. Ahmed, D.I. Kareem, H. Hadyi, and A. J. Kadhim, "Heterogeneous photo-decolourization of cobaltous phthalocyaninate dye (Reactive green dye) catalyzed by ZnO," *in AIP Conference Proceedings*, 2019, vol. 2144, no. 1, p. 20004.

الخلاصة

يتضمن هذا العمل العملي ثلاثة أجزاء رئيسية **الجزء الأول** يوضح تحضير كاشف Luminol و الليكاند (Luminol- tyrosine) والمعقد (Luminol-Tyrosine)-(II)Fe وتم تأكيد التحضير من خلال طيف Uv-Visible و طيف FTIR و اطياف HNMR و التحليل الدقيق للعناصر (C.H.N) و نقطة الانصهار وجدة تهجين المعقد FeL_2CL_2 بهيئة شكل ثماني السطوح وقد تم اثبات ذلك باستخدام طريقة النسب المولية وقياس الحساسية المغناطيسية حيث اتضحت هي ٢:١.

ركز **الجزء الثاني** على تحضير الإسبنيل $CoCr_2O_4$ باستخدام طريقة الترسيب المشترك. تم تعديل سطح الإسبنيل $CoCr_2O_4$ باختيار ZrO_2 لتحسين خواصه. وتم تحضير متراكبات من الإسبنيل المدمج $CoCr_2O_4$ مع ZrO_2 بنسب مختلفة (٢ :١ و ٣ :١) باستخدام تقنية الموجات فوق الصوتية كطريقة بسيطة وصديقة للبيئة   بناءً على تحليل XRD ، فإن متراكبات الإسبنيل $CoCr_2O_4$ و ZrO_2 التجارية والإسبنيل $CoCr_2O_4$ / ZrO_2 بنسب مختلفة (٢ :١ و ٣ :١) هي أحجام نانو تتراوح من ٨,١٧٨٥ نانومتر إلى ١٥,٥٨٢٣ نانومتر.

ZrO_2 > متراكب ٣ :١ > متراكب ٢ :١ > إسبنيل $CoCr_2O_4$
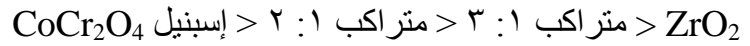
أعطت أطياف SEM فكرة عن شكل سطح المحفزات الضوئية المدروسة. شكل الإسبنيل $CoCr_2O_4$ والباقي المحفزات الضوئية شبه كروية باستثناء ZrO_2 كروية الشكل . تم العثور على أحجام الجسيمات التي تم قياسها والتي تم تحديدها من أطياف SEM من ١٧,٨٩ نانومتر إلى ٥٢,٦٢ نانومتر وجميع العينات المدروسة تعتبر بلورات نانوية. من خلال طيف EDX ، جميع العناصر التي تتكون منها المحفزات الضوئية موجودة ولا يوجد شوائب معها. تكتشف الأطياف عن وجود Co و Cr و Zr و O في كروميت الكوبالت المركب ومواده النانوية المركبة. تم استخدام معادلة Tauc لإيجاد كل أنواع فجوات النطاق للمحفزات الضوئية المدروسة. فجوات النطاق غير مباشرة لجميع العينات وتزداد قيمتها بزيادة نسبة ZrO_2.   تسلسل قيم فجوات النطاق هو 2 :Bg Comp.1> Bg spinel CoCr2O4 <3 :Bg Comp.1> Bg ZrO_2 ، ويساوي ٣,٢ . eV 5> 4.8eV> 4.7 eV> eV.

في الجزء الثالث ، تم تطبيق المحفزات الضوئية المدروسة. تم تقدير إزالة اللون الضوئي للمعقد FeL_2CL_2 عند درجة الحموضة ٧,٣ باستخدام السبنل $CoCr_2O_4$ و ZrO_2 التجاري والمتراكبات ٢ :١ و ٣ :١. التمراكب ٣ :١ هو أفضل مركب مقارنة بالمركب ٢ :١ ،. تم إ الطبيق للمحفزات الضوئية المدروسة في هذا التفاعل الضوئي هي ٠,١ غم / ١٠٠ مل و ٠,٢ غم / ١٠٠ مل و ٠,٣ غم / ١٠٠ مل الى السبنل $CoCr_2O_4$ و ZrO_2 والمتراكب ٢ :١ والمتراكب ٣ :١ على التوالي. عززت درجة الحرارة المتناقصة إزالة اللون للمعقد المستخدم باستخدام السبنل $CoCr_2O_4$ والمتراكب ٣ :١ ، ولكنها تثبطت باستخدام ZrO_2 . ووجد ان طاقة التنشيط لاستخدام المتراكب ٣ :١ أقل من استخدام السبنل $CoCr_2O_4$ والتي تساوي ٩٣,١٠٨٤- كيلو جول مول ١- و ٤٦,٢٤٩٩- كيلو جول مول ١-، على التوالي. يعتمد هذا السلوك على هيكل الإسبينيل الذي يتضمن من معدنين مختلفين في حالة أكسدة والتهجين (مثل Co (II) كرباعي السطوح و Cr (III) كثماني السطوح).

تحضير وتشخيص خصائص الجسيمات النانوية للمتراكب الشوكي كوبلت كرومايت \ اوكسيد الزركونيوم وتطبيقة على محلول ملون

رسالة مقدمة الى

مجلس كلية العلوم ــ جامعة كربلاء

كجزء من استكمال متطلبات نيل درجة الماجستير

علوم في الكيمياء

تقدم بها

حمد حميد كاظم سردي الطائي

بكالوريوس علوم في الكيمياء (٢٠٠٨) الجامعة بابل

اشراف

أ. د لمى مجيد احمد   أ. د مهند موسى كريم

٢٠٢١ م   ١٤٤٣ هـ